8-2018

Physiological and Environmental Impacts of Nanomaterials-Biomolecular Coronae

Achyut J. Raghavendra
Clemson University, araghav@g.clemson.edu

Follow this and additional works at: https://tigerprints.clemson.edu/all_dissertations

PHYSIOLOGICAL AND ENVIRONMENTAL IMPACTS OF NANOMATERIALS—
BIOMOECULAR CORONAE

A Dissertation
Presented to
the Graduate School of
Clemson University

In Partial Fulfillment
of the Requirements for the Degree
Doctor of Philosophy
Physics

---

by
Achyut J. Raghavendra
August 2018

Accepted by:
Dr. Ramakrishna Podila, Committee Chair
Dr. Apparao M. Rao
Dr. Feng Ding
Dr. Jeremy Tzeng

ABSTRACT

Engineered nanomaterials (ENMs) exhibit unique electronic and optical properties, which are suitable for the broad spectrum of applications including biomedical, aerospace, textiles, agriculture. Such unique properties of ENMs also raise significant concerns over their adverse ecological and physiological effects. In the past two decades, ENMs were found to exhibit complex interactions in biological milieu. It is expected that physicochemical properties of ENMs and their surrounding environment influence their environmental and physiological fate and transport. Indeed, a comprehensive understanding of interactions at the nano-bio interface is critical to designing environmentally and physiologically benign ENMs pivotal to the future growth of nanomedicine and its applications. To this end, the present work experimentally investigates nanomaterial-biomolecular corona (or biocorona) using spectroscopic techniques and biological assays. Specifically, the influence of defects, surface functionalization, and physiological environment on the formation of biocorona and ensuing biological responses is presented.

The first two chapters (Chapters 1 and 2) provide a succinct introduction to *nanotoxicity* with focus on biocorona formation and various *spectroscopic* characterization techniques utilized. In Chapter 3, the variation in biocorona formation due to *defects* in the structure of single-walled and multi-walled carbon nanotubes (SWCNTs and MWCNTs) is presented. Briefly, it was found that defects result in significant changes in the nature and amount of proteins adsorbed on SWCNTs due to

differences in their charge distribution. In case of MWCNTs, carboxylated MWCNTs with higher density of defects resulted in a stronger binding and efficient delivery of antigens. In Chapter 4, a unique study exploring the effect of diseased (*hyperlipidemic*) physiological state on the biocorona composition (instead of the normal healthy state) is presented. Our findings suggest that disease-induced variations in the physiological environment have a significant impact on nanomaterial-biomolecular corona, cell response, and cellular association.

In Chapter 5 provides new spectroscopic insights into *charge transfer* interactions between biomolecules (aromatic amino acid complexes) and emerging two-dimensional (2D) ENMs like graphene, graphene oxide, and BN. The adsorption of amino acids on 2D materials was observed to considerably alter their biological response in terms of generation of reactive oxygen species. Also, the influence of different surface functional groups on Ag nanoparticles on conformational changes in apolipoprotein biocorona and ensuing biological is explored. Finally, Chapter 6 explores *environmental effects* of graphene, BN upon their interaction with natural organic matter (NOM). The results show that the delocalized π-electron cloud in graphene facilitated a significant charge transfer and chemisorption of NOM unlike BN. Also, BN was found to result in algal cell rupture and reduction in photosynthetic activity unlike graphene.

DEDICATION

To my beloved family, for their continual support to my endeavors.

ACKNOWLEDGMENTS

TABLE OF CONTENTS

Table of Contents (Continued)

LIST OF TABLES

LIST OF FIGURES

List of Figures (Continued)

CHAPTER ONE

NANOTOXICITY REVIEW

In the past decade, nanomaterial-based products found their way to consumer stores translating nanotechnology from bench to bedside. Nanotechnology impacted several industries including energy, medical, sports, electronics, agriculture, and textiles. Vance *et al.*[3] reported a thirty-fold increase in a number of nano engineered products between 2005 and 2015. Among fast-growing metal nanoparticles applications, silver takes a major share of 24% in the market. Therefore, human and environmental exposure to nanomaterials is inevitable. Despite the broad range of nanomaterial applications, its use is limited owing to its potential risks to the environment and human population.

Nanotoxicity is a field of research dedicated to understanding potential risks associated with the use of engineered nanomaterials (ENMs) to both humans and environment. Although concerted research efforts led to an initial assessment of nanomaterial toxicity in the last decade, there has been a lack of fundamental understanding of nano-bio interactions in terms biomoelcular adsorption or biocorona. To impress the relevance of this research interest, a database query on PubMed with 'nanoparticle AND corona' in search criteria yielded ~1000 entries as shown in **Fig. 1.1.1**. The trend shows a three-fold increase in a number of reports since 2012, which strongly suggests that the nanoparticle corona began to gain attention in the last five years.
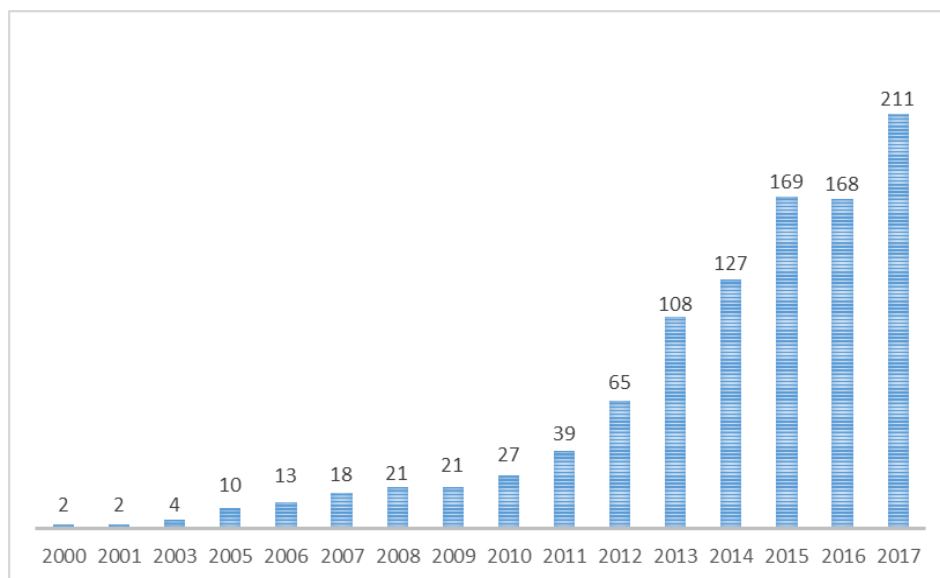
Figure 1.1.1: PubMed entries to search criteria 'nanoparticle AND corona' since 2000.

This chapter briefly describes the transport and fate of ENMs in our ecosystem and reviews findings in the literature exploring nanomaterials toxicity and its influential factors. The inadvertent fouling of ENMs by biomolecules provides a biological identity, which could potentially trigger undesired physiological responses. The following sections discuss various physicochemical properties of ENMs, which dictate the formation and composition of nanomaterial-biomolecular corona or boicorona and in turn their toxicological effects on physiology and environment.

1.1 Nanomaterial-biomolecular corona (or biocorona)

Global research efforts have led to a better understanding of nanomaterial toxicity. Yet, the fundamental mechanisms through which nano–bio interactions occur

2

still remain largely inconclusive.[4] Building on the understanding of adsorbed biomolecules in cellular responses to biomaterials, a new picture of nanotoxicity based on protein-nanomaterial interactions is recently beginning to emerge.[5]–[7] Upon their introduction to any physiological environment, the surface of nanomaterials gets coated with various biomolecules including proteins, peptides, and lipids collectively referred to as the nanomaterial-biomolecular corona or biocorona. Interestingly, it is the biocorona that dictates the fate of nanomaterials in any biological medium rather than the bare nanomaterial itself.

Biocorona is formed due to the high surface free energy of ENMs, leading to adsorption of many biomolecules, most prominently proteins in order to reduce surface free energy. Although at the initial stage most abundant proteins present in the physiological medium adsorb onto the ENM surface, these proteins will be swapped by proteins with higher affinity over time (Vroman's effect [8]). The adsorption process is governed by protein-protein interactions as well as protein affinities for the ENMsurface. As shown in the schematic **Fig 1.1.2** proteins with higher binding affinities form "hard" biocorona and low binding affinity proteins form the "soft" biocorona. Hard biocorona proteins is known to interact with ENM surface through van der Walls interactions, hydrogen bonds, electrostatic interactions, and hydrophobic interactions whereas soft biocorona proteins interact via weak protein-protein interactions. These hard and soft layers are also distinguishable depending on the exchange rates. While the soft layer is thought to be dynamic, the hard layer is stable with exchange times in the order of hours.[9]
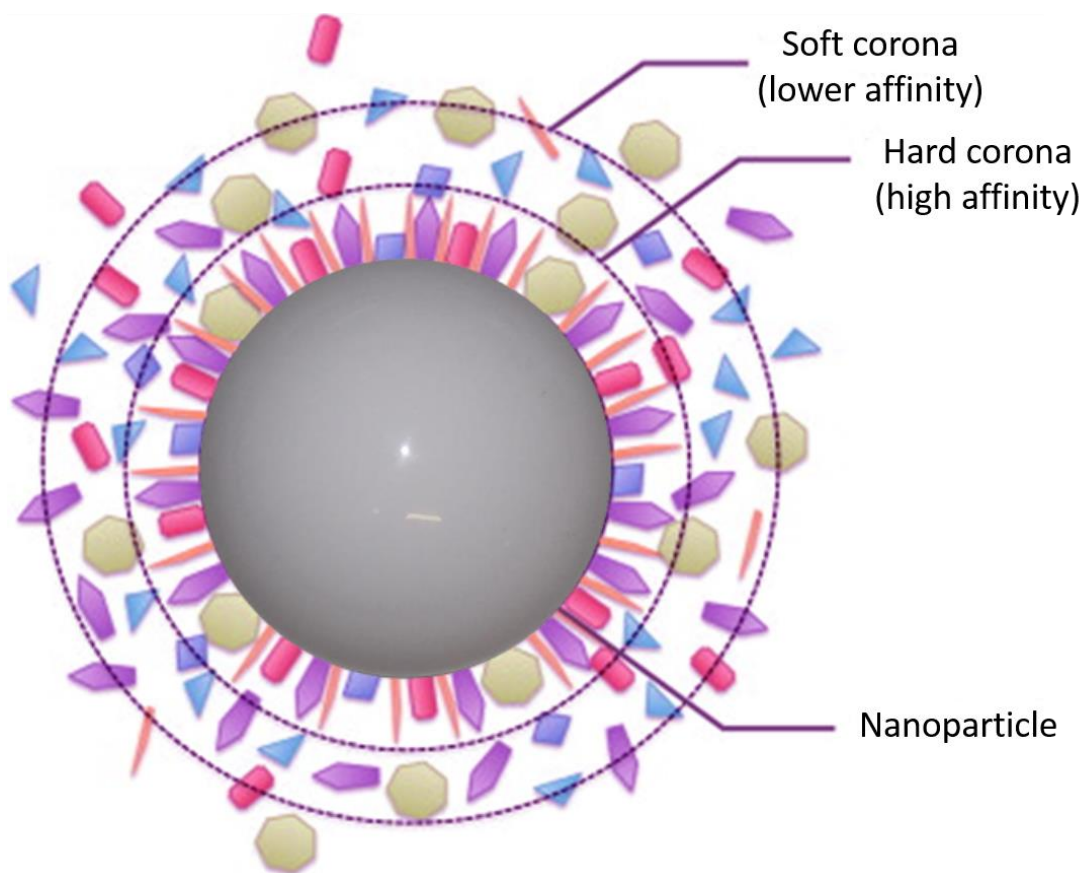
Figure 1.1.2: Depending on protein affinity for nanoparticle surface two distinguishable layers (hard and soft) are formed as shown in this schematic. The complexity of biocorona composition (both hard and soft corona) due to the availability of various proteins is illustrated with different colors and shapes here. Modified with permission from ref [2].

The nature (structure and composition) of the biocorona is found to be complex and unique for all nanomaterials dependent on several parameters such as nature of the physiological environment, exposure time, and physicochemical properties of ENMs

(composition, size, shape, surface charges, surface functional groups). It is also known that adsorbed proteins in biocorona may undergo structural rearrangement or conformational changes, which could alter protein interaction with other biomolecules. Nanoparticle composition and its surface chemistry are also found to be key in identifying binding proteins and their affinities. Hence, a thorough understanding of all factors is critical for the safe design of nanomaterials.

1.2 Relation to physicochemical properties of nanomaterials and its environment

ENMs exhibit optical, electrical, magnetic, and mechanical properties distinct from their bulk counterparts. Due to their small size, ENMs can easily cross biological barriers (e.g., blood-brain barrier) and could cause undesired biological implications. Broadly speaking, all factors affecting nano-bio interactions could be categorized under physicochemical properties of ENMs and the exposed environment as shown in **Fig. 1.2.1**.[1] These parameters have also been reviewed by other research groups.[6], [10]–[12] **Table 1.2.1** summarizes the findings for various nanoparticle properties. In this section, the role of these factors in biocorona formation and composition is presented briefly.
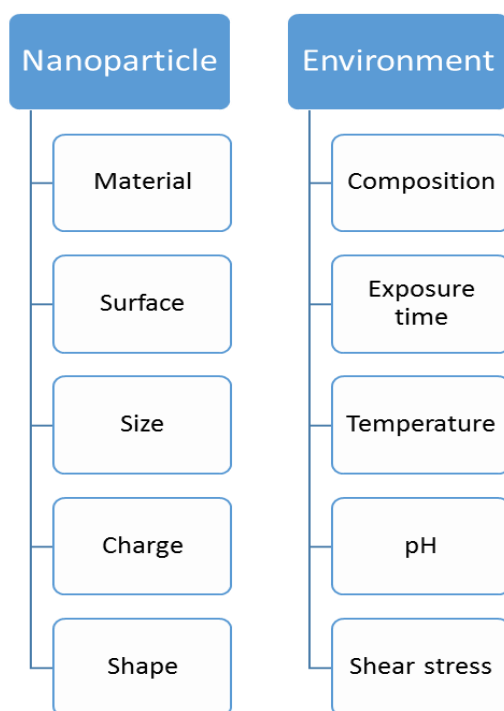
Fig 1.2.1: Important factors affecting the formation of biocorona classified under nanoparticle properties and its surrounding environment.

NP parameter	Observed effects
NP size	• Bigger size, larger degree of protein coverage • Smaller size increases corona thickness and decreases conformational change • Evolution of composition and relative abundance of adsorbed proteins
NP shape	Higher protein adsorption onto nanorods compared to nanospheres
NP surface	
Charge	• Charge affects composition of formed protein corona • More highly charged surfaces increase protein conformational changes • Protein conformation: positive > negative > neutral • Charged particles have higher cell internalization and faster opsonization rates than electrically neutral particles; positively charged NPs are incorporated by cells in higher numbers and faster than negatively charged NPs
Hydrophobicity	Higher hydrophobic NPs: • Increase adsorbed protein quantity ' and qualitatively change obtained protein adsorption patterns • Increase affinities of biomolecules • Increase protein conformational changes • Are opsonized more quickly than hydrophilic NPs
Smoothness/roughness	Surface roughness greatly minimizes repulsive interaction and influences the amount of protein, but not the protein identity

Tables 1.2.1: Effect of various nanoparticle (NP) properties on biocorona. Reproduced with permission from Nguyen et al. [1]

Surface curvature of nanoparticles (NPs) has been observed to affect the strength of protein-protein interactions. Significant changes in composition and organization of proteins in biocorona is also observed when nanoparticle size is comparable to the size of the protein.[6] Size and curvature of NPs also seem to affect binding of proteins. For instance, higher surface to volume ratio in gold nanomaterials of 30 nm diameter adsorbed more proteins than 50 nm sized nanoparticles as reported by Dobrovolskaia et al.[13] Proteins on gold nanoparticles were observed to by structurally changed (unfolded) and indeed catalyze the formation of protein aggregates.

In addition to size and shape, defects that are inevitable in ENMs also play a role in biocorona formation needs attention. Chapter 4 presents variations in biocorona due to defects in carbon nanotubes in detail. Hydrophobic surfaces have been found to adsorb more proteins compared to hydrophilic/ neutral surfaces. Proteins on hydrophobic ENMs tend to unfold in order to accommodate more proteins. Albumin molecules have been shown to adsorb more proteins on hydrophobic nanoparticles than hydrophilic counterpart albeit protein affinity roughly remaining the same.[14]

Time evolution of biocorona on different sized (4-40 nm) gold nanoparticles was carefully assessed by Casals and his group[15]. They stabilized these gold nanoparticles by coating citrate, mercaptoundecanoic for negative surface charge and aminoundecanethiol for a positive surface charge. NPs were exposed to cell culture medium containing 10% fetal bovine serum (FBS). Also they observed irreversible change in proteins over time, which confirm our present understanding. It has been reported that protein adsorption increases with increase in surface charge of NPs.[16]

Chapter 5 discusses Ag NPs (with various surface functional groups) and their interaction with apolipoprotein to form corona.

Biological environment also plays a crucial role in coronal composition and formation. Maiorano *et al.* experiments with citrate coated Au NPs with various cell culture media determined how media composition influences NP-biomolecular corona and cellular response.[17] They chose two widely used cell culture mediums DMEM and RPMI with fetal bovine serum as the protein source. Biological impacts were evaluated with several viability assays onto cell lines human epithelial cervical cancer (HeLa) and human leukemic monocyte lymphoma (U937). Interestingly, they observed DMEM induced stable and a protein-rich corona as compared to RPMI. This study confirmed nanoparticle-protein complex formation mediated in physiological environment can impact on cellular responses.

In summary, ENMs are useful for various applications including nanomedicine due to their unique properties. However, a deeper understanding of ENM-induced cytotoxic and inflammatory responses is needed before the viability of ENMs can be realized. To this end, it is imperative to understand the dependence of ENM-biocorona on ENM physicochemical properties including size, shape and surface functionality. This is highly complex because all the physicochemical properties are interrelated. As it will be discussed in the following chapters of this work, size, shape, surface charge, and defects are important in the formation and evolution of ENM-biocorona while biocorona formation itself can alter the charge and dispersion stability of the ENM system. The

complex interdependence between biorocona and ENM physicochemical properties is very hard to decouple in reality and is a major roadblock in the ability to predict ENM's toxic response based on its physicochemical properties.

CHAPTER TWO

SPECTROSCOPIC CHARACTERIZATION TECHNIQUES

The advancement of nanotechnology over the past two decades has spurred the fields of health care, information technology, energy, homeland security, food safety and transportation; and the global market for nanotechnology-related products reached more than \$200 billion in 2009 with a projected \$1 trillion per annum by 2015 (US Senate Committee, 2011).[18] Despite this enormous global market, there remain several concerns regarding the impact of engineered nanomaterials (ENMs) on biological responses in living organisms, and the environment at large.[19]–[23] A comprehensive knowledge of the ENM-biomolecular interactions is central to applications in nanomedicine, consumer goods, and other unintentional exposures. Currently, there are more than 40 nanopharmaceuticals in routine clinical use and the patents and publications on nanomedicine have been exponentially increasing.[24] Considering that nanomedicine efforts are a sudden convergence of contrasting scientific disciplines (e.g. viz., materials science, bioengineering, pharmacology), the advancement and acceptance of nanotechnology relies heavily on a holistic interdisciplinary understanding of the impact of fundamental properties of ENMs (such as their morphology, size, defects and chemical stability) on physiological and environmental systems.

Upon introduction into a biological system, ENMs rapidly associate a variety of macromolecules including proteins, peptides, amino acids, fatty acids, lipids and other organic matter forming protein biocorona. [25]–[27] The formation of the corona is not only dictated by the physicochemical properties of the ENM but also the composition of the physiological environment. [28] The addition of the corona on the surface of the ENM imparts a new distinctive interactive surface, which influences activity, deposition, clearance, and cytotoxicity. [29]–[31] The biocorona has also been shown to compromise the targeting capacity of functionalized ENMs and subsequently hinder delivery therapy. [27], [32], [33]   In addition, the inconsistencies observed between *in vitro* to *in vivo* extrapolation of ENM toxicity are likely contributable to differences in ENM-biocorona formation. [25], [34] Spectroscopic tools are ideal for exploring the biological interactions of ENMs with proteins.[6], [35], [10] As discussed in this chapter, combining spectroscopic tools with traditional toxicological studies can provide unique insights into the nano-bio interface that could be used to ultimately design benign ENMs.

2.1 Hyperspectral imaging

Gold and silver nanoparticles display a collective and resonant oscillation of surface electrons, known as plasmons, upon light excitation in the visible region (400-700 nm).   The surface plasmon resonance is highly sensitive to both nanoparticles aggregation and the dielectric constant of the environment surrounding them. In a biological medium, the presence of protein corona around nanoparticles alters the SPR

peak by modifying the dielectric constant. [36] Similarly, their cellular uptake could lead to aggregation, which is known to red-shift the SPR peak. [37] Hyperspectral imaging is an excellent tool that combines microscopy and spectroscopy in real time by accumulating reflectance spectrum for each pixel in a micrograph. Thus, the state of nanoparticles and protein corona upon cellular uptake can be gleaned from the hyperspectral micrographs.[38]–[40] Recently, we explored the cellular uptake of silver nanoparticles (Ag NPs) with and without protein corona using hyperspectral imaging.[41] Our studies revealed intracellular modifications resulting from protein corona formation as shown in **Fig. 2.1.1**. Changes in the microenvironment of AgNPs were evidently reflected in the shift of plasmon energies allowing us to differentiate between intra- and extra-cellular nanoparticles. Hyperspectral imaging presents an alternative to traditional electron microscopy methods for the identification of nanoparticles and protein corona inside the cell. [42]–[45]The exhaustive sample preparation needed for electron microscopy, such as encapsulation in a polymer followed by microtoming, often leads to artifacts. For example, the large agglomerates formed during the electron microscopy sample preparation are indistinguishable from agglomerates resulting from the loss of nanoparticles surface coating upon entering biological media.
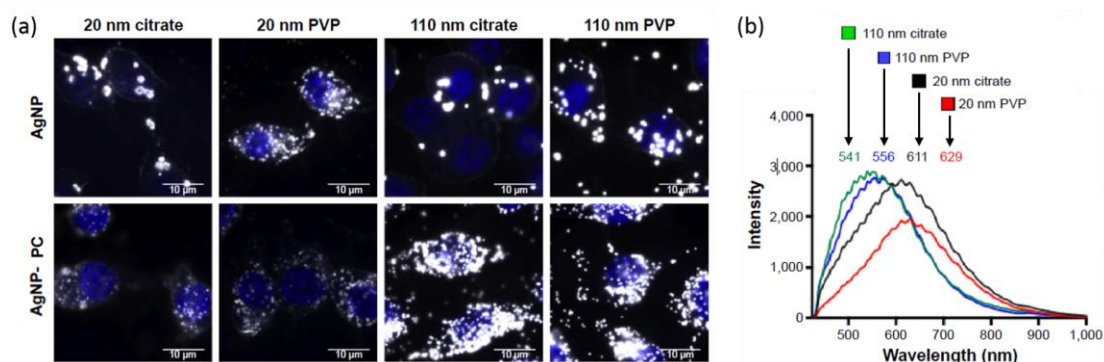
Figure 2.1.1: (a) Hyperspectral enhanced darkfield images of macrophages exposed to AgNPs and AgNPs with protein corona for 2 h, at a concentration of 25μg/mL. Macrophage nucleus appears blue in the images due to DAPI stain. (b) Differences in mean spectra for AgNPs with different sizes (20 and 110 nm) and coatings (PVP and citrate). Based on such shifts in plasmon energies, it is possible to study the uptake and modification of AgNPs using hyperspectral imaging.

2.2 Circular dichroism spectroscopy

ENM-protein complex formation poses concerns on potential denaturation of proteins, which can alter protein binding to receptors and induce inflammatory responses. Lysozyme, for example, adsorbed on gold nanoparticles (AuNPs) were observed to induce misfolded proteins which likely catalyze the formation of aggregates.[46] Similarly, fibrinogen was found to unfold on the surface of stabilized (negatively charged with polyacrylic acid) AuNPs, and bind to integrin receptor (MAC-I) leading to the inflammatory response.[47] Circular dichroism (CD) spectroscopy has been extensively used to study conformational changes in biomolecules.[48]–[50] CD studies on ENM

protein corona can elucidate the changes in protein secondary structures ensuing from their adsorption to ENMs surface.[51] For example, apolipoprotein (ApoA-I) protein, which is known to be abundant in the protein corona of metal nanoparticles, exhibited secondary structural changes dependent on the surface coating (**Fig. 2.2.1**). ApoA-I is the major lipoprotein component of high-density lipoprotein (HDL). It adopts a shape similar to a horseshoe of dimensions 12.5x8x4 nm with high α-helix content.[52]–[54] The helices in ApoA-I are predicted to be amphipathic, with the hydrophobic (/hydrophilic) face mediating lipid (/aqueous) interactions. The thermodynamic drive to minimize the aqueous exposure of the hydrophobic residues is one of the major factors in ApoA-I adsorption on AgNPs.[55], [56] We studied the interactions between ApoA-I and 100 nm AgNPs with four different coatings viz., citrate, polyvinylpyrrolidone (PVP), branched polyethyleneimine (bPEI) and lipoic acid.[57] These coatings were chosen to provide both negative (citrate, PVP, lipoic acid) and positive charged surfaces (bPEI) with different affinities for AgNPs. While lipoic acid interacts strongly through Ag-S bonds, other coatings (citrate, PVP, bPEI) are considerably weaker. As shown in **Fig. 2.2.1**, CD studies showed a significant decrease in α-helical content for all surface coatings with the complete disappearance of α−helices for AgNP-bPEI and AgNP-lipoic acid. From a physiological standpoint, we found a significant increase in the ability of ApoA-I coated AgNP-bPEI and AgNP-lipoic acid to generate reactive oxygen species due to its unfolding. The conformational changes observed in CD can provide more information on ENM-protein corona complex and may even be used as a predictor of adverse immune responses.
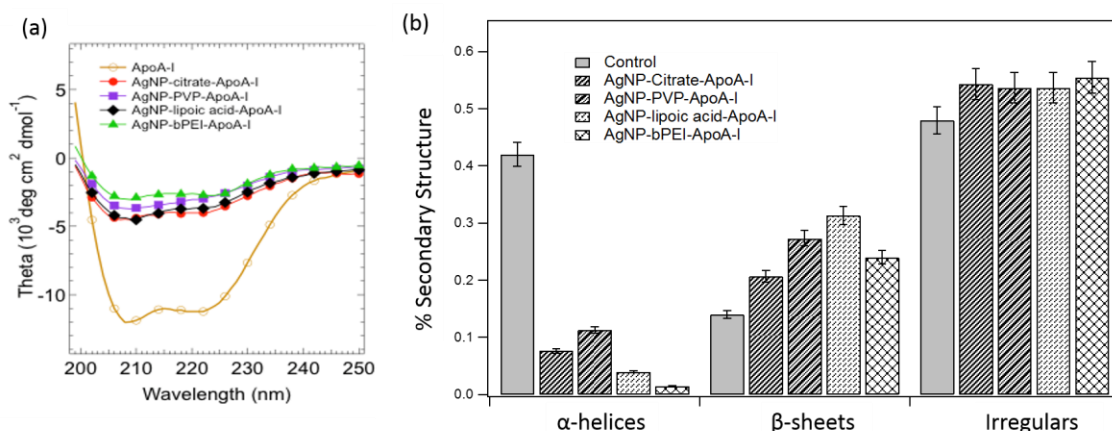
Figure 2.2.1: (a) Circular dichroism (CD) spectra for ApoA-I incubated with AgNPs of different surface coatings (citrate, PVP, bPEI, and lipoic acid) shows (b) marked decrease in α-helix content with corresponding increase in β-sheets and irregular structures. Spectra were analyzed using CAPITO (a CD Analysis & Plotting Tool) and secondary structure content was estimated. CD spectroscopy provides secondary and tertiary protein structure content estimation of biomolecules, which is critical for analyzing conformational changes during ENM-protein interactions.

2.3 Infrared spectroscopy

Unlike metal nanoparticles, carbon-based ENMs exhibit strong optical absorption <240 nm due to their π-electron system, which can interfere with protein CD spectra collected in 200-300 nm range, precluding the use of CD to study nanocarbon-protein corona. Alternatively, we used ATR-FTIR (attenuated total internal reflection- Fourier transform infrared) spectroscopy to elucidate the adsorption-induced structural changes in proteins (bovine serum albumin or BSA and fibrinogen) on carbon ENMs such as multi-

walled carbon nanotubes (MWNTs), graphene and graphene oxide nanoribbons (GNRs and GONRs). The FTIR spectrum of proteins displays two main bands, Amide I (1600-1700 cm^{-1}) and Amide II (1500-1580 cm^{-1}), arising from the amide bonds that link the amino acids in proteins. While Amide I band is mainly associated with the C=O stretching vibration, Amide II band results primarily from bending vibrations of the N—H bond. Given that both the C=O and the N—H bonds are involved in the hydrogen bonding between the different peptide units, their spectral position and intensity can be used to determine the secondary structure content of a protein. For example, as shown in **Fig. 2.3.1**, the α-helical content in BSA leads to strong adsorption ~1640-1660 cm^{-1} (dashed lines) while the lower frequency component at ~1620-1640 cm^{-1} and the peak ~1555 cm^{-1} arise from β-sheets. Clearly, the rich secondary structure of BSA (particularly, the peak relating to α-helical content) significantly disappears upon its adsorption on to all carbon-based NMs, as expected from its low internal stability. Indeed, the changes in secondary structure are higher in the case of MWNTs (i.e., complete disappearance of secondary structure) suggesting that BSA unfolds much more, relative to GNRs and GONRs, in order to adhere to the tubular MWNTs. GNR and GONR retain BSA secondary structure to a certain extent, as shown by the presence of ~1555 cm^{-1} for β-sheets. In the case of fibrinogen, the secondary structural changes are found to be higher for GONRs compared to MWNTs and GNRs plausibly due to the formation of hydrogen bonds. The α-helix peak was found to partially disappear for fibrinogen adsorbed on MWNTs and GNRs. Lastly, the structural changes for fibrinogen on GNRs seemed to be less pronounced than MWNTs possibly due to its shape. It could

be rationalized that fibrinogen must unfold more to adhere to MWNTs due to their higher curvature than GNRs. To further understand NM-BSA interactions, we also performed large-scale molecular dynamics (MD) simulations of BSA-MWNT, GNR/GONR-water systems (detailed in [58]). As shown in **Fig. 2.3.1**, we observed that proteins undergo conformational changes after initial contact (in accordance with our experimental observations, discussed in **Fig. 2.4.1**) leading to some protein regions collapsing on to the ENM surface rather than gradually spreading from the initial region of contact.
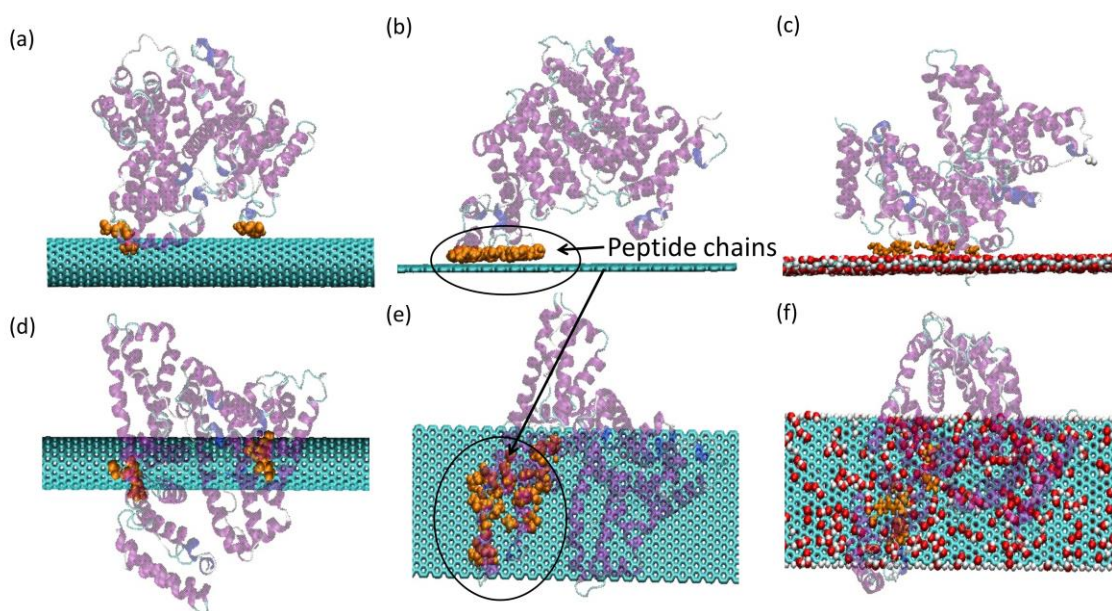
Figure 2.3.1: (a-c) Snapshots of MD simulations showing BSA on SWNT, GNR, and GONR 10 ns after adsorption. (d-f) show the top-view. The adsorption is accompanied by disruption of a-helices into random peptide chains (shown in orange).

17

2.4 Electrochemical impedance spectroscopy

Charge transfer is known to play an important role in several many physiological processes including blood clotting, vitamin absorption, and oxidative stress.[59]–[61] Differences in electronegativity between proteins and the ENM surface may induce charge transfer which, along with other perturbations in the media (e.g. pH, thermodynamic fluctuations), plays a critical role in protein denaturation, protein-protein interactions, and alterations to the cellular and extracellular redox status. Such interactions are not necessarily specific, with conformational changes possibly resulting in newly exposed charged regions and hydrophobic domains attracting or repelling other surrounding proteins or nanostructures. Electronic properties of ENMs including their band structure and density of states have been shown to regulate protein adsorption dynamics via charge transfer, which is evident as shifts in absorption and emission spectra.[62], [63]

2.4.1 Charge transfer during corona formation

The chemisorption of proteins on bulk material surfaces has been known to occur through charge transfer processes. For example, the aromatic amino acids present in BSA (tryptophan, phenylalanine, histidine, and tyrosine) could interact with the unhybridized pz orbitals of the carbon-based ENMs, via providing a weak acceptor level in the electronic density of states (DOS) to allow partial charge transfer. It may be expected that

a surface facilitating higher charge transfer at the nanoscale may lead to stronger surface-protein interactions and a subsequent increase in protein adsorption. Spectroscopic and electrochemical techniques such as micro-Raman, CD, and cyclic voltammetry can be used to analyze elucidate the influence of charge transfer on protein affinity for ENMs and the alterations in secondary and tertiary structures that occur with adsorption. Among the variety of ENMs, nanocarbons possess a strong affinity for proteins through hydrophobic and aromatic π-π stacking interactions. [64] Previously, we elucidated the charge transfer interactions between nanocarbons and proteins using micro-Raman spectroscopy. Our results show strong interactions of proteins (albumin and fibrinogen) with nanocarbons is strongly influenced by charge transfer between them, inducing protein unfolding which enhances conformational entropy and higher protein adsorption. For instance, the UV-visible absorption spectrum of single-wall carbon nanotubes (SWNTs) coated with BSA was found to blue shift significantly while BSA-coated graphene sheets (both exfoliated and synthesized via chemical vapor deposition) exhibited no such changes.[65] Additionally, micro-Raman spectroscopy revealed alterations in the structure of the G-band (or graphitic band) of BSA-coated SWNTs. The G-band, which is highly sensitive to charge transfer, was found to be upshifted with a Breit-Wigner-Fano lineshape resulting from electron transfer between BSA and SWNTs. No changes were observed for graphene upon protein coating indicating that ENMs-BSA charge transfer is unique to SWNTs. Concomitantly, FTIR spectroscopy revealed subsequent conformational changes in BSA (Figure 4) in the form of unfolding of α–helices, suggesting hard corona formation on SWNTs as opposed to graphene. These

results insinuate that disruption in electrostatics due to ENM-protein charge transfer leads to the breaking of peripheral H-bonds in the α–helices and permanent denaturation of BSA on SWNTs. [65], [66]
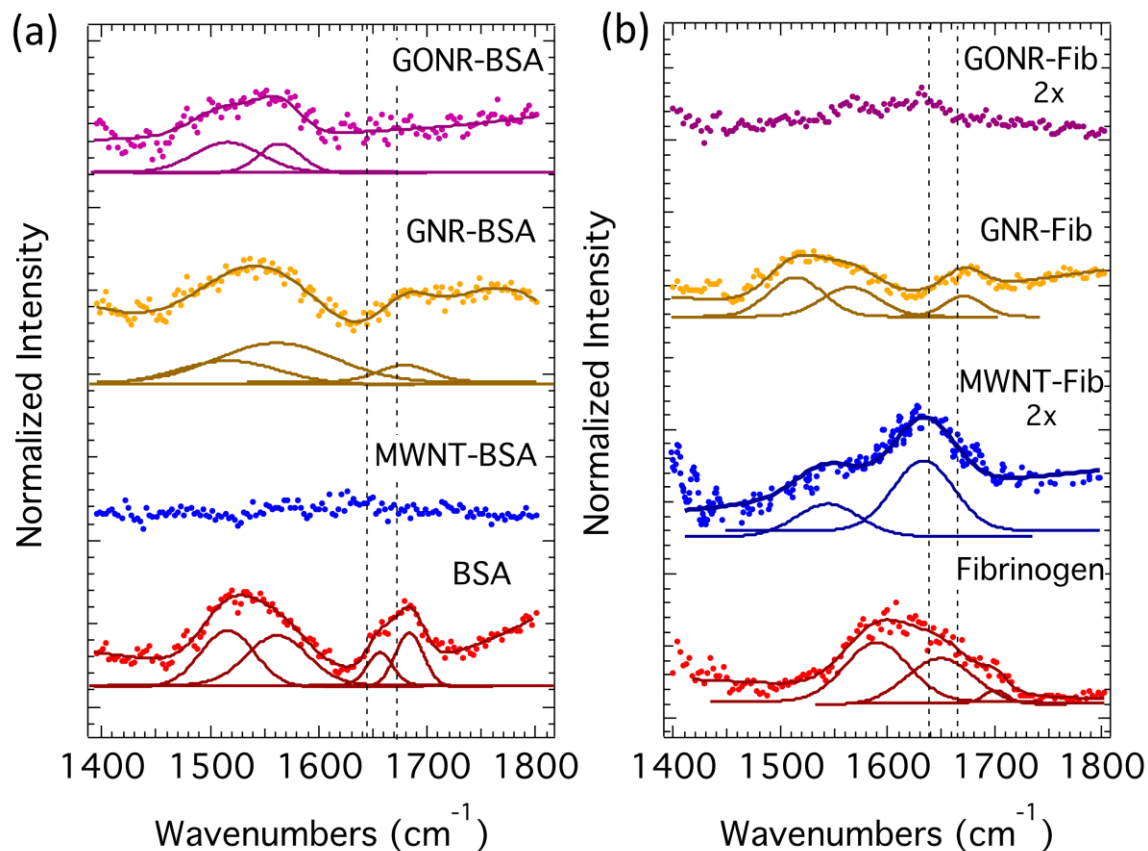
Figure 2.4.1: (a) FTIR spectra for native BSA, BSA-adsorbed on MWNTs, GNRs, and GONRs show that the CNMs significantly affected the secondary structures of the proteins. The absorption peak for α-helix in native BSA, in the range from 1640 to 1660 cm^{-1} (indicated by the vertical dashed lines), showed a significant reduction (disappeared for MWNTs) for all CNMs suggesting that the secondary structure of BSA adsorbed on CNMs was less compact. (b) In the case of fibrinogen, the loss of secondary structure

was highest for GONRs possibly due to the formation of hydrogen bonds. While both

MWNTs and GNRs exhibited a loss of α-helical content, the appearance of new peak

~1500 cm^{-1} (corresponding to random motifs) in GNRs suggested a lesser degree of

relaxation for fibrinogen, compared to MWNTs

CHAPTER THREE

EFFECT OF DEFECTS IN CARBON NANOTUBES ON CORONAL

COMPOSITION AND ITS FATE

Raghavendra, Achyut J., *et al.* "Variations in biocorona formation related to defects in the structure of single walled carbon nanotubes and the hyperlipidemic disease state." *Scientific reports* 7.1 (2017): 8382. Produced in part with permission of Nature Publisher Group.

Bai, Wei, *et al.* "Defect density in multiwalled carbon nanotubes influences ovalbumin adsorption and promotes macrophage activation and cD4$^+$ T-cell proliferation." *International journal of nanomedicine* 11 (2016): 4357. Reproduced in part with permission of International Journal of Nanomedicine.

3.1 Introduction

Successful immunotherapy requires identification of target antigens, their efficient delivery, and subsequent interaction with the antigen-presenting cells (APCs) and T cells without eliciting negative regulatory immune suppression or rejection in the host. Recently, a variety of cancer vaccines have been developed and tested in clinical studies but only a few trials obtained >5-10% partial or complete response. This may be attributed to the failure in vaccine formulation, targeted delivery, and consequent activation of the immune system.[67], [68] Alternatively, antigen-coated microparticles (e.g. 1 to 10 μm aluminum salts) have been widely used in both human and veterinary vaccines to stimulate immune responses and improve the efficacy of vaccines but only had limited success.[69] With the rapid development of nanotechnology, researchers expect to build on the unique physicochemical properties of nanomaterials to provide new alternatives for vaccine development.[70]

Among a wide variety of nanomaterials, carbon nanotubes are one of the most promising candidates for drug and antigen delivery due to their unique physicochemical properties such as the high surface area to volume ratio and delocalized pi-electron cloud. For example, recent studies have utilized CNTs to successfully deliver peptides[71], cancer testis antigen[72], and small molecular drugs[73], in various *in vitro* immune cell lines and *in vivo* animal models. CNTs are inherently hydrophobic and exhibit strong tendency to aggregate in aqueous media, which limits their use in the biomedical application. Accordingly, as-produced CNTs are often modified using wet chemical methods for adding carboxyl and hydroxyl functionalities to improve their suspension stability. Such surface modifications of CNTs are also known for reducing their toxicity and improving their ability to modulate the immune system[74][75]. In addition, our proteomics studies showed that carboxylated CNTs bind significantly more serum proteins in cell culture media than pristine nanotubes.[76] Further, carboxylated CNTs have been proposed for use in vaccine delivery due to their ability to bind protein. In general, it appears that carboxylation of CNTs enhances their biomedical applicability. However, during the process of carboxylation, surface defects are often introduced into the CNTs and it is currently unclear how these surface defects will impact CNTs used in biomedical applications such as antigen delivery for vaccines. Therefore, in this study, we investigated two carboxylated MWCNTs with different levels of surface defects.

In this work, we investigate the use of carboxylated multi-walled carbon nanotubes (MWCNTs) with two different defect densities as a vaccine delivery vehicle to deliver a specific antigen to stimulate the immune response. Carboxylated MWCNTs were loaded with ovalbumin (OVA) and delivered to bone marrow derived macrophages. These macrophages were co-cultured with OVA-specific CD4$^+$ T cells isolated from OT-II mice for 5 days. We demonstrated that OVA was abundantly absorbed on MWCNTs and was efficiently delivered into macrophages without observable toxicity. Interestingly, MWCNTs with higher defect density showed more OVA adsorption despite their low surface area. We found that MWCNT-OVA complex significantly induced the secretion of cytokines (TNFα and IL-6) and expression of MHC class II on macrophages as compared to MWCNTs alone or OVA alone. Remarkably, OVA peptides were presented on MHC class II and subsequently stimulated the robust proliferation of CD4$^+$ T cells after co-culture. In contrast, MWCNTs without OVA coating did not induce cytokine production, expression of MHC class II, nor CD4$^+$ T cell proliferation. Our work provides strong evidence for use of MWCNTs as an antigen delivery system in vaccine development.

Single walled carbon nanotubes (SWCNTs) are one-dimensional structures with unique optical and electronic properties relevant for many biomedical applications.[77], [78] Particularly, the sharp densities of electronic states at the so-called van Hove singularities (vHS) in SWCNTs impart strong resonant optical absorption and emission of visible and near-infrared light, which makes them invaluable for applications in photothermal therapy, multimodal imaging (e.g., Raman, fluorescence and

photoacoustic), and cancer drug delivery.[79], [80] While much research has focused on exploiting SWCNT properties for biomedical applications, their toxicity has been well demonstrated. Fundamental understanding of SWCNT biological interactions and mechanisms of toxicity still, however, remain elusive.[81]

In physiological environments, cells interact with the biocorona (BC), which consists of a layer of physi- and chemi-sorbed biomolecules (i.e. proteins, lipids, peptides, etc.), which inadvertently accumulate on the surface of the SWCNTs.[82]–[84] The addition of the BC alters not only the surface and properties of the SWCNT but may also modify their cellular interactions similar to what has been shown with other nanoparticles.[85]–[87] Ultimately this means that the BC can interfere with the SWCNT's function (viz., imaging or drug delivery), and alter its biodistribution, clearance, and/or toxicity. It has been demonstrated that the physicochemical properties of nanomaterials in general influence the formation and the content of BC, however, the impact of structural defects have not been fully evaluated.[88], [89] The formation of BC on SWCNTs, however, is more fundamentally intriguing due to the presence of vHS in its electronic structure.

Previously, we showed that the vHS in SWCNTs leads to unexpected charge-transfer interactions with proteins such as fibrinogen and could lead to undesired thrombosis.[65] The electronic structure of SWCNTs is highly sensitive to defects, which are often unintentionally introduced in SWCNTs while processing them through mechanical or chemical functionalization for biological applications.[90], [91] The presence of defects alters SWCNT biomolecular interactions through charge-transfer

interactions and could ultimately change the composition of BC. Understanding BC compositional differences due to defects in SWCNTs will allow for new avenues of control regarding BC formation to be explored resulting in regulation of biological response.

To enable the safe and effective use of CNTs in nanotechnologies it is essential to evaluate differences in the BC that forms under these increasingly prominent disease states. In the current evaluation of the BC, we hypothesized that the defects in SWCNTs will result in differential association of biomolecules forming the BC. Additionally, we hypothesized that disease-associated differences in the physiological media would also alter BC formation. To examine the role of defects and a high cholesterol environment on the formation of the SWCNT-BC we utilized a quantitative proteomics approach with label-free mass spectrometry. We prepared SWCNTs with different defects using a planetary ball-milling approach. The defects in SWCNTs were characterized using a comprehensive array of tools including transmission electron microscopy, Raman and photoluminescence spectroscopy, and gas-adsorption isotherms. We observed that increased ball-milling time of SWCNTs resulted in more defects introduced in the structure of SWCNTs. Following incubation in normal mouse serum, quantitative label-free mass spectrometry identified differences in the biomolecular content of the BC resulting from the ball-milling process. Further, incubation in cholesterol-rich mouse serum resulted in the formation of unique BCs compared to SWCNTs incubated in normal serum. Ultimately our study demonstrates that the BC is modified due to physicochemical modifications in SWCNT structure induced by ball-milling and due to

physiological disease conditions. These alterations in the BC may result in variable biological responses.

3.2 **Materials and methods**

3.2.1 Preparation and characterization of MWCNT-ovalbumin complex

Pristine MWCNTs with two different sizes were obtained from Cheap Tubes Inc, including MWCNT-2 (10-20 nm, 0.5-2 μm) and MWCNT-30 (10-20 nm, 10-30 μm). Pristine MWCNTs were carboxyl functionalized according to the previous method (17). Size and morphology of carboxylated MWCNTs were evaluated by transmission electron microscopy (TEM) using a Hitachi 7600 (Hitachi Group). Diameter and length measurements were performed on $\geq$ 100 CNTs. Ovalbumin was purchased from Sigma and dissolved in PBS at 1 mg/mL. To generate MWCNT-OVA complex, 200 μL of carboxylated MWCNT (1 mg/mL), 500 μL of ovalbumin solution (1 mg/mL) and 700 μL of distilled water were mixed and incubated on a rotator overnight at 4 °C. The mixture was centrifuged (14,000 rpm, 10 min, 4°C) and the pellets were washed twice to remove non-adsorbed ovalbumin. After wash, the pellets were re-suspended in distilled water at 1 mg/mL. The hydrodynamic size and zeta potential of either MWCNT or MWCNT-OVA complex were determined using a Zetasizer Nano ZS (Malvern Instruments). The surface area measurements were performed on a Quantachrome Autosorb iQ gas sorption analyzer using N2 gas. Raman characterization of MWCNTs was performed using a Renishaw InVia microscope coupled to 514.5 nm Ar+ laser.

To quantify the amount of ovalbumin bound to MWCNTs, the mixture used for the formation of MWCNT-OVA complex was centrifuged (14,000 rpm, 10 min, 4°C) and the supernatant was collected. The concentration of ovalbumin in the supernatant was determined by Pierce BCA protein assay, which was subtracted from the initial concentration of ovalbumin in the original mixture to calculate the amount of ovalbumin bound to MWCNT. The measurement was conducted at least three times.

3.2.2 Synthesis and characterization of SWCNTs.

SWCNTs were prepared using chemical vapor deposition.27 An MTI planetary ball mill was used to induce defects in SWCNTs. High-resolution transmission electron micrographs were obtained using Hitachi H-9600. A Renishaw InVia micro-Raman (coupled to 514.5 nm Ar+ laser) and Bruker IFS V/66 FT-Raman equipped with Nd:YAG 1064 nm was used to obtain the Raman and PL spectra of SWCNTs. The surface area of SWCNTs was characterized using Quantachrome Autosorb instrument. All the spectroscopic measurements were performed in triplicates.

3.2.3 Animals and cell models

Male C57BL/6J mice were purchased from The Jackson Laboratory (Bar Harbor, ME) at 8-10 weeks of age. Breeding colonies of OT-II transgenic mice were also acquired from The Jackson Laboratory (Bar Harbor, ME), and maintained in the animal facility at the University of Colorado-Anschutz Medical Campus. OT-II transgenic mice

express the mouse alpha-chain and beta-chain T cell receptor that pairs with the CD4$^+$ co-receptor and is specific for chicken ovalbumin peptides (OVA$_{323-339}$). All animal procedures were performed with approval and in accordance with the guidelines of the University of Colorado-Anschutz Medical Campus Institutional Animal Care and Use Committee.

Male C57BL/6J mice were sacrificed and the femur bones were collected. Bone marrow cells were flushed aseptically from the dissected femurs using a 25-gauge needle. The cells were incubated in RPMI 1640 medium supplemented with 10% fetal bovine serum (FBS), 100 U/mL penicillin, 100 μg/mL streptomycin, 2 mM L-glutamine, 1 mM sodium pyruvate, 5 μM 2-mercaptoethanol, which is referred to the complete medium. And the complete medium was supplemented with 10 ng/mL recombinant mouse macrophage-colony stimulating factor (M-CSF, R&D systems, Minneapolis, MN). The cells were incubated in a humidified incubator at 37 °C in 5% CO_2. On Day 4, the medium was replaced with complete medium supplemented with 5 ng/mL M-CSF. Bone marrow derived macrophages were used following 7 days of culture and were found to be >90% macrophages by expression of F4/80 antigen using monoclonal anti-mouse PerCP-Cyanine5.5-conjugated F4/80 antibody (eBioscience, Inc).

On the same day when macrophages were treated with MWCNTs, OT-II transgenic mice were sacrificed and the spleen was collected. A single cell suspension of splenocytes was obtained using a tissue dissociator (Miltenyi Biotec, Inc.), and red blood cells were removed from the splenocytes using Mouse Erythrocyte Lysing Kit (R&D,

Systems). CD4$^+$ T cells were enriched using mouse CD4$^+$ T Cell Enrichment Column Kit according to the manufacturer's procedure (R&D, Systems).

We employed fluorescent Texas Red-conjugated ovalbumin (TR-OVA) to form MWCNT-TR-OVA complex to confirm the successful delivery of MWCNT-OVA complex into macrophages using enhanced darkfield fluorescent imaging microscopy (Cytoviva, Inc. Auburn, AL). Macrophages were treated with 25 μg/mL of either MWCNT or MWCNT-TR-OVA complex in chamber slides using the serum-free medium. The use of serum-free DMEM is to prevent the binding of additional serum proteins to either MWCNTs or MWCNT-OVA complex. Following 6 h exposure, macrophages were washed with PBS and fixed with 4% paraformaldehyde for 10 min at room temperature. The nuclei were stained with DAPI. The cells were imaged using enhanced darkfield fluorescent microscopy (Cytoviva). The experiments were repeated at least three times.

Macrophages were treated with 25 μg/mL of either MWCNTs or MWCNT-OVA complex for 6 hours and were washed and incubated up to 5 days in complete medium supplemented with 5 ng/mL M-CSF. On Day 1, Day 3 and Day 5, the supernatants were collected for measurement of TNFα and IL-6 production using ELISA according to the manufacturer's protocol (R&D systems). For MHC class II expression, macrophages were detached using 0.025% trypsin and re-suspended in staining buffer (Invitrogen). Rat monoclonal PE/Cy5-conjugated anti-MHC class II (PE/Cy5) antibody (Abcam) was used to detect MHC class II expression on macrophages using flow cytometry. Prior to labeling MHC class II molecules, macrophages were pre-incubated with purified anti-

mouse CD16/CD32 mAb (BD Pharmingen) to reduce Fc receptor-mediated nonspecific binding. Ovalbumin was used as a positive control. The experiments were conducted independently on a minimum of three different batches of BMDMs.

In order to investigate if the ovalbumin delivered by MWCNTs has the ability to stimulate CD4$^+$ T cell proliferation, CFSE-labeled CD4$^+$ T cells were co-cultured with macrophages loaded with MWCNT-OVA complex for 5 days. Briefly, macrophages were treated with 25 μg/mL of either MWCNTs or MWCNT-OVA complex in the serum-free medium for 6 hours, and were washed and co-cultured with CD4$^+$ T cells labeled with the fluorescent dye 5,6-carboxyfluorescein diacetate succinimidyl ester (CFSE) (Thermo Fisher Scientific) for 5 days in the complete medium supplemented with 5 ng/mL M-CSF. The ratio of T cells to macrophages was 2:1. After 5-day co-culture, both macrophages and CD4$^+$ T cells were detached using 0.025% trypsin and re-suspended in the staining buffer. CD4$^+$ T cells were then immunostained with APC-conjugated mouse anti-CD4$^+$ antibody (eBioscience) to distinguish them from macrophages. The proliferation of CFSE-labeled CD4$^+$ T cells by CFSE dilution was analyzed using flow cytometry (Accuri^{TM} C6 Flow Cytometer, BD Biosciences, Ann Arbor, MI) and FCS Express 4 software (De Novo Software, Glendale, CA). The experiments were repeated at least three times.

All graphs and statistical analysis were performed using Prism 6 software (GraphPad, San Diego, CA). Statistical significance was analyzed by one-way analysis of variance (ANOVA) with differences between groups assessed using Dunnett's post hoc

tests. Differences were considered statistically significant when $p < 0.05$. Refer Chapter 4.2.5 section for methods on formation and evaluation of SWCNT-biocoronas.

3.3 Results and discussion

3.3.1 Case of MWCNTs
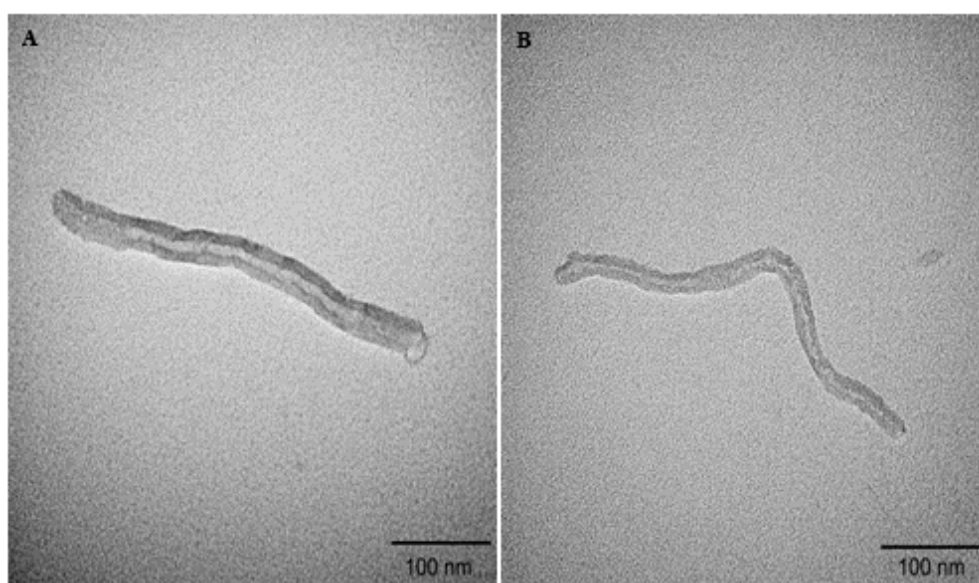
Figure 3.3.1: TEM analysis of carboxylated MWCNT-2 (A) and MWCNT-30 (B). The outer diameters of carboxylated MWCNT-2 and MWCNT-30 were 26 ± 5 nm and 18 ± 3 nm, respectively. The average length of both carboxylated MWCNTs was ~500 nm.

As **Fig. 3.3.1** shows TEM images of two carboxylated MWCNTs in their dry state. The size analysis indicated that the outer diameters of carboxylated MWCNT-2 and MWCNT-30 were 26±5 nm and 18±3 nm, respectively, which are roughly consistent with the manufacturer specifications. The average length of both carboxylated MWCNTs

was found to be ~500 nm, which is much shorter than the manufacturer specifications. We surmise that the functionalization process for adding carboxyl groups resulted in the observed reduction in length due to breaking at the defect site.[92] Our gas sorption measurements showed that the MWCNT-2 and MWCNT-30 samples have surface areas ~215 m^2/g and 94 m^2/g, respectively. The Raman spectra of MWCNT-2 and MWCNT-30 showed the presence of the so-called disorder or D-band (~1350 cm^{-1}) along with the characteristic graphitic or G-band (~1580 cm-1) (**Fig. 3.3.2**). Both the samples also exhibited at a higher frequency shoulder to the G-band (known as the D' band ~1620 cm^{-1}) suggesting high defect densities in the samples. The ratio of D- to- G band areas (I_D/I_G) was calculated to be 0.97±0.1 and 1.37±0.2 for MWCNT-2 and MWCNT-30, respectively, showing that MWCNT-30 samples contain more defects.

To understand the ability of MWCNTs to deliver ovalbumin, it is important to quantitatively determine the amount of ovalbumin bound to MWCNTs. The amount of ovalbumin bound to MWCNT-2 and MWCNT-30 was 582 ± 41 μg/mL (~0.582 mg OVA per 1 g CNTs, 0.271 ng OVA per cm^2 of CNTs) and 1066 ± 182 μg/mL (~1.066 mg OVA per 1 g CNTs, 1.12 ng OVA per cm^2 of CNTs), respectively. This difference may be rationalized in terms of higher defect density (as seen from Raman spectra in **Fig. 3.3.2**) in the case of MWCNT-30 samples. Such an observation is in agreement with our previous experimental and theoretical studies, which show that the defects strongly influenced biomolecular adsorption.[91]
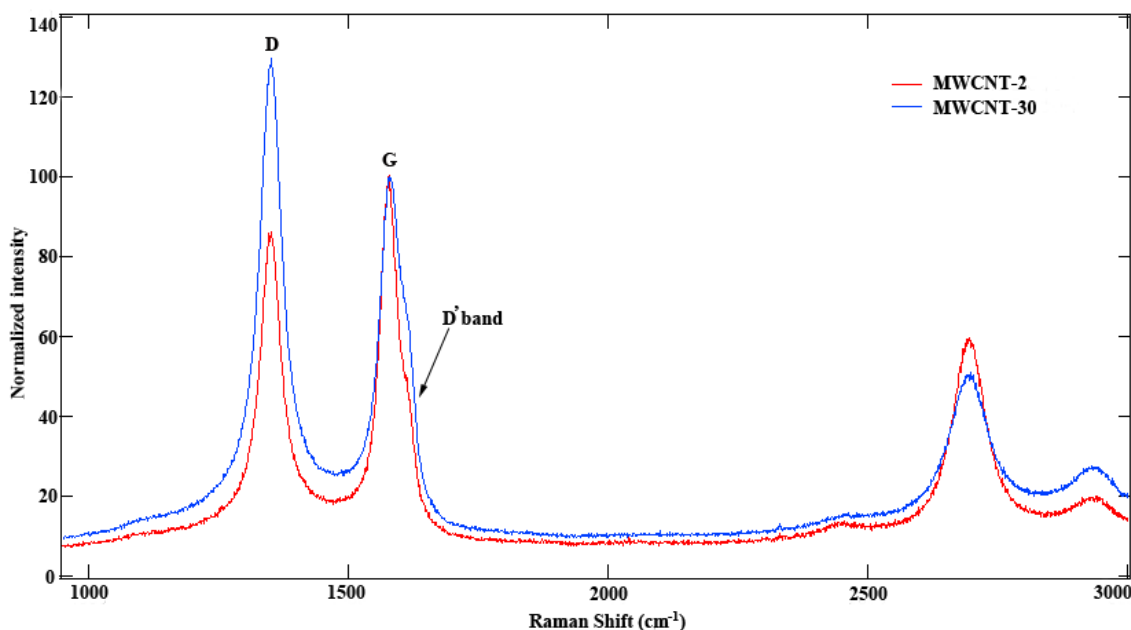
Figure 3.3.2: The Raman spectra of carboxylated MWCNT-2 and MWCNT-30. The D-band (~1350 cm^{-1}) was found along with the characteristic G-band (~1580 cm^{-1}). Both MWCNTs also exhibited at a higher frequency shoulder to the G-band (known as the D' band ~1620 cm^{-1}) suggesting high defect densities in MWCNTs. The ratio of D- to- G band areas (I_D/I_G) was 0.97 and 1.37 for MWCNT-2 and MWCNT-30, respectively, indicating that MWCNT-30 samples contain more defects.
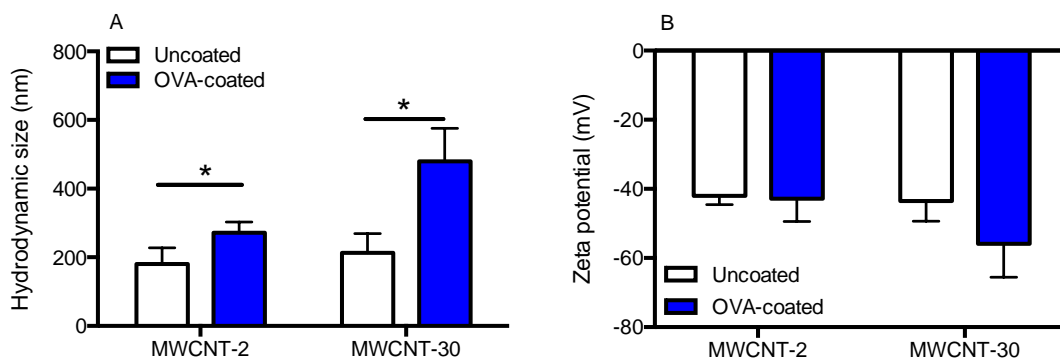
Figure 3.3.3: Effects of ovalbumin coating on the hydrodynamic size and zeta potential of MWCNTs. (A) Ovalbumin coating increased the hydrodynamic size of MWCNTs (A) but had little impact on the zeta potential of MWCNTs (B). (n=3, mean ± SD, * p>0.05 comparison between MWCNTs with and without ovalbumin coating)

TEM characterization showed the length of MWCNTs in a dry state, however, MWCNTs undergo a certain degree of agglomeration upon dispersion. We measured the hydrodynamic size and zeta potential of MWCNTs using dynamic light scattering (DLS). DLS measurement showed the similar hydrodynamic size (~200 nm) of MWCNT-2 and MWCNT-30 due to agglomeration (**Fig. 3.3.3A**). As expected, MWCNT-OVA complex showed a significant increase in hydrodynamic size than uncoated MWCNTs. Ovalbumin coating increased the size of MWCNT-30 to a greater degree than MWCNT-2 (Figure 3A) concomitant with the amount of bound ovalbumin. In addition, though both MWCNT-2 and MWCNT-30 have the similar zeta potential (**Fig. 3.3.3B**), we found that ovalbumin coating slightly decreased the zeta potential of MWCNT-30 (**Fig. 3.3.3B**) but not MWCNT-2 resulting in a more negatively charged MWCNT-30.

We used photoluminescence (PL) spectroscopy to study the effect of defects on the adsorption of ovalbumin on MWCNTs. The aromatic amino acid content in OVA absorbs light strongly at ~280 nm and emits at ~338 nm, and a standard curve was established in terms of the intensity of the emission peak (~338 nm) in OVA (**Fig. 3.3.4A**). We observed clear differences between all MWCNT-2 and MWCNT-30 samples in both pristine and functionalized forms (**Fig. 3.3.4B** and **3.3.4C**). Indeed, in the

case of MWCNT-30, we found that OVA adsorption deviates from a linear trend (shown by the dashed black line in **Fig. 3.3.4B and 3.3.4C**) at higher concentrations. On the other hand, MWCNT-2 exhibited Langmuir-like isotherm (see inset in **Fig. 3.3.4B**) in both pristine and carboxylated forms. The results indicated that while carboxylated MWCNT-2 and MWCNT-30 showed similar adsorption at lower concentrations, both trends deviated from linearity albeit in different directions (shown by dashed black line) at higher concentrations.
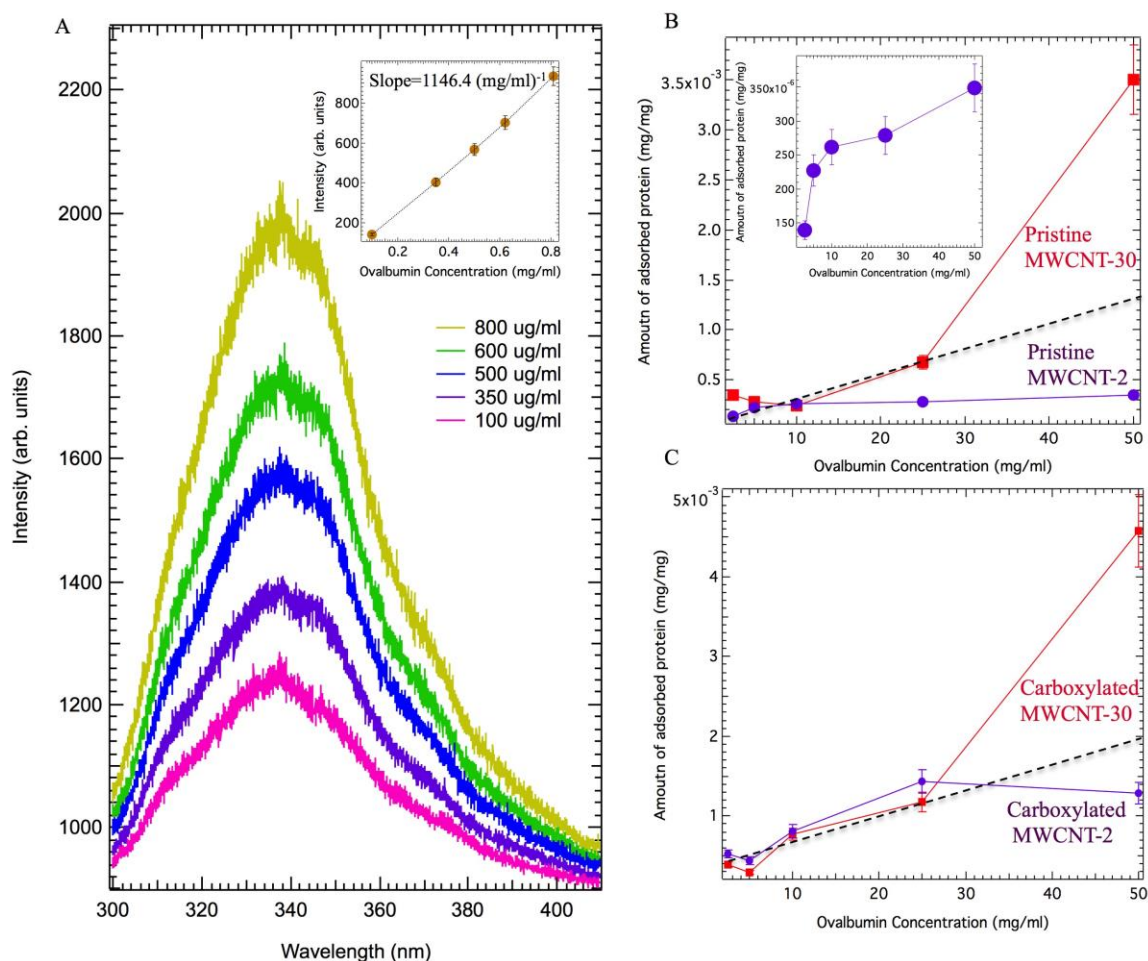
Figure 3.3.4: Binding of OVA to MWCNTs confirmed by photoluminescence spectroscopy.

To demonstrate the successful delivery of ovalbumin by MWCNTs into macrophages, we employed darkfield microscopy in conjunction with fluorescent Texas Red-conjugated ovalbumin to confirm the uptake of MWCNT-TR-OVA complex by macrophages (**Fig. 3.3.5**). After 6 h treatment, macrophages treated with or without MWCNTs alone did not show any fluorescence. In comparison, macrophages treated with ovalbumin showed fluorescence, and most interestingly, macrophages treated with MWCNT-TR-OVA complex displayed strong fluorescence, suggesting that both MWCNT-2 (**Fig. 3.3.5**) and MWCNT-30 successfully delivered ovalbumin into macrophages.
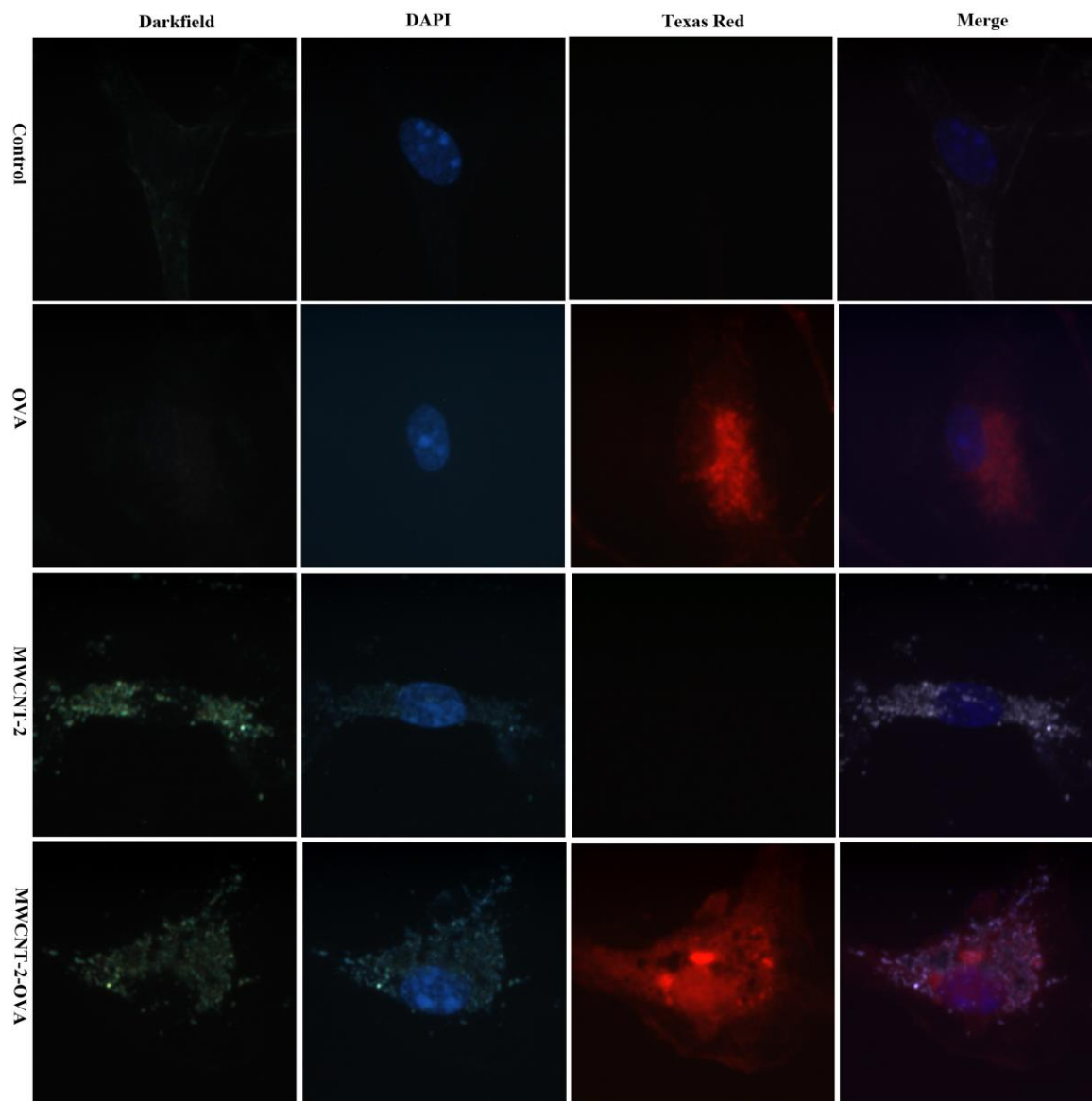
Figure 3.3.5: Delivery of fluorescent Texas Red-conjugated ovalbumin by MWNCT-2 into bone marrow derived macrophages (BMDM) visualized by darkfield and fluorescent microscopy. Macrophages with or without treatment with MWCNTs alone showed no fluorescence, but macrophages treated with ovalbumin and MWCNT-TR-OVA complex displayed strong fluorescence. (Magnification: 100 X)

We found that neither MWCNTs nor MWCNT-OVA complex had an impact on cell viability of macrophages up to 5 days using MTS assay (**Fig. 3.3.6**). We further investigated whether MWCNT-OVA complex activated macrophages. Classically activated macrophages are characterized by the production of pro-inflammatory cytokines, such as TNFα and IL-6, and the expression of MHC class II.[93] Ovalbumin alone remarkably induced the production of both TNFα and IL-6 up to 5 days after treatment while MWCNT-2 and MWCNT-30 alone had no effect on the production of TNFα and IL-6 by macrophages (**Ref.** [94]). Interestingly, both MWCNT-2-OVA and MWCNT-30-OVA complexes induced significantly higher production of both TNFα and IL-6 after treatment compared to ovalbumin treatment alone. Importantly, MWCNT-30-OVA complex induced a greater cytokine production compared to MWCNT-2-OVA complex due to higher OVA adsorption.
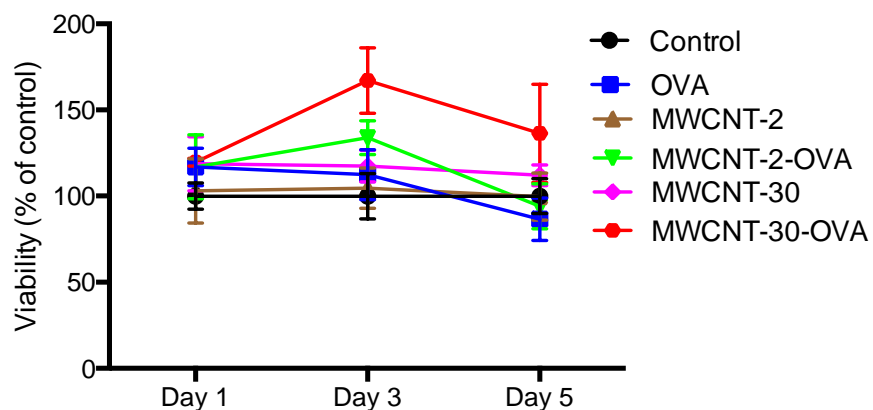
Figure 3.3.6: Effects of MWCNTs or MWCNT-OVA complex on cellular viability of BMDM using MTS assay (n=6, mean ± SD). MWCNTs or MWCNT-OVA complex showed no observable effect on the cellular viability of macrophages up to 5 days.

As demonstrated above, macrophages were effectively activated by MWCNT-OVA complexes. Therefore, we further investigated whether these activated macrophages, in turn, enhanced CD4$^+$ T cell proliferation using ovalbumin-specific CD4$^+$ T cells isolated from OT-II mice. We co-cultured CFSE-labeled OT-II CD4$^+$ T cells with macrophages treated with either MWCNTs or MWCNT-OVA complex. As expected, ovalbumin alone induced CD4$^+$ T cell proliferation (**Fig. 3.3.7A**). Interestingly, we found that both MWCNT-2-OVA complex and MWCNT-30-OVA complex significantly induced the proliferation of CD4$^+$ T cells, but MWCNT alone had no impact on CD4$^+$ T cell proliferation (**Fig. 3.3.7B and C**). We also found that MWCNT-30-OVA complex induced greater CD4$^+$ T cell proliferation than MWCNT-2-OVA complex, supported by the observation that there were six distinguished generations of CD4$^+$ T cells with MWCNT-30-OVA complex, but only 4 with the others (ovalbumin or MWCNT-2-OVA complex).
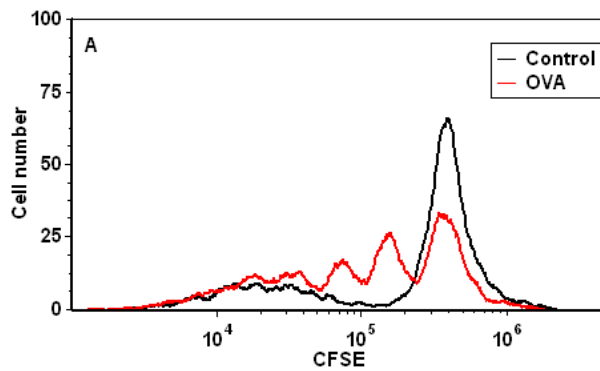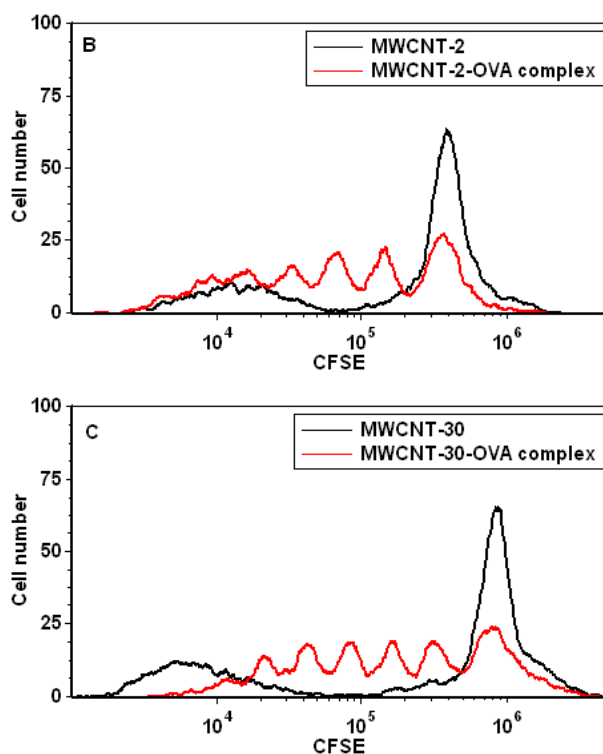
Figure 3.3.7: MWCNT-OVA complex remarkably induced CD4$^+$ T cell proliferation. (A) Proliferation of OT-II CD4$^+$ T cells after co-culture with untreated macrophages (black line) and ovalbumin-treated macrophages (red line), (B) proliferation of OT-II CD4$^+$ T cells after co-culture with macrophages treated with MWCNT-2 (black line) and MWCNT-2-OVA complex (red line), and (C) proliferation of OT-II CD4$^+$ T cells after co-culture with macrophages treated with MWCNT-30 (black line) and MWCNT-30-OVA complex (red line).

3.3.2 Case of single-walled carbon nanotubes

SWCNTs were generated using a previously described chemical vapor deposition (CVD) process.[95] The Raman spectrum of SWCNTs displays a unique radial breathing

41

mode (RBM), which could be used to accurately determine the diameter distribution. As shown in **Fig. 3.3.8A**, the Raman spectra of as-prepared SWCNTs at two excitation wavelengths (514.5 and 1064 nm) showed RBMs between 150-180 cm^{-1} indicating a sharp diameter distribution ~1.3-1.6 nm. Ball milling is expected to induce structural defects by opening SWCNT end caps in addition to creating atomic vacancies and non-hexagonal rings in SWCNTs. Indeed, it has been previously shown that intensive ball milling for ~50 h completely disrupts SWCNT tubular structure leading to multi-layered polyaromatic carbon materials.[96] Accordingly, the ball milling time in this study was limited to ~8 h to induce defects while retaining the tubular structure of SWCNTs. The Raman spectrum of SWCNTs also was used to quantify the defect density based on the ratio of the disorder (or D-band) to graphitic band (or G-band) intensity (**Fig. 3.3.8B**). From **Fig. 3.3.8B** and **C**, it is evident that the D-to-G band intensity ratio (I_D/I_G) increased with increasing ball milling time from 0.16 in as-prepared SWCNTs to ~1.5 in 8 h ball milled samples. While SWCNTs ball milled for 2 h showed a rapid increase in I_D/I_G ratio, higher ball milling times (4, 6, and 8 h) led to monotonic increase that appeared to be saturated ~8 h (Figure 1B: I_D / I_G Ratio). All ball milled SWCNTs were found to retain their tubular structure, as evidenced by the photoluminescence (PL) spectra and TEM (Fig. 3.3.8C). The presence of the van Hove singularities (vHS) in SWCNT-electronic density of states results in strong PL emission in the infrared region.29 As shown in Fig. 3.3.8C, a strong PL emission was observed for all SWCNTs ~1560 nm when excited at 1064 nm. This observation suggests that the one-dimensional tubular structure of SWCNTs, necessary for the presence of vHS, was retained in all the ball milled samples.

The ball milling process is known to increase the specific surface area of SWCNTs through structural defects. To ascertain such changes in surface area, N2 gas adsorption experiments were performed. The surface area was found to have a monotonic increase with ball milling time up to 6 h (**Table 3.3.1**). Indeed, the surface area for 6 h ball milled SWCNTs was found to increase by almost an order of magnitude. The significant decrease in surface area of 8 h-ball milled SWCNTs could be attributed to the formation of amorphous carbon that gets compacted during the milling process.
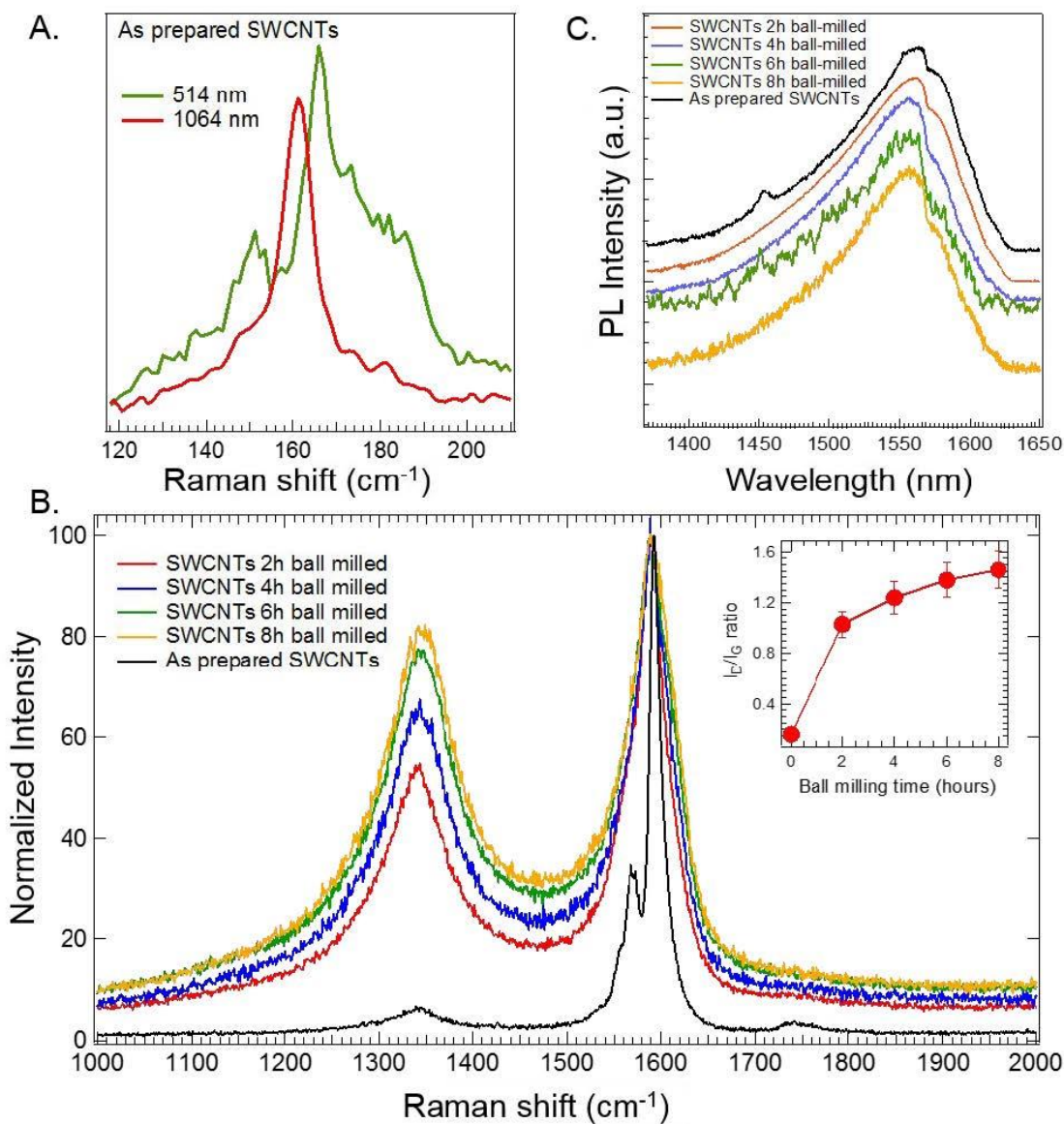
Figure 3.3.8: A. Radial breathing modes from the Raman spectra of As Prepared SWCNTs suggest a diameter distribution ~1.4 nm. The spectra were collected using both 514 and 1064 nm to probe all SWCNT populations. B. Alterations in the defect band (D-band ~1350 cm-1) in ball milled SWCNTs evidenced by their Raman spectra. All the

spectra were normalized to the graphitic or G-band to obtain the I_D/I_G ratio that is indicative of the defect density. Also, plot of I_D/I_G vs. duration of ball milling (inset) shows that there is an initial rapid increase for 2 h ball milling followed by a saturation in the defects with increasing ball milling time. The spectra shown in A and B are averaged over at least three different sets. C. The photoluminescence spectra of As Prepared and ball milled SWCNTs showed an emission peak ~1560 nm. The presence of strong emission, unique to the tubular structure of SWCNTs, confirms that the defects were introduced while still retaining the tubular morphology. All characterization experiments were performed with an $n \geq 3$.

SWCNTs	Surface Area
As Prepared	169.668 m^2/g
2 h ball milled	301.728 m^2/g
4 h ball milled	351.015 m^2/g
6 h ball milled	1091.402 m^2/g
8 h ball milled	118.165 m^2/g

Table 3.3.1: Alterations in the surface area of SWCNTs due to ball milling measured by BET analysis.

Serum from mice fed a normal western diet were collected to evaluate the biocoronas that formed on SWCNTs. Specifically, following incubation in 10% normal serum, individual biocoronal proteins on SWCNTs were identified utilizing label-free mass spectrometry. This approach allowed for the identification of specific proteins included in the biocoronas of SWCNTs following incubation in normal serum. Following identification and assessment of relative quantitative differences between protein components of the biocorona we evaluated alterations in the biocorona due to ball milling (As Prepared vs Ball milled in normal serum). These comparisons for investigation were determined based on the common processing of SWCNTs by ball milling for manufacturing and the significant portion of our population that exist with hyperlipidemia. Ultimately, these comparisons describe differential biological interactions that may occur due to typical alterations in SWCNT structure.
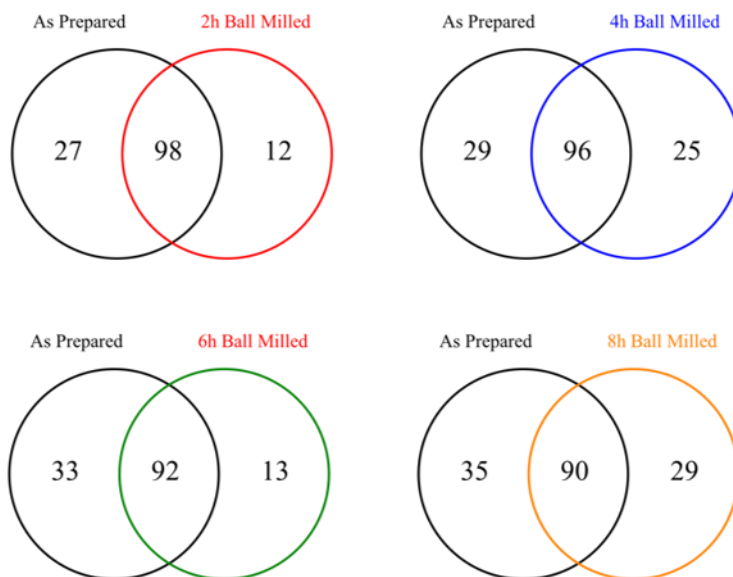
Figure 3.3.9: Venn diagrams representing the number of proteins found to associate with SWCNTs following incubation in 10% normal serum comparing As Prepared SWCNTs to SWCNTs that have undergone ball milling.

Ball milling of SWCNTs is a typical technique utilized in manufacturing that will likely alter biomolecule interactions. To evaluate these ball-milled induced changes we compared the protein components of the biocorona following incubation in normal serum. The identity of the majority of proteins forming the normal biocorona was found to be unchanged due to ball milling (**Fig. 3.3.9**). These commonly identified proteins that did not vary due to ball milling included alpha-2-HS-glycoprotein, complement C3, fibrinogen, fibronectin, plasminogen, serum albumin and others in the normal biocorona. These proteins are similar to our evaluations in Chapter 4 of the proteins of the biocorona

that form on multi-walled carbon nanotubes of differing characteristics and Fe_3O_4 nanoparticles. These shared proteins are likely associated with the engineered nanoparticles due to their relatively high abundance in serum. Although many proteins found to associate with SWCNTs were common between as-prepared SWCNTs and ball milled samples, there were a number of unique protein components within each BC. Specifically, ball milling, in general, resulted in the association of platelet-like factor 4, serum amyloid, carboxylesterase 1C, metalloproteinase inhibitor and others during incubation in normal serum. Ball milling also resulted in the unique association of apolipoprotein B-100, platelet-like factor 4, glutathione peroxidase, phospholipid transfer protein, alpha-2 antiplasmin and others during incubation in hyperlipidemic serum. Interestingly, many proteins unique to the biocorona of ball milled SWCNTs in normal serum, are known to function through redox and charge transfer mechanisms. For instance, glutathione peroxidase converts H_2O_2 into water through charge transfer reaction while metalloproteinase inhibitors chelate metal ions.[97] Upon ball milling, the defects created in SWCNTs are often charged with exoelectrons and the Ni catalyst used in SWCNTs synthesis may be exposed, unlike as-prepared SWCNTs.[98] It is plausible that the charged defects and exposed metal catalyst increased the affinity for unique proteins observed in the biocorona.

Further, for samples incubated in normal serum, fewer proteins were found to be in common between As-Prepared and ball milled samples as the length of ball milling time was extended (**Figure 3.3.9**). This suggests that a more diverse biocorona may form on the surface of SWCNTs as a result of ball milling since fewer proteins are found in

common as ball milling time is increased. While the majority of proteins identified were found to be in common between As Prepared and ball milled samples it is likely that these minor changes in protein identity may influence biological responses as shown in the literature with silver nanoparticles. For example, serum albumin is the primary component of the biocorona that forms on silver nanoparticles due to its abundance. However, when the inflammatory response by macrophages was evaluated following exposure to either silver nanoparticles with a biocorona that only consisted of albumin or a complex biocorona differences were evident.[99] This suggests that minor changes in the identity of the biocorona can elicit significant changes in biological responses.
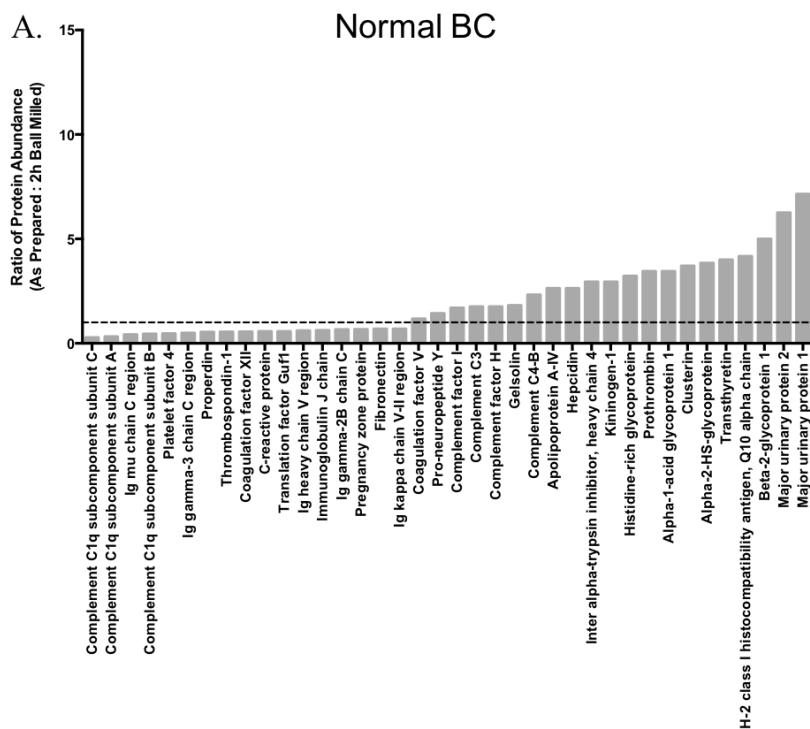
Figure 3.3.10: Relative abundance of proteins found to associate with 2h ball milled SWCNTs compared to As Prepared SWCNTs in normal serum.
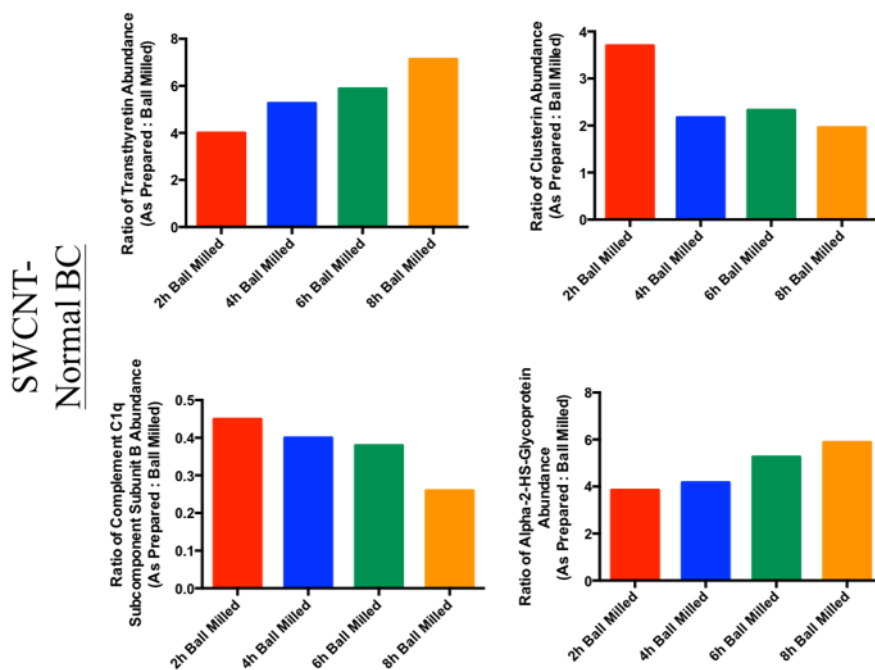
Figure 3.3.11: Differences in relative abundance of specific proteins (Transthyretin, Clusterin, Complement C1q Subcomponent Subunit B, and Alpha-2-HS-Glycoprotein) found to associate with SWCNTs in either normal serum due to ball milling time. All ratios are As Prepared SWCNTs : Ball Milled SWCNTs.

Many common individual protein components were identified in the biocoronas therefore, we next quantitatively evaluated whether ball milling influences their abundance in the SWCNT biocorona. Differences in abundance were evaluated for proteins found in common between As Prepared and ball milled SWCNTs following incubation in normal serum. Representative data comparing the abundance of commonly associated proteins between As Prepared and 2h ball milled SWCNTs following incubation in normal serum is shown in **Fig. 3.3.10**. Ball milling resulted in the decreased

abundance of many of these common proteins (higher ratios of As Prepared : 2h ball milled). The abundance of many proteins associated with the complement system was altered in the biocorona that formed on 2h ball milled SWCNTs compared to As Prepared SWCNTs in normal serum suggesting modified interactions with the complement system. The complement system is a part of the innate immune system and is involved in the removal of foreign objects as well as the inflammatory response.[100] These alterations in the interactions with the complement system due to ball milling may result in modified activation of the immune system thereby altering the SWCNT inflammatory response and clearance. These findings imply that ball milled SWCNTs are less likely to interfere with the adaptive immune response and less likely to trigger an immune response. Although many proteins were determined to commonly associate with SWCNTs, ball milling influenced their abundance within the biocorona and may ultimately influence cellular responses.

Progressive alterations in individual protein abundance due to ball milling time were also analyzed (**Fig. 3.3.11**). For example, as ball milling time increased, the amount of transthyretin was found to decrease on the surface of SWCNTs following incubation in normal serum. Transthyretin is produced by the liver and is a carrier of the thyroid-derived hormone thyroxine which is responsible for metabolism regulation.[101] Our data suggest that As Prepared SWCNTs may result in increased disruption of the endocrine system by binding transthyretin and interfering with the transport of thyroxine as compared to Ball Milled SWCNTs. In addition, increased ball milling time led to the increased association of clusterin (molecular chaperone protein and lipid transport) [32] and

complement C1q subcomponent subunit B (complement cascade) following incubation in normal serum. Increased ball milling time corresponded to decreased association of alpha-2-HS-glycoprotein abundance following incubation in normal serum. Since alpha-2-HS-glycoprotein is a large and abundant protein in serum it is likely that as its association decreases in the biocorona it is being replaced by smaller and lesser abundant proteins. This enrichment of lesser abundant proteins may alter the cellular interactions of the biocorona.   Ultimately, these representative changes in commonly associated individual protein abundance demonstrate differences in the biocorona of the SWCNT that are dependent on the process of ball milling. These abundance changes and alterations in protein identities support differential biological interactions due to ball milling and the likelihood of variable cellular and physiological responses.

Proteins found to associate with As Prepared and Ball Milled SWCNTs incubated in either normal serum were evaluated for biological pathways and common protein characteristics via gene ontology. This assessment of the data was performed to examine specific pathways and protein characteristics which may be potentially altered due to ball milling of SWCNTs. As Prepared SWCNTs incubated in normal serum interacted with biological pathways including blood coagulation, plasminogen activating cascade, Huntington's disease, integrin signaling pathway and others.   Following ball milling SWCNTs incubated in normal serum associated unique proteins which were related to blood coagulation, plasminogen activating cascade, inflammation mediated by chemokine and cytokine signaling and others. Overall the unique proteins which associated with SWCNTs following ball milling only added more proteins to pathways

already identified in the As Prepared sample. This suggests that ball milling increases the interactions with pathways SWCNTs already may perturb prior to ball milling. Ball milling resulted in the increased association of proteins related to the biological pathways of blood coagulation, integrin signaling, plasminogen activating cascade. The process of ball milling also resulted in interactions with proteins related to unique pathways compared to the As Prepared sample.

To examine commonalities between proteins that associate with the surface of SWCNTs and the role of ball milling, gene ontology was again utilized to assess protein classes. In normal serum, As Prepared SWCNTs associated protein classes involved in enzyme modulation, transfer/carrier, hydrolase, defense/immunity, signaling, receptor and others. Following ball milling and incubation in normal serum SWCNTs associated an increased number of distinct proteins related to enzyme modulation, transfer/carrier, defense/immunity, signaling, and hydrolase. Following ball milling SWCNTs also began to interact with proteins classified as structural. Following the process of ball milling, additional numbers of unique proteins from classes of enzyme modulation, transfer/carrier, defense/immunity, signaling, and cytoskeletal were found to associate. These findings demonstrate that following ball milling SWCNTs incubated in normal serum interact with the same classes of proteins as the As Prepared SWCNTs. The unique proteins found to interact with SWCNTs following ball milling (**Fig. 3.3.10**) consist of additional proteins from these classes. Ball milling, however, appears to increase interactions with structural proteins.

3.4 Conclusions

Defects in nanomaterials can play an important role in determining biomolecular interactions with serum proteins. SWCNTs with different defect densities were prepared by the ball milling process to study the influence of defects on biocorona formation. Our study demonstrates that charged defects induced by the ball milling process result in the formation of distinctive biocoronas through the differential association of proteins. Specifically, proteins that function through charge transfer and redox mechanisms were observed to bind defected SWCNTs.

Also, we demonstrated that carboxylated MWCNTs displayed no observable toxicity to bone marrow-derived macrophages. Rather, an increase in MWCNT defect density promoted protein binding leading to successful delivery of ovalbumin into macrophages and promoted $CD4^+$ T cell proliferation. Taken together, these data suggest that in addition to surface modification such as carboxylation, surface defect density should be considered in the design of novel carbon nanotube platforms for vaccine delivery.

CHAPTER FOUR

DISEASE INDUCED DISPARITIES IN CORONA FORMATION

4.1 Introduction

Many of the nanotherapeutics being developed utilize intravenous delivery thereby leading to direct vascular exposure of nanoparticles. However, it is becoming recognized that exposure to NPs in animal models induces a variety of vascular effects including exacerbation of atherosclerotic plaque formation, vascular inflammation, oxidative stress, and modified vascular reactivity [102]–[106]. In general, cardiovascular toxicity is of concern regarding the development of NPs and other pharmaceuticals as it is often difficult to identify in early toxicity screens and represents a major cause of new drugs failing phase II and III clinical studies. The improvement and development of *in vitro* approach to screen NPs for cardiovascular toxicity prior to *in vivo* testing is therefore needed. A key to this improvement is the necessity that these *in vitro* approaches accurately depict the *in vivo* environment.

A large and growing portion of the population currently exists with an underlying disease state. These underlying disease states, such as cardiopulmonary diseases, can

modify how individuals respond to exposures resulting in exacerbated responses[107]–[109]. Hyperlipidemia is a significant underlying disease state that is common in a significant portion of the U.S. population. Despite many common underlying disease states, such as hyperlipidemia within the population, the majority of studies assessing NP-induced toxicity are performed in healthy animal models and utilize *in vitro* models representing healthy physiological conditions. These healthy scenarios often do not represent the population in which nano-based therapeutics and diagnostic tools will be utilized. Many diseases such as hyperlipidemia result in altered expression of circulating macromolecules such as proteins, peptides, and lipids[110], [111]. Once NPs are introduced into a physiological environment they are rapidly coated with macromolecules forming a biocorona (BC)[82], [112]. The addition of the BC alters the interactive interface of the NP and can thereby result in modified NP clearance, distribution, activity, and toxicity[113]–[115], [17]. Variations in the BC resulting from using dissimilar *in vitro* methods and the use of conditions that do not account for diseased physiological environments that modify serum content may explain many inconsistencies between *in vitro* toxicity screening and *in vivo* studies of NP safety[116] (Joris 2013). Therefore, the formation of the BC is governed by the physicochemical properties of the NP, as well as, the physiological environment [117], [9], [76], [118]–[120]. To date, the examination of the toxicological impact of the BC has been performed only assessing the physicochemical properties of the NP while ignoring the role of the physiological environment and disease related changes in the biological milieu.

Magnetite, iron oxide (Fe_3O_4) NPs, are of considerable interest for their

biomedical applications, particularly for their use as MRI contrast agents due to their superparamagnetic properties[121]. Furthermore, their surfaces are easily modified to allow for targeting of particular tissues, specifically for tumor targeting [122]. Due to their emerging use in the biomedical field, evaluation of their toxicity is needed particularly in individuals with underlying disease states that may influence the formation of the BC. Additionally, the BC has been shown to influence the function of Fe_3O_4 NPs by interfering with their contrast abilities when used for MRI [123]. It is unclear how differential BC formation on the surface of Fe_3O_4 NPs due to disease-induced alterations in serum content may affect functionality and toxicity.

In our current study, we evaluated the formation of the BC on Fe_3O_4 NPs using normal/healthy and lipid-rich rat serum. This evaluation assessed changes in NP physicochemical properties due to additions of the BCs as well as utilized a proteomic approach to identify differences in the protein content of the BCs. Lastly, we assessed the toxicological implications of these BCs on Fe_3O_4 NPs including cellular uptake, cytotoxicity, and cell activation. This toxicological assessment was performed in rat aortic endothelial cells (RAEC) and exposures occurred under flow conditions to more accurately depict the *in vivo* environment. Overall, this study strives to promote our understanding of nanotoxicity, as well as, the development of safe nano-therapeutics utilizing relevant exposure conditions, which more accurately portrays the *in vivo* environment.

In addition to the defects in SWCNT structure as shown in Chapter three, physiological environment also has a significant impact on the formation of the BC and

can alter SWCNT-biomolecular interactions and subsequent cellular responses. Individuals that suffer from underlying diseases which modify serum biomolecule content will likely form unique BCs compared to healthy individuals. Introduction of NPs into these individuals with high cholesterol may result in altered BC formation that impacts NP-cellular interactions and responses. This BC that formed in high cholesterol serum exacerbated the inflammatory response of endothelial cells following exposure compared to normal serum BCs. This finding demonstrates how disease-induced alterations in the physiological environment can impact NP biological response by altering the BC.

4.2 Materials and methods

4.2.1 Isolation of Normal and Hyperlipidemic Rat Serum

Serum samples were kindly provided by Dr. Urmila Kodavanti at the US Environmental Protection Agency. Briefly, healthy male Sprague Dawley rats (Charles River Laboratories Inc, Raleigh NC) received water ad libitum and were fed either a normal diet of standard (5001) Purina rat chow (Brentwood, MO) or a diet high in fructose (60%) (TD89247, Harlan Laboratories, Madison, WI). All rats were maintained in an isolated animal room in an Association for Assessment and Accreditation of Laboratory Care (AALAC) approved animal facility 21 ± 1° C, 50 ± 5% relative humidity, and 12 h light/dark cycle. Following 2 weeks on the diets animals were necropsied and blood was collected without anticoagulant present via abdominal aortic

puncture. Following processing of serum, samples were pooled and aliquoted to be stored at -80°C. Serum from rats fed a normal diet (normal serum) demonstrated a cholesterol content of 122.27 mg/dl whereas serum from rats fed a high fructose diet (lipid serum) demonstrated a cholesterol content of 253.11 mg/dl. The U.S. EPA NHEERL Institutional Animal Care and Use Committee (IACUC) approved the protocol. The animals were treated humanely and with regard for alleviation of suffering.

4.2.2 Formation and characterization of Fe_3O_4 Nanoparticle-Biocorona

Spherical 20 nm Fe_3O_4 NPs suspended in PVP at a concentration of 20 mg/ml were purchased from Nanocomposix (San Diego, CA). BCs were formed on Fe_3O_4 NPs as described in our recent publications [76], [124], [99], [125]. Fe_3O_4 NPs were diluted in water to a concentration of 1 mg/ml incubated for 8 h at 10° C in distilled (DI) water (control), 10% normal serum, or 10% lipid-rich serum. Specifically, 250 ul of Fe_3O_4 NP (1 mg/ml), 650 μl of water, and 100 μl of serum were combined in a 1.5 ml tube. Following incubation Fe_3O_4 NPs were then pelleted via centrifugation 14,000 rpm (20,817 x g) 10 min and washed with PBS. Following centrifugation, the supernatant was removed and Fe_3O_4 NP was resuspended with 250 μl of water to its initial concentration of 1 mg/ml. The BC formed following incubation of Fe_3O_4 NPs in normal serum is referred to as Fe_3O_4 NP – Normal BC whereas the BC form following incubation in lipid-rich serum is referred to as Fe_3O_4 NP – Lipid BC.

For characterization, we measured the hydrodynamic size and zeta potentials

(ZetaSizer Nano, Malvern) of uncoated Fe_3O_4 NPs, and Fe_3O_4 NPs with BCs in DI water with Fe_3O_4 NPs at a concentration of 50 µg/ml (n=3/particle). Cholesterol content of the BCs formed on the surface of Fe_3O_4 NPs was evaluated via a commercially available colorimetric total cholesterol assay kit (Cell Biolabs, San Diego, CA) following manufacturer's instructions. Briefly, 50 µl of Fe_3O_4 NPs without or with BCs were loaded into a 96 well plate in duplicate and then were treated with a cholesterol reaction reagent that includes cholesterol esterase, cholesterol oxidase, and a colorimetric probe. The cholesterol esterase causes the hydrolysis of cholesterol esters from the cholesterol bound to the Fe_3O_4 NPs allowing for their determination.

Transmission electron microscopy images were obtained using a Hitachi H7600 microscope. For TEM studies, Fe_3O_4 NP – Normal BC and Fe_3O_4 NP – Lipid BC samples were stained by incubating them in 0.1% OsO_4 solution for 30 min. The samples were washed with double distilled water to remove unbound OsO_4 after which the samples were drop casted on a 400 mesh Cu grid and dried overnight. Z-contrast images were also acquired using Hitachi HD2000 microscope without staining the samples. The high Z-contrast between Fe_3O_4 NPs and BC allowed us to distinguish the two phases (i.e., NPs and BC).

Utilizing a proteomics approach, individual protein components of the BCs were identified similar to our previous studies evaluating the BC. Briefly, following the addition of the BCs, Fe_3O_4 NPs were washed and pelleted three times with PBS (10 min 14,000 rpm / 20,817 x g). Proteins were then solubilized using 8 M urea and 10 mM dithiothreitol (DTT) for 45 min at 60 °C. Fe_3O_4 NPs were then pelleted via

centrifugation at 15,000 x g for 10 min and the supernatant containing solubilized proteins was collected. Protein samples were then treated with 30 mM iodoacetamide for 30 min in the dark at room temp followed by the addition of 10 mM DTT in 50 mM ammonium bicarbonate (ABC) for 30 min at room temperature. Finally, 50 mM ABC was used to dilute remaining urea to less than 1 M. Samples were then proteolyzed using porcine trypsin (0.1 µg/ml) overnight at 37 °C, heated to 90 °C to deactivate trypsin, and concentrated to dryness. Samples were then resuspended in 0.1% trifluoroacetic acid in water, purified via Ziptip Pipette Tips (Millipore, Billerica, MA), and concentrated to dryness. Samples were then resuspended in 0.1 % Formic Acid in DDI water and injected into a Bruker Impact HD Q-TOF mass spectrometer (Bruker Daltonic, Billerica, MA). The acquired data were searched using a MASCOT (ver. 2.4.1) search engine with a peptide cutoff of 10 ppm and a minimum peptide score of 20 and a protein score of 40. The false discovery rate for samples was < 1% and the significance threshold was $p <$ 0.05. To determine differences in common protein components of the BCs, ratios of individual proteins were assessed utilizing Proteinscape and Profileanalysis software packages (Bruker Daltonic, Billerica, MA). Four samples of each BC were analyzed individually and injected 4 separate times. Peptides to be considered for evaluation had to be found within 5 of 8 samples with a minimum of 2 per BC type. Only peptides determined to be statistically significant were utilized to calculate ratios and more than one peptide had to be identified for a protein for that individual protein to be quantified.

4.2.3 Cellular uptake and cytotoxicity

    Rat aortic endothelial cells (RAEC) were cultured in rat endothelial cell growth

media (Cell Applications Inc., San Diego, CA). Cell lines were maintained in flasks under standard conditions at 37°C and 5% CO_2. For the assessment of the BC and its role in cellular responses, all experiments were performed utilizing serum-free media as done in our previous experiments [99], [125]. The removal of serum from media allows for the evaluation of the intentionally formed BC without the addition of a secondary BC within the cell culture system. The use of serum-free media limits the study of the BCs and the cellular responses to acute time points.

To assess Fe_3O_4 NP Cytotoxicity RAEC cells were grown to 90% confluency in 96 well plates (Costar) and were exposed to increasing concentrations of Fe_3O_4 NPs (0, 2.5, 5, 10, 20, 40, 80 μg/ml) with or without BCs for 2 h and 6 h in serum-free media in a static system. Cells were exposed in this static system due to the high number of concentrations evaluated and to screen for overt cytotoxicity. Due to the use of serum-free media, later time points were not evaluated. The concentrations of Fe_3O_4 NPs utilized were selected based on possible human exposures as well as previous *in vitro* examination of Fe_3O_4 NPs and other NPs. Briefly, concentrations of Fe_3O_4 NPs were determined based on levels used for human MRI analysis utilizing Fe_3O_4 NPs as a contrast agent, which typically range from 5-10 μg/ml blood volume, considering a male of 90 kg [126], [127]. Changes in cell viability were assessed via the 3-(4,5-dimethylthiazol-2-yl)-5-(3-carboxmethoxyphenyl)-2-(4-sulfophenyl)-2H-tetrazolium (MTS) assay (Promega, Madison, WI) via manufacturer's instructions using a spectrophotometer (BioTek Synergy HT, BioTek, Winooski, VT). No overt cytotoxicity was identified therefore a concentration of 20 μg/ml was utilized for all subsequent

experimentation of RAEC uptake and activation. This concentration of 20 μg/ml was also selected due to it being within the range of a human-relevant concentration.

In order to more accurately depict the *in vivo* environment, RAEC uptake of Fe_3O_4 NPs was assessed utilizing a Quasi Vivo system (Kirkstall, Rotherham, UK) that pumps media over the surface of the cells. RAECs were grown on coverslips and placed into an individual chamber. Serum-free media (control), serum-free media containing Fe_3O_4 NPs – Normal BC, or serum-free media contain Fe_3O_4 NPs – Lipid BC at a concentration of 20 μg/ml was loaded into the reservoir. A flow rate of 1 ml/min of fluid was utilized during the 2 h exposure. This NP concentration and time point were select for the evaluation of cellular uptake based on previous research examining the uptake of other NPs by RAECs and possible human blood concentrations of Fe_3O_4 NPs when utilized as an MRI contrast agent. The flow rate of 1 ml/min was estimated to result in a shear stress of 100×10^{-3} Pa. The Quasi Vivo system as manufactured can produce a shear stress of 2×10^{-5} Pa at a flow rate of 1 ml/min[128], however by inserting silicone glue into the base of the chamber thereby raising the cells nearer to the inlet of media a higher shear stress can be achieved. For comparison, a shear stress of 1.5-2.0 Pa occurs in human arteries while the higher diameter post-capillary venules have a shear stress at 300×10^{-3} Pa [129], [130]. A shear stress of 100×10^{-3} Pa is below the necessary 200×10^{-3} – 5 Pa need to induce cell alignment and tight junctions *in vitro* [131]. Therefore this shear stress utilized in this study will not induce biological responses by itself. Following exposure, coverslips were removed from the chamber and placed into a 24 well plate. Cells were then detached with 250 μl of trypsin and neutralized with an equal volume of

RAEC media. Cells were then washed 3 times with PBS and differences in uptake were determined by ICP-MS analysis of Fe content. All samples were dissolved in 6 ml of 2% HNO_3. The Fe concentration was determined with ICP-MS (X series II, Thermo Scientific) using an internal standard containing Li, Y and In with a detection limit of 3 ppb. Qualitative assessment of Fe_3O_4 NP uptake was performed by darkfield microscopy (Cytoviva, Auburn, AL). RAECs underwent the same exposure protocol, were fixed with 2% paraformaldehyde and had their nucleuses stained with DAPI. Focusing on the nucleus allowed for the assessment of internalized Fe_3O_4 NPs.

RAEC activation by Fe_3O_4 NPs without or with BCs was assessed utilizing a Quasi Vivo system (Kirkstall, Rotherham, UK) at a flow rate of 1 ml/min of fluid. RAECs were grown on coverslips and placed into an individual chamber. Serum-free media (control), serum-free media containing Fe_3O_4 NPs – Normal BC, or serum-free media contain Fe_3O_4 NPs – Lipid BC at a concentration of 20 μg/ml was loaded into the reservoir and cells were exposed for 1 h. Total RNA was isolated from cells using Direct-zol RNA MiniPrep (Zymo Research Corp., Irvine, CA) via manufacturer's instructions and quantified via nanodrop (Nanodrop 2000c Spectrophotometer, Thermo Scientific). Total RNA was reverse transcribed to cDNA using an iScript cDNA Synthesis Kit (Bio-Rad Laboratories, Hercules, CA). A rat endothelial cell biology PCR array was utilized to identify markers of endothelial activation following exposure to Fe_3O_4 NPs without or with BCs (RT2 Profiler PCR Array Systems, Cat# PARN-015Z, SABiosciences; Frederick MD). This PCR array identified 84 genes related to angiogenesis, vasoconstriction/dilation, inflammatory response, apoptosis, cell adhesion,

coagulation and platelet activation. Plates were prepared according to manufacturer's instructions and using a StepOnePlue Real-Time PCR System (ABI, Foster City, CA). Data analysis on SaBiosciences web-based PCR array expression analysis suite utilized the $\Delta\Delta Ct$ method with normalization to β-actin (housekeeping gene) and considering serum-free media exposed cells as controls.

All data are presented as mean $\pm$ SEM consist of 3-6 experiments. Data were analyzed by one-way ANOVA, with differences between groups assessed by Tukey's post hoc tests. All graphs and analysis were performed using GraphPad Prism 6 software (GraphPad, San Diego, CA, USA). Statistical significance was determined when p was found to be less than or equal to 0.05 between groups.

4.2.4 Formation and evaluation of the SWCNT-Biocoronas

BCs were formed on SWCNTs (n=6/group) using a modified Tenzer's method, as described in our recent publications.[76], [118], [132] Individual SWCNTs were suspended water at a concentration of 1mg/ml and incubated in either 10% normal or 10% hyperlipidemic serum to be mixed constantly for 8 h at 4°C. Specifically, SWCNTs following suspension were sonicated for 5 min in an inverted cup-horn sonicator at an amplitude of 75. 250 ul of SWCNTs (1mg/ml), 650 ul of water, and 100 ul of serum were combined in a 1.5 ml tube. Following the 8 h incubation SWCNTs were pelleted via centrifugation 14,000 rpm (20,817 x g) 10 min and washed with PBS. This washing process was repeated three times. Following the final centrifugation, the supernatant was removed and SWCNTs were resuspended with 250 ul of water to their initial

concentration of 1 mg/ml. The BC formed following incubation of SWCNTs in normal

serum is referred to as SWCNT-Normal BC whereas the BC formed the following

incubation in hyperlipidemic serum is referred to as SWCNT-Lipid BC.

We used proteomics approach to individual protein components of the BCs

similar to our previous studies evaluating the BC.[28] Briefly, following the addition of

the BCs, SWCNTs were washed and pelleted three times with PBS (10 min 14,000 rpm /

20,817 x g). Proteins were then solubilized using 8 M urea and 10 mM dithiothreitol

(DTT) for 45 min at 60 °C. SWCNTs were then pelleted via centrifugation at 15,000 x g

for 10 min and the supernatant containing solubilized proteins was collected. Protein

samples were then treated with 30 mM iodoacetamide for 30 min in the dark at room

temp followed by the addition of 10 mM DTT in 50 mM ammonium bicarbonate (ABC)

for 30 min at room temperature. Finally, 50 mM ABC was used to dilute remaining urea

to less than 1 M. Samples were then proteolyzed using porcine trypsin (0.2 ng/μl)

overnight at 37 °C, heated to 90 °C to deactivate trypsin, and concentrated to dryness.

Samples were then resuspended in 0.1% trifluoroacetic acid in water, purified via Ziptip

Pipette Tips (Millipore, Billerica, MA), and concentrated to dryness. Samples were then

resuspended in 0.1 % Formic Acid in HPLC-grade water and injected onto a nHPLC

utilizing a flow rate of 800 nL/min with a gradient of 5-50% 0.1% formic acid in

acetonitrile (ACN) over 30 min on C18 trapping (20x0.1 mm^2) and analytical columns

(150x0.1 mm^2). The nLC was coupled to a nano-ESI source and Impact HD Q-TOF

mass spectrometer (Bruker Daltonics, Inc., Billerica, MA). The acquired data were

searched using a MASCOT (ver. 2.4.1) search engine with a peptide cutoff of 10 ppm

and a minimum peptide score of 20 and a protein score of 40. The false discovery rate for samples was < 1% and the significance threshold was $p < 0.05$. These identified proteins were then assessed for biological pathways SWCNTs may interfere with and common protein characteristics by via the Gene Ontology Consortium database (geneontology.org,) and using only mapped identifiers. To determine differences in common protein components of the BCs, ratios of individual proteins were assessed utilizing ProteinScape and ProfileAnalysis software packages (Bruker Daltonic, Billerica, MA). Four samples of each BC were analyzed individually and injected 4 separate times. Peptides to be considered for evaluation had to be found within 5 of 8 samples with a minimum of 2 per BC type. Only peptides determined to be statistically significant were utilized to calculate ratios and more than one peptide had to be identified for a protein for that individual protein to be quantified. Data generated allowed for comparisons of the BCs between SWCNTs that had undergone ball milling resulting in altered defect loads and comparisons between the BCs that formed under the differing physiological conditions (normal vs hyperlipidemic).

4.3 Results and discussion

4.3.1 Case of Fe_3O_4

Nanoparticle	Hydrodynamic Size (nm)	Zeta Potential (mV)	Cholesterol Content (µM)
Fe_3O_4	103.0 ± 2.3	-34.1 ± 0.6	------------
Fe_3O_4 – Normal BC	117.3 ± 5.5	-24.1 ± 0.4 *	7.2 ± 0.3
Fe_3O_4 – Lipid BC	107.4 ± 5.5	-23.0 ± 1.4 *	62.2 ± 13.1[#]

Table 4.3.1: Fe_3O_4 NP-Biocorona Characterization (n=3). * denotes statistical difference from Fe_3O_4 without BC ($p \leq 0.05$). [#] denotes statistical difference from Fe_3O_4 – Normal BC ($p \leq 0.05$).
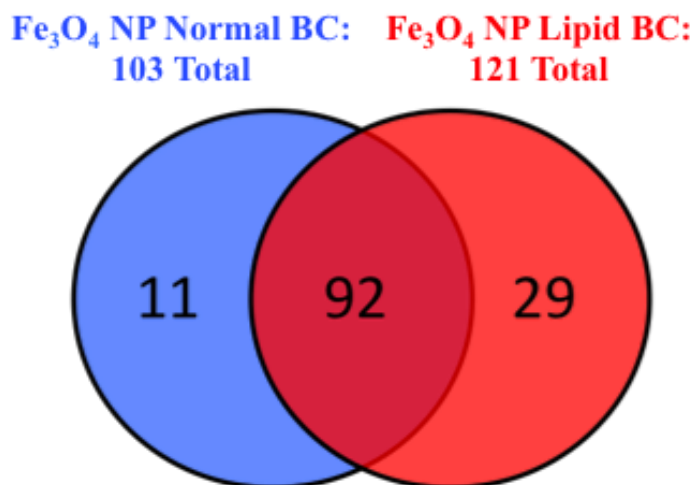
Figure 4.3.1: Venn diagram representing the distribution of protein components found to associate with 20 nm Fe_3O_4 NPs following incubation in 10% normal (blue) or hyperlipidemic (red) serum.

Following incubation of Fe_3O_4 NPs in 10% normal or lipid-rich serum and formation of the biocoronas (BC), hydrodynamic size and zeta potential were assessed (**Table 4.3.1**). Formation of either BC slightly increased the hydrodynamic size of the Fe_3O_4 NPs (**Table 4.3.1**). However, the formation of both the normal BC and lipid BC on Fe_3O_4 NP resulted in a significant decrease in zeta potential (**Table 4.3.1**).

Variations in the cholesterol content and protein components of the BCs formed on Fe_3O_4 NPs in the differing physiological environments were evaluated. Assessment of the cholesterol content of each BC demonstrated cholesterol as a component of both BC. As expected, the lipid BC had a greater amount of cholesterol associated with it compared to the normal BC (**Table 4.3.1**). Label-free proteomics was utilized to evaluate differences in protein components of the BCs. The BCs on Fe_3O_4 NPs incubated in either normal or lipid-rich serum were found to consist of 103 or 121 individual proteins respectively (**Fig. 4.3.1**). In common between the two BCs were 92 proteins including complement C3, prothrombin, serum albumin, serotransferrin, alpha-2-HS glycoprotein, apolipoprotein A-II, apolipoprotein E, and apolipoprotein C-I (**Fig. 4.3.1**). Fe_3O_4 NP with a normal serum BC was determined to bind 11 unique proteins when compared to Fe_3O_4 NP with a lipid-rich BC. Fe_3O_4 NP with a lipid-rich BC was found to bind 29 unique proteins when compared to Fe_3O_4 NP with a normal BC. A complete list of all proteins found to associate with Fe_3O_4 NP following incubation in the different physiological environments can be found in ref [28].
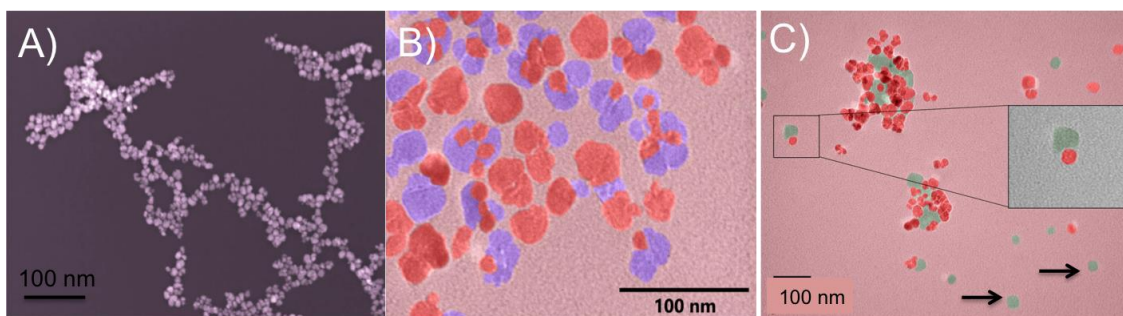
Figure 4.3.2. False-colored transmission electron micrographs for (a) Fe$_3$O$_4$ NPs, (b) Fe$_3$O$_4$-Normal BC, and (c) Fe$_3$O$_4$-Lipid BC. Biocorona is shown in blue (b) and green colors (c). The Fe$_3$O$_4$ NPs were observed to be embedded in BC. The black arrows in (c) show liposome structures formed in Fe$_3$O$_4$-Lipid BC.

As shown in **Fig. 4.3.2**, bare Fe$_3$O$_4$ NPs were found to have a mean size of ~30 nm. This is significantly smaller than the hydrodynamic size (>100 nm) suggesting that there may be some agglomeration of Fe$_3$O$_4$ NPs in solution. Additionally, TEM images showed that the Fe$_3$O$_4$ NPs are not completely spherical. We found that both Fe$_3$O$_4$-Normal BC and Fe$_3$O$_4$- Lipid BC contained Fe$_3$O$_4$ NPs embedded BC (**Fig. 4.3.2 B** and **C**). Interestingly, we also found the presence some liposomes in Fe$_3$O$_4$-Lipid BC, which were confirmed by OsO$_4$ staining and Z-contrast studies.

To determine possible differences in cytotoxicity due to the addition of the BCs, rat aortic endothelial cells (RAECs) were exposed to Fe$_3$O$_4$ NPs without or with BCs at concentrations of 2.5, 5, 10, 20, 40, or 80 µg/ml for 2 h or 6 h and examined for differences in viability. This initial assessment of cytotoxicity was performed in a static

cell culture system due to the number of concentrations examined. Due to the removal of serum from the cell culture media, only acute time points were evaluated. None of the concentrations utilized were found to induce significant cytotoxicity. Furthermore, the addition of the BCs was not found to alter cytotoxicity. Based on these data, previous work evaluating NP toxicity in RAEC, and relevant human concentrations a concentration of 20 μg/ml was utilized for all experimentation investigating disease-induced BC toxicity [126], [127]
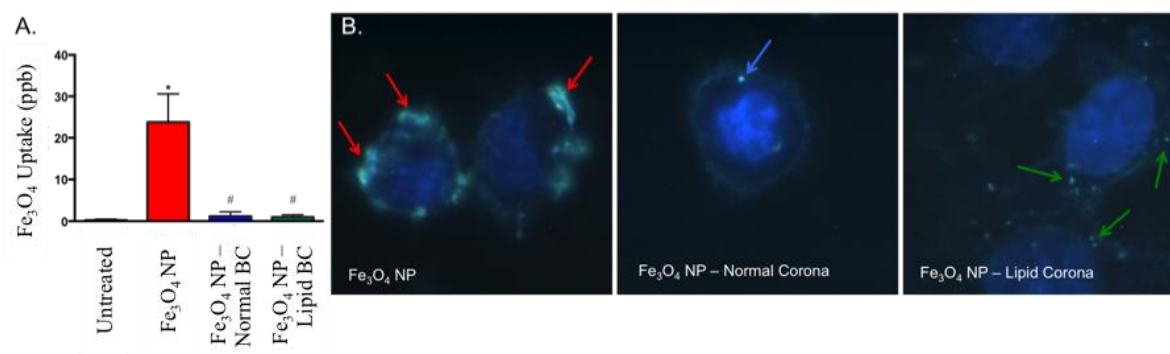
Figure 4.3.3: Measurement of 20 nm Fe_3O_4 NP uptake by ICP-MS and darkfield microscopy. Rat aortic endothelial cells (RAEC) were exposed to serum-free media (control), Fe_3O_4 NPs without a biocorona (BC), or Fe_3O_4 NPs with either a normal serum or lipid serum BC. Cells were exposed to a concentration of 20 μg/ml for 2 h under flow conditions of 1 ml/min. A) Following exposure, cells were assessed by ICP-MS for Fe_3O_4 NP uptake. Values are expressed as mean ± SEM (n=3/group). * Indicates significant difference from controls ($p < 0.05$). B) Alterations in RAEC uptake of Fe_3O_4 NPs due to the addition of BCs was qualitatively evaluated via darkfield microscopy. Fe_3O_4 NPs without a BC are identified with red arrows, Fe_3O_4 NP-normal BC with blue

arrows, and Fe_3O_4 NP-lipid BC with green arrows.

BC-induced alterations in RAEC uptake were evaluated by ICP-MS and darkfield microscopy (Figure 4). RAECs were exposed to 20 μg/ml of Fe_3O_4 NPs without or with BCs for 2 h under a flow rate of 1 ml/min. RAECs were found to readily internalize Fe_3O_4 NPs without a BC, however, addition of both BCs resulted in reduced uptake as evaluated by ICP-MS (**Fig. 4.3.3A**). These results were qualitatively confirmed via darkfield microscopy (**Fig. 4.3.3B**). Fe_3O_4 NPs without a BC were internalized (red arrows) to a greater degree than Fe_3O_4 NPs with a normal BC (blue arrows) or Fe_3O_4 NPs with a lipid BC (green arrows).

To determine differences in Fe_3O_4 NP-induced RAEC activation due to the addition of the BCs, mRNA gene expression was examined. RAECs were exposed for 1 h to 20 μg/ml of Fe_3O_4 NPs without or with BCs under a flow rate of 1 ml/min. A PCR array specific for rat endothelial cell biology was utilized which evaluated mRNA expression changes in 85 genes related to a variety of processes. These processes included angiogenesis, vasoconstriction/dilation, inflammatory response, apoptosis, cell adhesion, coagulation and platelet activation. In summary, RAECs exposed to Fe_3O_4 NPs without a BC demonstrated a significant ($p \leq 0.05$) upregulation of 4 genes and downregulation of 10, while cells exposed to Fe_3O_4 NPs with a normal BC had 7 genes upregulated and 18 down-regulated and those exposed to Fe_3O_4 NPs with a lipid BC had 10 genes upregulated and 8 down-regulated. Exposure to all Fe_3O_4 NPs (without and with BCs) significantly altered the expression of a subset of genes in common including the upregulation of Cx3cl1, Cxcl1, Selp, and VCAM1 and the downregulation of Ednra,

Hif1a, and Sod1. Inflammatory genes such as IL-6, Cxcl1, Cxcl2, and TNF were induced to a greater degree upon RAEC exposure to Fe_3O_4 NPs with BCs compared to the absence of a BC. The induction of these inflammatory genes was greatest in RAECs exposed to Fe_3O_4 NPs with a lipid BC. Verification of VCAM-1 mRNA expression seen in the PCR array through real-time PCR demonstrated similar gene induction. Additional controls were added to this experiment to ensure that changes seen in mRNA expression were not related to carry over of free serum proteins (proteins not associated with Fe_3O_4 NP BCs). These control groups demonstrated no changes in VCAM-1 mRNA expression. To further assess activation of RAEC by Fe_3O_4 NPs without or with BCs, cell surface expression of VCAM-1 was evaluated by immunofluorescence (**Fig. 4.3.4**). Cells again were exposed under flow conditions of 1 ml/min to Fe_3O_4 NPs without or with BCs (20 μg/ml) for 1 h and stained for VCAM-1 expression. Fe_3O_4 NPs without a BC and Fe_3O_4 NPs with a normal BC did not demonstrate differences in VCAM-1 expression compared to controls (**Fig.4.3.4**). Exposure to Fe_3O_4 NPs with a lipid BC, however, did demonstrate increased cell surface expression of VCAM-1. This alteration in surface VCAM-1 expression verified results examining mRNA expression.
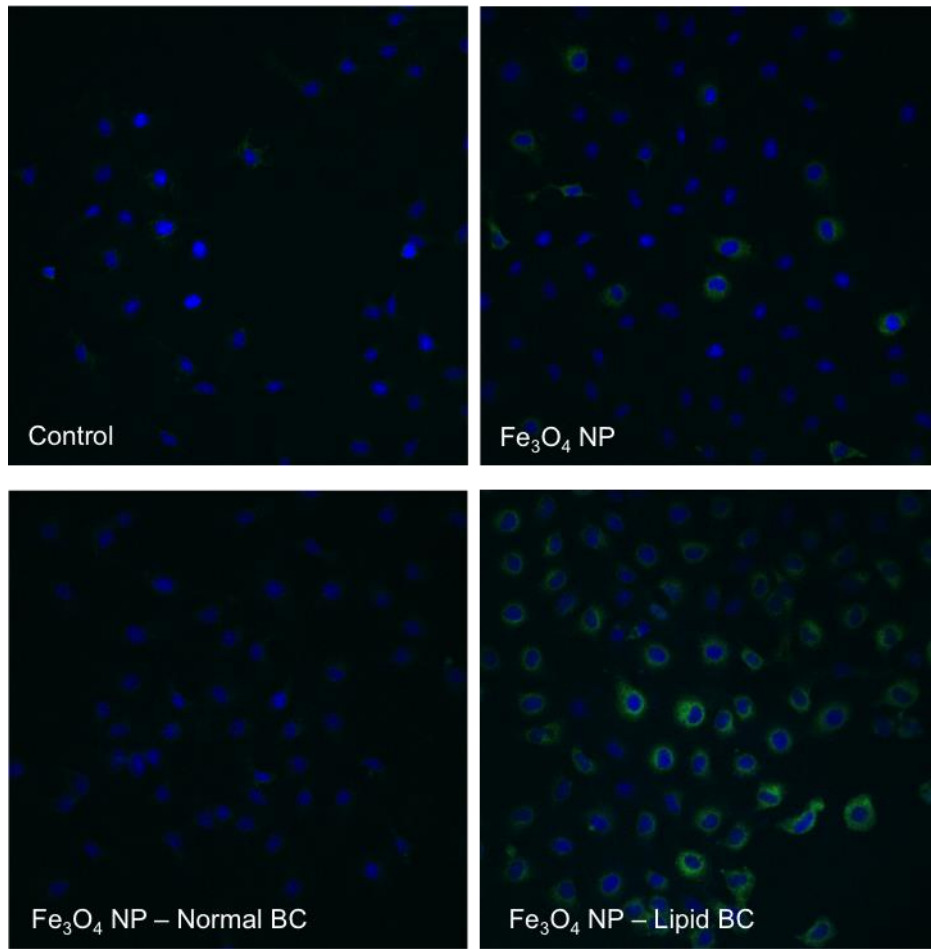
Figure 4.3.4: Assessment of Fe_3O_4 NP-BC alterations in cell surface expression of VCAM-1 by immunofluorescent staining. Rat aortic endothelial cells (RAEC) were exposed to serum-free media (control), Fe_3O_4 NPs without a BC or Fe_3O_4 NPs with either a normal serum or lipid serum BC. Cells were exposed to a concentration of 20 µg/ml for 1 h under flow conditions of 1 ml/min. Cells were then immunofluorescently stained with DAPI to identify the nucleus (Blue) and with a VCAM-1 antibody to identify endothelial cell surface expression of VCAM-1 (Green).

<u>4.3.2 Case of SWCNTs</u>

A substantial portion of our population exists with an underlying health condition. These underlying conditions often modify the biomolecular content of the individual's serum. Since the formation of the biocorona is dependent on both the physicochemical properties of the engineered nanomaterial as well as the physiological environment it likely that underlying disease states will result in unique biocorona formation.[21] One highly prevalent and growing disease state is hyperlipidemia or high cholesterol. Previous evaluation has demonstrated that incubation of iron oxide nanoparticles in hyperlipidemic serum results in the formation of unique biocoronas compared to incubation in normal serum.[21] Further, the addition of the hyperlipidemic biocorona was determined to induce greater inflammatory responses in endothelial cells suggesting increased toxicity of nanoparticles in individuals with hyperlipidemia. In our current study, we evaluated the biocorona that forms on SWCNTs that have been either untreated or ball milled in both normal and hyperlipidemic serum. In order to understand nanoparticle-biomolecular interaction, it is necessary to examine common disease states.
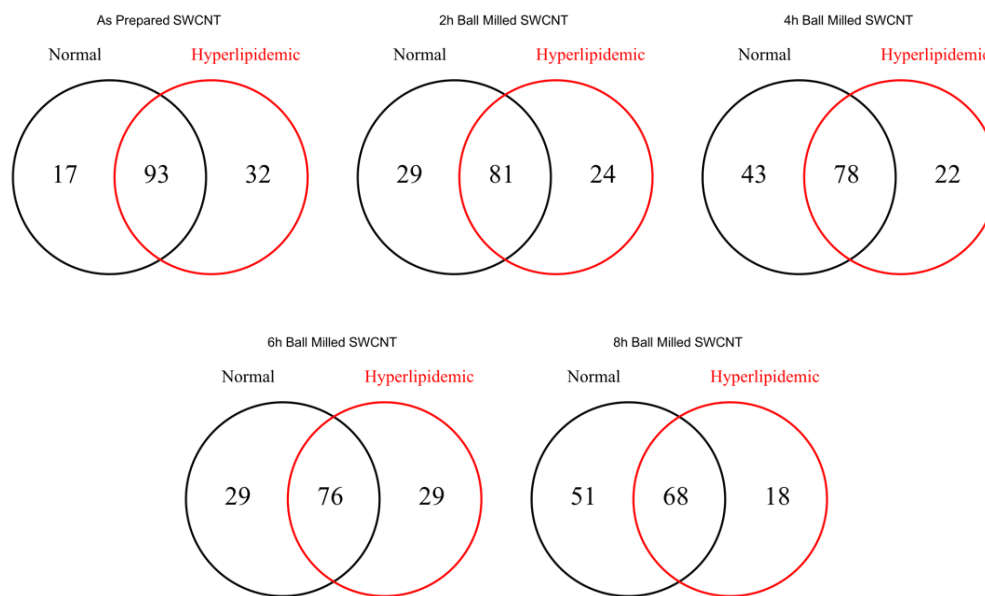
Figure 4.3.5: Venn diagrams representing the number of proteins found to associate with SWCNTs due to incubation in either normal or hyperlipidemic serum.

A proteomic comparison of the protein components of the biocorona that forms on SWCNTs following incubation in either normal or hyperlipidemic serum demonstrated that the majority of proteins were in common (**Fig. 4.3.5**). These common proteins included apolipoprotein AI, C reactive protein, fibronectin, kininogen-1, plasminogen, and others. Unique to the normal serum biocorona were proteins alpha-1 antitrypsin 1-4, hemoglobin subunit A, and others. Unique to the hyperlipidemic biocorona were hepcidin, extracellular matrix protein 1, antithrombin-III, and others. Interestingly, as ball milling time was increased, fewer proteins were shared between the normal and hyperlipidemic serum biocoronas. This corresponded with a trend of more unique proteins in the normal serum biocorona compared to the hyperlipidemic serum

biocorona as ball milling time increased (**Fig. 4.3.5**). Further, the hyperlipidemic serum biocorona demonstrated less unique proteins compared to the normal serum biocorona as ball milling time increased. It is likely that due to the amount of cholesterol present in the hyperlipidemic serum that cholesterol outcompeted proteins for binding sites on the SWCNTs. This competition may explain the decreases in common proteins between the normal and hyperlipidemic biocoronas as increased ball milling time enhanced the surface area of SWCNTs resulting in more cholesterol association. To date, few studies have evaluated the lipid content of the biocorona that forms on engineered nanomaterials. Future research is needed regarding the association of lipids on engineered nanomaterials in physiological environments.[133] It is likely that they not only modify the association of other biomolecules but also nanomaterial-cellular interactions.
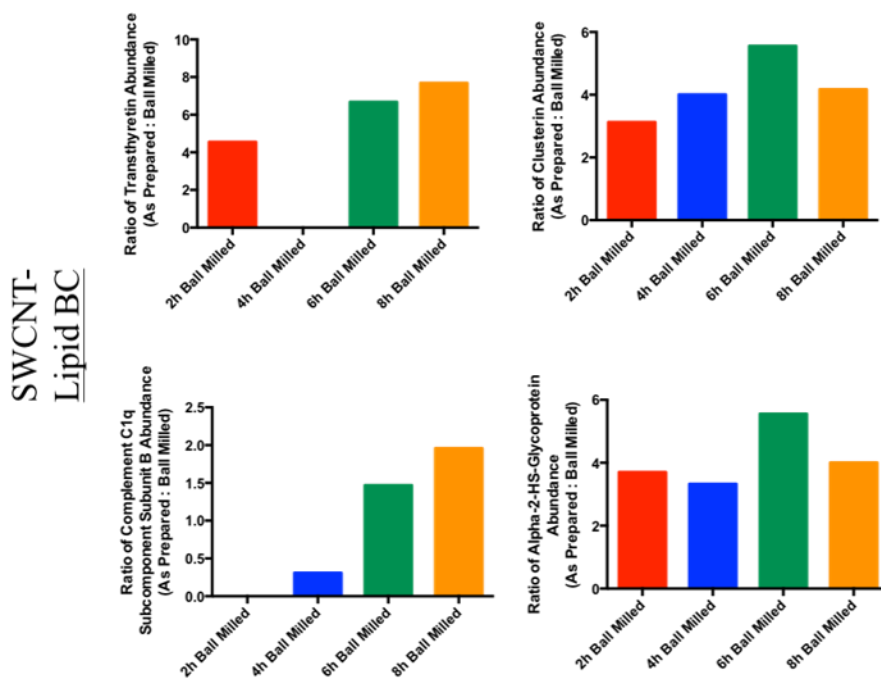
Figure 4.3.6: Differences in relative abundance of specific proteins (Transthyretin, Clusterin, Complement C1q Subcomponent Subunit B, and Alpha-2-HS-Glycoprotein) found to associate with SWCNTs in hyperlipidemic serum due to ball milling time. For normal serum refer Fig. 3.3.11. All ratios are As Prepared SWCNTs : Ball Milled SWCNTs.

Although a majority of proteins were shared between the normal and hyperlipidemic biocoronas on SWCNTs differences were determined regarding their abundance (**Fig. 4.3.6**). Many proteins such as immunoglobulin kappa V-III, apolipoproteins E, C-I, A-II, and A-I, and complement C1q subcomponent subunit B, complement C1s-A subcomponent, complement C3 and complement C1r-A subcomponent were found to be enriched within the hyperlipidemic biocorona on As Prepared SWCNTs. As Prepared SWCNTs in hyperlipidemic serum associated greater amounts of apolipoproteins and complement factors likely due to their increased abundance in hyperlipidemic serum. Many of the shared proteins found to be decreased in the hyperlipidemic compared to the normal biocorona appear to be high abundant serum proteins. This suggests that the increased lipid content maybe competing with them for binding sites on the SWCNTs. Further, this data overall demonstrates that the biocorona is not only different due to structural modification induced by ball milling but also due to the physiological environment. Although they share numerous proteins the abundance of these proteins are not uniform. These variations in abundance further

demonstrate altered biomolecular interactions, distinct biocorona formation, and the possibility for modified cellular responses.

Again, gene ontology was used to evaluate proteins related to specific biological pathways and classes of proteins that associated with SWCNTs. For this comparison of biological pathways and protein classes, proteins that were found to bind in common between normal and hyperlipidemic serums regardless of ball milling were utilized. Further only proteins that were unique and never shared between samples were used to explain pathways and classes that were unique to serum environment. Assessment of commonly associated proteins demonstrated that proteins associated with the biological pathways of blood coagulation, integrin signaling, inflammation-mediated by chemokine and cytokine signaling, vitamin D metabolism, plasminogen activating cascade and others. Assessment of the unique protein components of the biocoronas primarily added proteins to the identified common pathways. The hyperlipidemic biocorona on SWCNTs however uniquely associated glyceraldehyde-3-phosphate dehydrogenase which is involved in the biological pathway of glycolysis. Although most of the proteins that associated with SWCNTs in normal and hyperlipidemic serums were associated with the same biological pathways it is interesting that there were unique proteins that bound. Therefore, classes of the proteins that associated with SWCNTs were evaluated. Proteins that bound in common were found to have been from classes of proteins involved in enzyme modulation, transfer/carrier, defense/immunity, signaling, transporter, receptor and others. Uniquely associated proteins primarily were from similar classes to the ones that were shared of proteins that were shared. The hyperlipidemic biocorona, however,

was found to associate with single proteins from the classes of transcription factor and nucleic acid binding (transcription factor HIVEP2), and isomerase (major urinary protein-1). Again, this assessment demonstrated that although proteins that bound to the SWCNTs were from similar protein classes specific proteins that bound were unique.

4.4 Conclusions

In summary, our study demonstrates the impact of underlying disease states on the formation of the BC on Fe_3O_4 NPs and its implications for the safe development of NPs for biomedical applications. Although numerous studies have demonstrated that the physicochemical properties of NPs result in differential BC formation, few have examined the role of the physiological environment in terms of variations due to underlying disease states. The addition of the lipid BC was determined to influence cellular uptake and activation, thereby having consequences for the safe utilization of NPs. In the current study we investigated a common human disease state, hyperlipidemia, however, numerous other conditions are known to alter physiological environments, which may influence the formation of the NP-BC and toxicity thereby requiring additional investigation. There are also many other biological fluids other than serum that NPs may come into contact with due to their routes of exposure such as bronchoalveolar fluid, gastrointestinal fluid, and others. In order for the safe and effective use of NPs for biomedical applications, it is necessary to evaluate the formation of the BC in different environments and assess its impact on NP function and toxicity.

A common disease-induced alteration in the serum environment can also result in modified biocorona formation. Further, these disease-related changes in the physiological environment demonstrate differences due to SWCNTs ball milling when compared to normal conditions. Toxicological experimentation of exposures to SWCNTs often focuses on end product exposure and healthy/normal physiological conditions. However, often nanomaterials are modified through processes such as ball milling which may influence nanomaterial-biomolecule interactions. In order to protect the population from unintended adverse responses, it is necessary to understand how these modifications in the nanomaterial's surface and the biological environment can alter nanomaterial-biomolecule interactions which may govern biological responses such as toxicity, biodistribution, and clearance.

CHAPTER FIVE

CHARGE TRANSFER INTERACTIONS OF NANOMATERIALS WITH

BIOMOLECULES

5.1 Introduction

There is an immediate need to focus our attention on emerging two-dimensional (2D) layered materials such as graphene, graphene oxide (GO), and BN. Many medical applications are envisaged for 2D materials in multiple areas including cancer drug delivery, clot-resistant coatings for biomedical implants, and biomedical imaging[134]–[139]. In the physiological environment, the high surface area of 2D materials, compared to 0D and 1D materials[140], opens new possibilities for relatively stronger non-covalent biological interactions through efficient π−π stacking and hydrogen bonding with biomolecules present in the biocorona. A critical first step in understanding the formation and subsequent influence of biocorona is to study how 2D materials (essentially equivalent to surfaces) interact with amino acids. The aromatic rings in certain amino acids (e.g., tryptophan, tyrosine, and phenylalanine) could be expected to interact strongly with 2D materials, and thereby adversely influence the transport and uptake of

82

essential amino acids critical for protein synthesis. It is known that deficiencies in even a single essential amino acid (e.g., tryptophan) could alter immunity and increase disease susceptibility.[141] Furthermore, it has been suggested that the adsorption characteristics of a diverse set of small molecules such as amino acids could be used to develop quantitative-structure activity relationships or QSARs for predicting biocoronal fingerprint of ENMs[142]. Therefore, it is important to understand the interactions between 2D ENMs and amino acids in order to guide the emerging medical applications and aid in the development of new toxicity and QSAR models. To this end, we used micro-Raman and photoluminescence spectroscopy combined with electrochemical characterization to study the electronic interactions between three aromatic amino acids (tryptophan, tyrosine, and phenylalanine) and three different types of 2D materials (graphene, GO, and BN). As demonstrated in this study, the interactions between biomolecules and 2D materials significantly perturb the ENM electronic structure, which could be elucidated through changes in the Raman spectra of 2D materials and quantified using cyclic voltammetry. The rationale for choosing this particular set of 2D materials (viz., graphene, GO, and BN) is multi-fold: i) the widely used graphene and GO exhibit strong non-covalent interactions ($\pi-\pi$ stacking and hydrogen bonding) with aromatic molecules due to delocalized electrons or the presence of functional groups, ii) although graphene and BN are structural analogues, they exhibit differences in π-electron cloud distribution. The π-electron cloud is uniformly delocalized in graphene while it is centered near N atoms in BN. Such differences facilitate the investigation of different orientations in $\pi-\pi$ stacking, and iii) while graphene and BN are hydrophobic, GO is

hydrophilic and has been proposed to exhibit possible hydrogen bonding with biomolecules leading to interactions distinct from graphene and BN[143]. Our results show that tyrosine and tryptophan strongly interact with 2D materials, unlike phenylalanine. More importantly, we found evidence for charge transfer between aromatic acids and graphene & GO. Such charge transfer reactions[144] are known to be important for predicting oxidative stress potential of ENMs [145] and developing biomolecular sensors.

Although many physicochemical characteristics of ENMs have been reported to influence ENM-BC, it is not yet clear what combination of these properties could be used to predict ENM-BC formation and evolution [25], [146]. The composition of ENM-BC is known to strongly depend on ENM size and surface charge [6], [9], [27], [58], [119], [124], [147]–[152]. Larger ENMs exhibit a preferential adsorption of higher molecular weight proteins whereas lower molecular weight proteins accumulate more on the surface of smaller ENMs. On the other hand, surface charge is expected to be a key factor in determining protein structural changes [6], [9], [25], [119], [146], [151], [153]. The interactions between ENM surface and proteins could disrupt the structural integrity of proteins in ENM-BC and impact their function or elicit adverse immune responses. The surface coatings or functional groups are physically and chemically more active relative to the core of ENM. For instance, citrate groups adsorbed on the surface of Ag nanoparticles (AgNPs) are negatively charged and provide electrostatic repulsion needed to prevent AgNP agglomeration. Any oppositely charged biomolecules (compared to surface functional groups on ENM) experience a natural electrostatic attraction to adsorb

84

on ENM surface. Proteins with a stronger affinity to the ENM core can quickly displace the initially present functional groups and be irreversibly immobilized on ENM surface by partial or complete denaturation [25], [119], [154]. A combination of many factors including van der Waals forces, hydrogen bridges, charge transfer and other hydrophobic interactions are known to drive protein denaturation [155], [156], [11], [157]. Such factors naturally depend upon ENM physicochemical properties. It is imperative to deconvolute the influence of different physicochemical properties (e.g., surface charge and size) and understand how they differ from each other in influencing protein adsorption and denaturation in ENM-BC.

Here, we experimentally investigated the influence of AgNP surface charges on adsorption and denaturation of apolipoprotein A-I (ApoA-I). Considering that ApoA-I is one of the most abundant proteins in AgNP-BC irrespective of AgNP size [124], its adsorption on AgNPs with different surface coatings could provide new insights into the role of surface charges in ENM-BC. ApoA-I is the major protein component of high-density lipoprotein (HDL). It adopts a shape similar to a horseshoe of dimensions 12.5x8x4 nm with high α-helix content [53], [158]–[161]. The helices in ApoA-I are predicted to be amphipathic, with the hydrophobic (/hydrophilic) face mediating lipid (/aqueous) interactions. The thermodynamic drive to minimize the aqueous exposure of the hydrophobic residues is one of the major factors in ApoA-I adsorption on AgNPs [162], [163]. Our light scattering and surface charge studies on 100 nm AgNPs (with four different functional groups) revealed that the binding of ApoA-I on AgNPs is sensitive to their surface charge and functionality. While ApoA-I exhibited a strong affinity for both

positively and negatively charged AgNPs, its secondary structure exhibited more pronounced changes for two surface functionalities viz., lipoic acid and branched polyethyleneimine (bPEI). In this article, we explain the observed secondary structural changes in terms of the electronic charge transfer, gleaned from electrochemical cyclic voltammetry experiments, between ApoA-I and functionalized AgNPs. Lastly, the displacement of positively charged bPEI by ApoA-I and the structural changes of ApoA-I on AgNP-lipoic acid were found to induce a significant increase in their ability to generate reactive oxygen species (ROS). Our results provide new insights into the role of AgNPs surface charge in ENM-BC formation and its influence on bioresponse.

5.2 Materials and methods

Graphene was synthesized using chemical exfoliation technique. Bulk graphite (~1 g) was suspended in 100 mL of N-methyl-2-pyrrolidinone (NMP) and sonicated using 1/8" tip sonicator (Branson 250) at 100 W for 2 h. After sonication, the suspension was centrifuged at 3000 rpm for 30 mins, and the supernatant was filtered through 0.45 μm nylon filter and re-suspended in 100 mL of fresh NMP. This fresh solution was sonicated again for 6 h and centrifuged at 1500 rpm for 1 hr. The supernatant was then vacuum filtered using a 0.45 μm nylon filter. The filtered powder was washed several times using deionized water to remove residual NMP and air-dried to obtain exfoliated graphene samples. GO was synthesized using the standard Hummer's method described elsewhere[164]. BN powder was obtained from Graphene Supermarket (SKU: BN-

100G). It should be noted that our infrared spectroscopy studies showed that GO contained several functional groups including hydroxyl, carboxyl, and epoxide functionalities[164]. All pure amino acids were purchased from Sigma-Aldrich. For studying the interactions with amino acids, 100 µg of ENMs (graphene, GO, and BN) were incubated for 12 hrs in 1 mL solution of amino acids. After incubation, the samples were centrifuged at 13,000 rpm and the supernatant was removed. The samples were washed thrice to remove any amino acids not adsorbed on ENMs and were finally suspended in DI water. For transmission electron microscopy (TEM), the samples were suspended on a 400-mesh Cu grid and the TEM images were acquired using Hitachi H-7600 microscope. Micro-Raman spectroscopy was performed using 514.5 nm Ar+ ion excitation coupled to a Renishaw micro-inVia spectrometer equipped with a 50x objective and Peltier-cooled CCD. For Raman measurements, the samples were drop casted on a microscope slide and were gently air-dried before collecting the Raman spectrum. Photoluminescence measurements were obtained using a Horiba-Jobin Yvon nanolog spectrometer equipped with a liquid-nitrogen cooled CCD.

An aqueous solution of AgNPs (100nm, NanoXact, Nanocomposix) with citrate, polyvinylpyrrolidone (PVP), branched polyethyleneimine (bPEI) and lipoic acid as capping agents were purchased. ApoA-I from human plasma (MW = 28.3KDa) was purchased from Sigma-Aldrich. Different ApoA-I concentrations (0-4 g/L) were considered with AgNPs (50 µM) to study hydrodynamic size and zeta potential using Zetasizer Nano ZS90 (Malvern Instruments). For transmission electron microscopy (TEM) characterization of the corona formation, AgNPs with ApoA-I biocorona were

stained with 0.1% osmium tetroxide (OsO_4) by incubating for 30 minutes. These samples were then drop casted on 400 mesh Cu grid and TEM images were acquired using a Hitachi H-7600 microscope.

Electrochemical studies were performed using a Gamry reference 3000 electrochemical system. Cyclic voltammetry (CV) measurements were obtained in a three-electrode setup with Ag/AgCl as the reference electrode, platinum wire as the auxiliary/counter electrode. GO, and boron nitride samples were drop casted on a glassy carbon electrode (diameter: 3 mm) and air dried for 12 hours. ENMs adsorbed on the glassy carbon were used as the working electrode with a high purity Pt counter electrode. Stock solutions containing tyrosine, tryptophan, and phenylalanine with varying concentrations were prepared in 0.05M PBS solution (electrolyte). For other study, AgNPs formed the working electrode. We used ApoA-I solution as the electrolyte to study charge transfer. It should be noted that we used concentration ranges based on the physiological levels of ApoA-I (~1-1.3 g/L) for electrochemical studies to avoid high current values that could result in artifacts in charge transfer measurements.

Circular Dichroism (CD) measurements were performed using Jasco spectropolarimeter (J-810) to analyze secondary structures of ApoA-I after the biocorona formation on AgNPs. Samples were prepared for CD analysis with suspensions of AgNPs and ApoA-I corresponding to the molar ratio of 1:600 and incubated at 40 °C for 8h. The CD spectra were measured at room temperature with a wavelength range from 200-300nm for all the samples at a scan speed of 50nm/min. Background correction was applied with pure AgNP suspension.

Reactive oxygen species (ROS) were evaluated using dichlorofluorescein (DCF) assay via flow cytometry (by counting 10000 cells per sample). Macrophages were grown to 90% confluence and exposed to 30 μg/mL of AgNPs for 1h. All the measurements were performed in triplicates.

5.3 Results & dicussion

5.3.1 Two-dimensional nanomaterials with aromatic amino acids
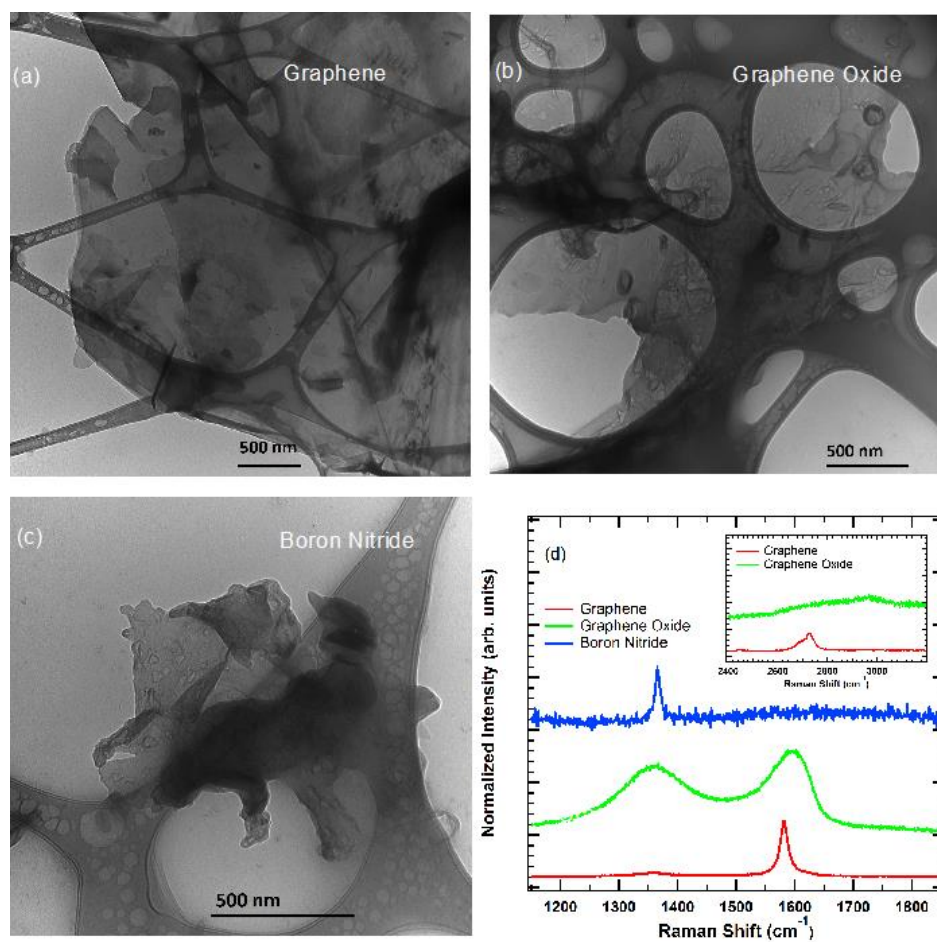
Figure 5.3.1: Representative transmission electron microscope images for (a) graphene, (b) graphene oxide, and (c) BN. (d) Raman spectra for as-prepared graphene (red), graphene oxide (green) and boron nitride (blue). The D-band (~1350 cm^{-1}) and the G-band (~1590 cm^{-1}) for graphene oxide exhibit significant broadening due to the presence of defects. Graphene (G-band ~1585 cm^{-1}) and BN (~1366 cm^{-1}) exhibit sharp Raman features indicative of good crystallinity.

As shown in **Fig. 5.3.1d**, graphene and GO exhibited disorder (D-band) and graphitic (G-band) bands ~1350 cm^{-1} and 1581 cm^{-1} (~1598 cm^{-1} for GO) respectively. The presence of defects in GO, induced during harsh chemical oxidation process in Hummer's method, resulted in a highly intense D-band and a significant broadening of the G-band relative to graphene. While graphene samples showed a two-peaked 2D-band ~2700-50 cm^{-1} (see Fig. 5.2.1d inset) suggesting it to be few-layered (~5-6 layers), the 2D band in GO was suppressed due to oxidation. BN sheets exhibited a strong peak ~1366 cm^{-1} in their Raman indicating excellent crystallinity similar to graphene.

Previously, many theoretical studies[143], [165], [166] investigated the interactions of aromatic amino acids with carbon-based ENMs such as carbon nanotubes (CNTs), graphene, and GO. These studies observed that the aromatic rings of amino acids prefer to stack on CNTs and graphene sheets due to the presence of π−π interactions[143], [165]. In contrast, it was predicted that GO interacts with biomolecules (e.g., proteins, amino acids, nucleobases) through hydrogen-bonding interactions[143]. To experimentally validate such predictions, we characterized the

amino acid adsorption on different ENMs using isotherms obtained through photoluminescence (PL) studies (**Fig. 5.3.2**). It is well known that aromatic amino acids such as tryptophan, tyrosine, and phenylalanine exhibit strong PL when excited by ultra-violet light[144]. As discussed in the experimental section, we incubated ENMs with different concentration of amino acids (within their physiological concentration range 0-70 μm/L) and obtained the isotherms by measuring the PL arising from residual amino acids on ENMs after three rounds of washing. Although it is possible to fit the observed isotherms to Langmuir-like models, we did not derive any quantitative conclusions because many assumptions for Langmuir isotherms are invalid in our case (e.g., the irreversibility of adsorption)[167] [58]. Furthermore, the quenching of aromatic amino acid PL when interacting with ENMs could lead to incorrect quantitative results. Nonetheless, PL data could be used to glean useful qualitative information regarding the relative affinity among 2D materials and the orientation and stacking of amino acids.
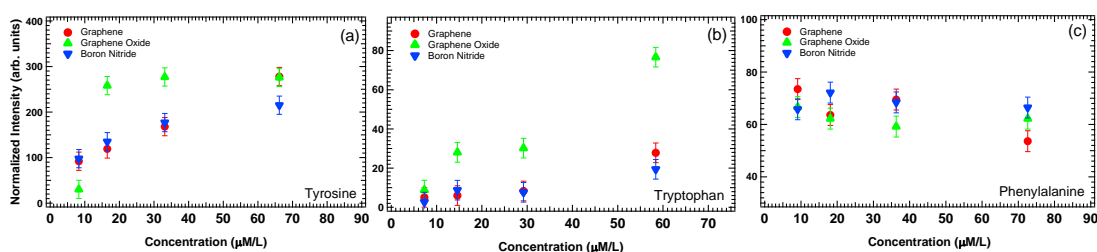
Figure 5.3.2: Adsorption isotherms for (a) tyrosine, (b) tryptophan, and (c) phenylalanine on graphene, BN, and graphene oxide. Graphene oxide showed significantly higher adsorption for tyrosine and tryptophan, possibly due to the formation of hydrogen bonds, compared to graphene and BN (which exhibit $\pi-\pi$ interactions with amino acids).

However, phenylalanine showed similar adsorption on all 2D materials that were relatively independent of concentration.
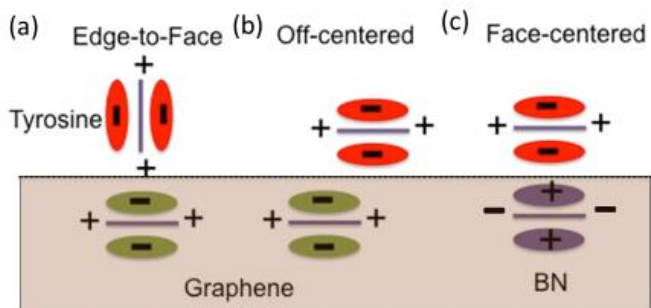
Figure 5.3.3: (a) A graphene sheet containing p-electrons can be viewed as a quadrupole (as depicted by green lobes in the lower panel) with a negative charge above and below the sheet and a positive charge around the edges. Similarly, the aromatic ring (shown in red) in tyrosine, tryptophan, and phenylalanine could be viewed as quadrupoles with charge distribution similar to graphene. Amino acids (e.g., tyrosine shown above graphene sheet) exhibit either edge-to-face or off-centered (b) stacking due to quadrupole-mediated p-p interactions. (c) BN exhibits positive charge (shown in purple) above and below the sheet due to the presence of N atoms that pull the electrons away from the center. Accordingly, the amino acids may prefer face-centered stacking, unlike graphene.

Tyrosine exhibited similar adsorption trends for graphene and BN unlike GO (**Fig. 5.3.2a**). As predicted from density functional theory[143], such contrasting isotherms are expected due to the formation of hydrogen bonds (H-bonds) in the case of GO. Interestingly, the adsorption curves for graphene and BN were similar although the π-electron cloud is uniformly delocalized in graphene while it is centered near N atoms in BN. The delocalized π-electron cloud in graphene induces a quadrupole moment with a partial negative (/positive) charge above and below (/in-plane) the sheet (see the lower panels in **Fig. 5.3.3a** and **b**). Tyrosine also exhibits a similar quadrupole with negative charges above and below the aromatic ring. Thus, it may be expected that tyrosine prefers perpendicular edge-to-face interactions or off-centered parallel stacking in lieu of face-centered parallel stacking (**Fig. 5.3.3a** and **b**). On the other hand, in case of BN, the scenario is different because N is a relatively strong electron-withdrawing group that polarizes the π-electron density away from the core, and thereby reverses the direction of the overall quadrupole moment (compared to graphene) by inducing a central area of relative electron deficiency and localization of π-electrons around N atoms (lower panel in **Fig. 5.3.3c**). Accordingly, tyrosine may prefer face-centered stacking on BN surface (**Fig. 5.3.3c**). The edge-to-face orientation in the graphene-tyrosine complex (**Fig. 5.3.3a**) involves less active area of interaction and thus should allow more tyrosine molecules to stack on graphene as opposed to off-centered stacking. Nonetheless, the adsorption isotherms for graphene and BN (which favors only face-centered stacking for tyrosine) are similar suggesting that the edge-to-face interactions in graphene could be possibly ruled out. In case of GO, as observed in theoretical calculations[143], the hydroxyl group

of the phenolic ring in tyrosine may form H-bonds with the hydroxyl groups on GO leading to higher adsorption. Returning to **Fig. 5.3.2a**, we found that the adsorption on GO saturated abruptly beyond 15 μM/L for tyrosine possibly due to the saturation of limited hydroxyl groups on the surface of GO. Furthermore, the formation of H-bonds, which necessitates a close proximity between both hydroxyl groups (one from GO and another from tyrosine), may also prevent multilayer adsorption in GO.

Interestingly, tryptophan exhibited a monotonically increasing trend for adsorption on GO unlike tyrosine (**Fig. 5.3.2b**). The hydroxyl groups of GO are predicted to form H-bonds with indole ring hydrogen in tryptophan[143]. In addition to the H-bonds, tryptophan may exhibit relatively stronger π-π interactions with GO due to the presence of extended π-cloud in the indole ring. The adsorption of tryptophan on graphene and BN was similar to tyrosine and could be entirely attributed to π-π stacking arising from interactions of quadrupoles induced by π-electron cloud (off-centered stacking for graphene and face-centered for BN similar to the case of tyrosine).
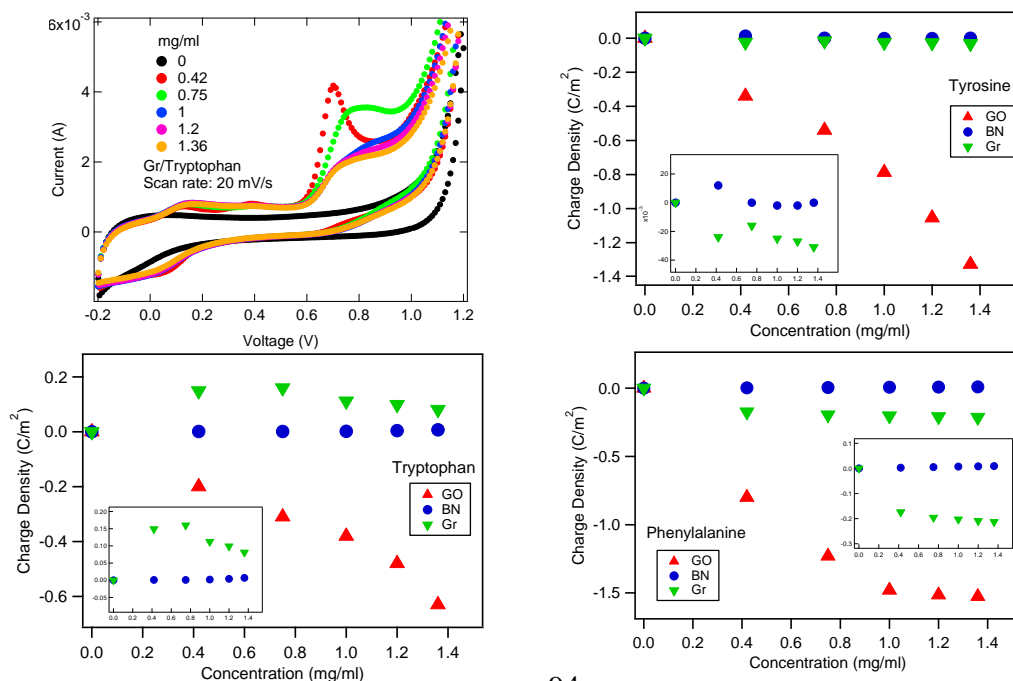
Figure 5.3.4: (a) Cyclic voltammetry loops for graphene and tryptophan show the appearance of a new peak ~0.6-0.8 V indicating irreversible charge transfer. (b-d) Charge density isotherms derived from their corresponding CV loops for different 2D materials and amino acid combinations. Insets shows zoomed in view of the plot of charge density vs concentration for Gr and BN.

There was no significant difference in the adsorption of phenylalanine on graphene, BN, and GO. This result is not surprising because the structures of tyrosine and phenylalanine differ only by the presence of an extra hydroxyl group. The lack of hydroxyl group in phenylalanine (unlike tyrosine) precludes the possibility of H-bonds and thereby results in a lower affinity for GO. The qualitative conclusions, based on PL data, were further confirmed using cyclic voltammetry studies discussed later in **Fig. 5.3.4**.

While the PL studies provide insights into physical adsorption and affinity through π-π interactions, the nature of chemical bonding can be understood through perturbations in electronic structure. We used cyclic voltammetry and micro-Raman spectroscopy to understand the influence of amino acid adsorption on the electronic structure of ENMs. We performed cyclic voltammetry (CV) measurements with ENMs as a working electrode in amino acid electrolyte solution (**Fig. 5.3.4**). In CV characterization, the application of gate voltage on the working electrode (i.e., ENMs in our case) modulates its electronic energy levels, which when in the vicinity of energy levels of the amino acids (present in the electrolyte) can result in a charge transfer. For

quantifying the electrochemical charge transfer, we first obtained a base CV curve with 0.05 M PBS electrolyte solution containing no amino acids (see **Fig. 5.3.4a**). Subsequently, amino acids aliquots of varying concentrations were introduced into the electrochemical cell and scan rate normalized CV loops were obtained for each concentration. The total amount of charge-transferred was obtained by integrating the area enclosed by the CV curves and subtracting the base area (from the CV curve in 0.05M PBS electrolyte solution). As shown in **Fig. 5.3.4b-d**, we found that the charge-transfer isotherms for all ENMs and amino acid combinations showed clear trends as a function of concentration.

In a typical CV plot, a peak in current (in a current vs. voltage plot such as the one shown in **Fig. 5.3.4a**) or changes in the CV loop area indicate the presence of charge transfer between the electrolyte (i.e., amino acid in PBS solution in our case) and the working electrode (i.e., ENMs). The changes in CV loop area could occur due to two reasons: i) chemisorption or binding of amino acids with ENMs results in an irreversible reaction, which appears as a peak in the CV loop (e.g., graphene/tryptophan in **Fig. 5.3.4a**) and thereby changes the enclosed area, and ii) physisorption, which decreases the available surface area of ENMs for ion adsorption leading to a decrease in the total loop area.

The charge density isotherms (**Figs. 5.3.4b-d**), obtained from the CV curves, show the combined effects of both physi- and chemisorption. We observed that GO exhibited the largest changes in charge density suggesting the strong interaction between GO and amino acids as observed in PL (cf. **Fig. 5.3.2**) and previous theoretical results

96

[143]. The charge density changes in graphene and BN were significant (see insets in **Fig. 5.3.4b-d**) but much smaller compared to GO. It should be noted that the base CV loops for GO in pure PBS solution enclose a much larger area (~ 1.75 C/m^2) compared to graphene and BN ($\sim 50\text{-}300$ mC/m^2) due to the presence of quinone, carboxyl, and epoxide functional groups. The net reduction of CV loop area for GO in the presence of amino acids is a combined effect of physi- and chemisorption. However, CV measurements alone cannot distinguish the difference between physical and chemical interactions. On the other hand, the micro-Raman spectrum of carbon-based ENMs is highly sensitive to charge transfer and may be used to resolve the difference between chemical and physical interactions. Carbon-based ENMs exhibit strong Raman features such as the G and 2D-bands (*cf.* **Fig. 5.3.1d**), which are known to upshift (downshift) when any acceptor (donor) species interact via hole (electron) transfer[144]. As documented in the literature[168], the peak frequencies and shape of G- and 2D-band depend on the Fermi energy (E_F) of carbon-based ENMs. In a simplistic picture, an upshift (downshift) in E_F (or equivalently Fermi velocity) results in a downshift (upshift) in G- and 2D-bands. Previously, Rajesh *et al.* [165] theoretically showed that the E_F of graphene and CNTs undergoes an overall shift (as large as 0.21 eV) upon interaction with amino acids due to charge transfer. Indeed, their study found that the degree of shift in E_F of ENM-amino acid complexes varied as a function of the polarizability of the aromatic moiety of the adsorbed amino acid molecules. In our studies, GO displayed a downshift in the G-band frequency (**Table 5.3.1** and **Fig. 5.3.5a**) for tryptophan and phenylalanine. It should be noted that the 2D band is absent in GO due to the disruption of the so-called

double-resonance Raman process upon the oxidation of graphene lattice[169]. The shifts in G-band are expected due to the formation of chemical bonds, as ascertained in the reduction in charge density from CV measurements (*cf.* **Fig. 5.3.4**). The magnitude of the shifts in G-band of GO was highest for phenylalanine concurring with the CV data (**Fig. 5.3.4d**). Interestingly, tyrosine (unlike phenylalanine and tryptophan) was found to upshift the G-band in GO although a distinct reduction in the charge density was observed in CV measurements (**Fig. 5.3.4b**). Such an observation suggests that the physisorption of tyrosine, which may preclude the participation of functional groups on GO in electrochemical charge storage, overwhelmed the chemisorption leading to the reduction in charge density in CV measurements.
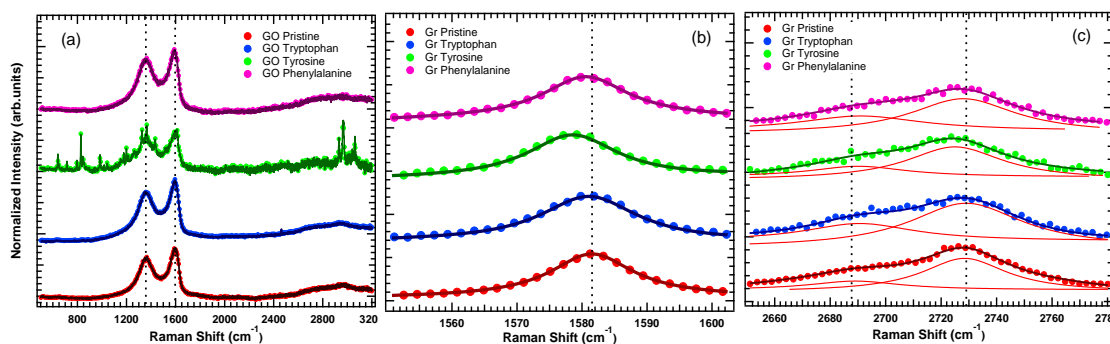
Figure 5.3.5: (a) Raman spectra of graphene oxide-amino acid complexes showed significant shifts due to the formation of hydrogen bonds with amino acids. The starred peaks arise from tyrosine due to its high Raman cross-section. (b) Raman spectra for graphene-amino acids complexes show shifts in G- and 2D-bands (in (b) and (c) respectively) indicating the involvement of charge transfer between amino acids and

graphene. Solid lines in indicate fits to the experimental data. The red curves in panel (c) are deconvoluted peaks for 2D-band in graphene.

	Pristine		Tyrosine		Tryptophan		Phenylalanine	
	Position (cm^{-1})	FWHM (cm^{-1})	Position (cm^{-1})	FWHM (cm^{-1})	Position (cm^{-1})	FWHM (cm^{-1})	Position (cm^{-1})	FWHM (cm^{-1})
Graphene (G band)	1581.5	15.36	1578.5	16.94	1581.1	18.27	1580.5	15.86
Graphene Oxide	1598.3	109.96	1599.9	95.73	1596.7	105.8	1593.9	104.02
Boron Nitride	1366	10.42	1365.7	10.18	1365.5	10.79	1366	10.63

Table 5.3.1: The positions of Raman peaks for graphene, graphene oxide, and BN-amino acid complexes derived from Fig 5.3.5

	Pristine		Tyrosine		Tryptophan		Phenylalanine	
	Position (cm^{-1})	FWHM (cm^{-1})	Position (cm^{-1})	FWHM (cm^{-1})	Position (cm^{-1})	FWHM (cm^{-1})	Position (cm^{-1})	FWHM (cm^{-1})
Graphene (2D band)	2689.1	40.12	2683	42.47	2690.6	48.04	2691	53.99
	2728.4	37.04	2722	42.40	2729	49.45	2727	45.86

Table 5.3.2: The positions of deconvoluted 2D-band for graphene derived from Fig. 5.3.5c.

In case of graphene, a significant downshift was observed in both G- and 2D-bands when interacting with tyrosine (**Fig. 5.3.5** and **Table 5.3.1**). As explained earlier, this downshifts in G- and 2D-bands of graphene-tyrosine complex could be understood in terms of upshift in E_F induced by electron-transfer from tyrosine[165]. Although a discernible shift was observed for graphene-tyrosine complex, the widths of G- and 2D-

band did not change significantly. The presence of chemical interactions between graphene and tyrosine (through electron transfer) suggests that the adsorption may predominantly be mono- or bi-layered because only the molecules within the vicinity of graphene (~0.4-1 nm) can exhibit charge transfer and bind strongly. Based on the Raman measurements, it is plausible that the minute changes in charge density (**Fig. 5.3.4b**) resulted solely from chemisorption. On the other hand, tryptophan and phenylalanine (**Fig. 5.3.5** and **Table 5.3.1**) resulted in a significant broadening of G- and 2D- bands despite little or no shift (i.e., no charge transfer) in the frequency (**Tables 5.3.1** and **5.3.2**). It is likely that tryptophan and phenylalanine exhibit multilayer physisorption unlike monolayer chemisorption in the case of tyrosine. In such a scenario, the multilayers of amino acids could contribute prominently to the non-radiative decay of excited electrons, which could, in turn, result in the observed broadening of G- and 2D-bands. Interestingly, tryptophan exhibited an increase in the charge density due to the presence of a new peak in the CV loop (*cf.* Fig. **5.3.4a** and inset in **Fig. 5.3.4c**) suggesting that both chemisorption and physisorption are involved.

In case of BN, we did not observe appreciable changes either in CV measurements or Raman spectra suggesting the absence of chemisorption. Such a result is expected due to the localization of π-electrons around N in BN unlike uniformly distributed π-electron cloud in graphene or chemically active functional groups in GO.

5.3.2 Effect of surface functional groups on AgNP-apolipoprotein corona
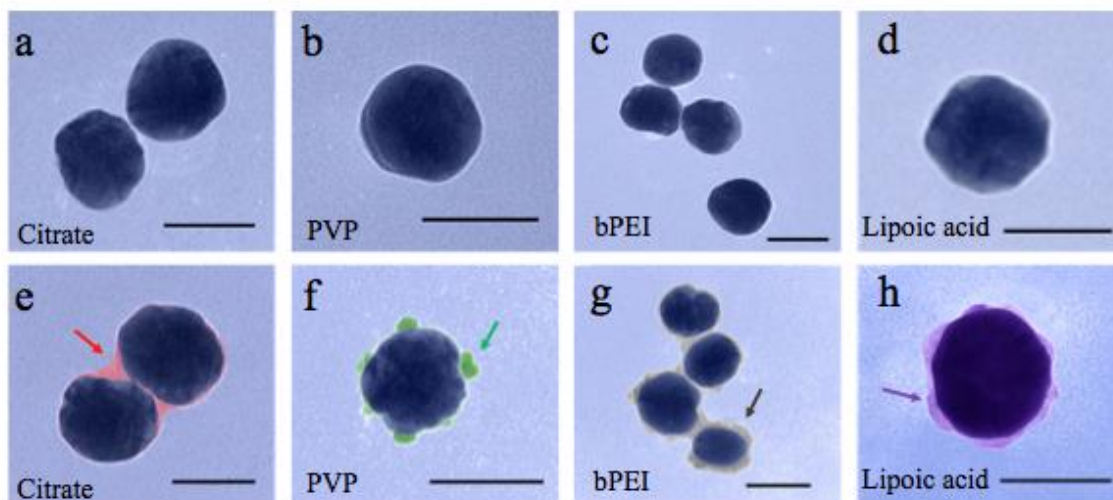
Figure 5.3.6: Transmission electron micrographs showing as-purchased Ag NPs (a-d) with citrate, PVP, bPEI and lipoic acid coatings respectively. The presence of biocorona (see arrows in e-h) upon incubation with ApoA-I was assessed using OsO_4 staining as shown in (e-h). Scale bar is 100 nm.

As shown in **Fig. 5.3.6**, TEM images confirmed that all four types of AgNPs (citrate, PVP, bPEI, and lipoic acid coated) are spherical in shape with a similar size ~100 nm in their dehydrated state. ApoA-I appeared to non-uniformly adsorb on to AgNPs (**Fig. 5.3.6e-h**) with a strong preference for rough edges (see **Fig. 5.3.6.**f and **h**). Given the small size of ApoA-I protein (hydrodynamic size ~ 8 nm) relative to 100 nm AgNPs, the corona possibly consisted of multiple ApoA-I layers. In some cases, ApoA-I was

found to envelop AgNP aggregates in the dehydrated state under TEM similar to previous observations [170].

Although all AgNPs have the same size in their dehydrated size (as evidenced by TEM), we found that their hydrodynamic sizes (S_{HD}) differed from each other in the following order: bPEI (~135 nm) > PVP (~120 nm)>lipoic acid (~108 nm)> citrate (~100 nm). This trend is expected based on the size of the surface coating molecules where polymers (bPEI and PVP) are significantly larger than the smaller citrate and lipoic acid groups. The difference in the surface coatings was also evident from their zeta potential (ζ) measurements where bPEI is positively charged with a relative low ζ ~8.89 mV while citrate (ζ~−39 mV), PVP (ζ~−37 mV), and lipoic acid (ζ~−28 mV) exhibited larger negative values. Based on the zeta potential measurements, negatively charged ApoA-I ((ζ~−30−36 mV [170]) is expected to display strong electrostatic attraction towards bPEI coated AgNPs and possibly experience some repulsion from other negatively charged AgNPs.
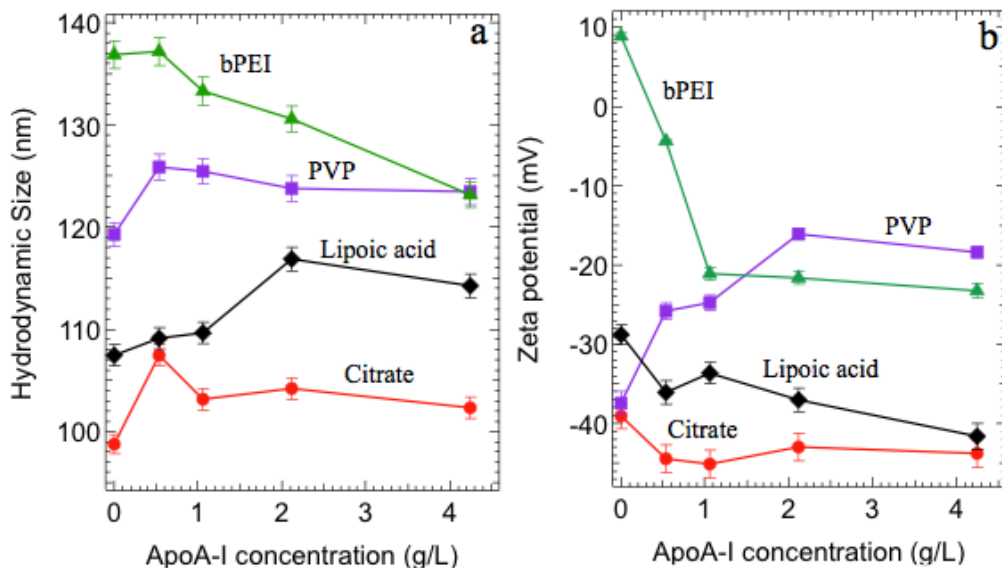
Figure 5.3.7: (a) The hydrodynamic size of AgNPs was found to change with increasing ApoA-I concentrations with saturation >2 g/L for AgNP-PVP, citrate, and lipoic acid coatings. AgNP-bPEI, however, did not show such saturation. (b) The zeta potential measurements showed clear changes indicating the displacement of surface coatings by ApoA-I. All surface coatings showed saturation in zeta potential changes >2 g/L excepting AgNP-lipoic acid. Based on (a) and (b), it could be inferred that AgNP-bPEI and AgNP-lipoic acid do not show saturation in protein adsorption even at high ApoA-I concentrations. It should be noted that the physiological concentration of ApoA-I is 1.3-1.5 g/L.

We studied the evolution of S_{HD} and ζ of AgNPs in the presence of ApoA-I (**Fig. 5.3.7a** and **b**). In case of bPEI, ζ decreased rapidly and changed from a positive to a

negative value in the presence of ApoA-I. Indeed, ζ values at higher ApoA-I concentrations (~-24 mV) suggest that ApoA-I stabilized AgNPs better than bPEI. A concomitant decrease in S_{HD} of AgNP-bPEI suggested that ApoA-I has a higher affinity for AgNP surface and ultimately replaced bPEI on AgNP surface. The surface potential of AgNP-PVP decreased with increasing concentration of Apo-A1 similar to bPEI. However, S_{HD} showed a sharp increase with a rapid saturation at a relatively low concentration of ApoA-I (<1 g/L). Unlike AgNP-bPEI and AgNP-PVP, a significant increase in S_{HD} for AgNP-lipoic acid was observed only at higher ApoA-I concentrations (>2 g/L). The observed changes in both ζ and S_{HD} were much slower for lipoic acid and can be rationalized in terms of relatively strong Ag-S interactions (binding energy ~217 kJ/mol [171]) between sulfur in lipoic acid and the surface of AgNPs. Interestingly, AgNP-citrate showed relatively smaller changes in S_{HD} and ζ compared to other surface coatings. Nevertheless, in all cases, the increase in S_{HD} did not indicate the formation of AgNP aggregates unlike in the dehydrated state. We found that the changes in S_{HD} and ζ saturated above 2 g/L for all surface coatings excepting bPEI and lipoic acid. While S_{HD} for AgNP-lipoic acid appears saturated, its ζ did not suggest that protein adsorption did not saturate. When the average time between consecutive collisions (τ_c) of ApoA-I with AgNPs is greater than ApoA-I configurational relaxation time (τ_R), there is sufficient time for ApoA-I to unfold on AgNP surface and thus could form a disorganized corona. This condition ($\tau_c > \tau_R$) occurs at low ApoA-I concentrations (<2 g/L) for AgNP-PVP and AgNP-citrate. Indeed, disorganized protein agglomerates can be clearly observed on AgNP-PVP surface. However, at higher $\tau_c \sim \tau_R$, ApoA-I cannot completely

unfold due to rapid collisions between ApoA-I and AgNPs. This results in a densely packed corona where ApoA-I retains much of its secondary structure. Based on the results described in Fig. 2, it may be expected that the corona layer presents directly on the AgNP surface is densely packed > 2g/L for all cases excepting bPEI and lipoic acid, and thus saturates further changes in S_{HD} and ζ. The collision frequency (f_c=1/ τ_c) of ApoA-I molecules with AgNP surface may be calculated using the Smoluchowski equation [172]

$$f_c=1/\ \tau_c =2\pi DCdN_A \qquad\qquad (5.2.1)$$

where D= 120 um^2 s^{-1} is the room-temperature diffusion coefficient of the ApoA-I [173], d= 12.8 nm is the room-temperature hydrodynamic diameter of ApoA-I [174] and, N_A=6.023 $\times$ 10^{23} mol^{-1} is the Avogadro number, and C is the ApoA-I concentration at which adsorption saturates. At C= 2 g/L, we find that τ_c ~ 90 μs, which is on the same scale as protein unfolding timescales. It should be noted that the value of τ_c derived from the above analysis only provides an estimate for the unfolding timescales. Nevertheless, it could be used to infer that ApoA-I molecules will collide on a timescale of few tens of μs at physiological concentrations ~1.3-1.5 g/L, leading to a rapid saturation in adsorption [175].

It is well known that some proteins change their conformation upon binding to nanoparticle surfaces. Previously, Cukalevski *et al.* studied the conformational changes of ApoA-I on polystyrene (PS NPs) and NIPAM/BAM (N-isopropylacrylamide-co-N-

tert-butylacrylamide) small sized nanoparticles (<60 nm) with large curvature and different surface charges [163]. They found that plain and negatively charged PS NPs (diameter ~23-24 nm) slightly increased the helical structure of ApoA-I in the range of 2-15 % whereas positively charged PS NPs (diameter ~57 nm) slightly reduced the amount of helical structure by ~10%. A similar study by Li *et al.* on 30 nm negatively charged AgNPs and ApoA-I [170] also found a reduction of helical content by ~15-20%. Although these previous reports provide some preliminary understanding of ApoA-I interactions with ENMs, a controlled study with AgNPs of the same size but different surface coatings is necessary to understand the influence of surface change. In this study, we used 100 nm AgNPs with different surface coatings to clearly distinguish the effects of surface charges and understand the mechanisms involved in ENM-induced protein unfolding. In our circular dichroism (CD) studies, we found that ApoA-I exhibited a significant decrease in the helical content by >40% on all 100 nm. ApoA-I unfolding is more pronounced in our case due to the large AgNP size compared to previous studies [163], [170]. The CD spectra revealed that the changes in helical content were more prominent for AgNP-bPEI and AgNP-lipoic acid compared to PVP and citrate coatings. Indeed, the helical content of ApoA-I may be completely suppressed for these AgNPs (**Fig. 2.2.1**). These changes were accompanied by a concomitant increase in β-sheet and random chain structures in the following order: AgNP-PVP<AgNP-citrate<AgNP-lipoic acid~AgNP-bPEI.
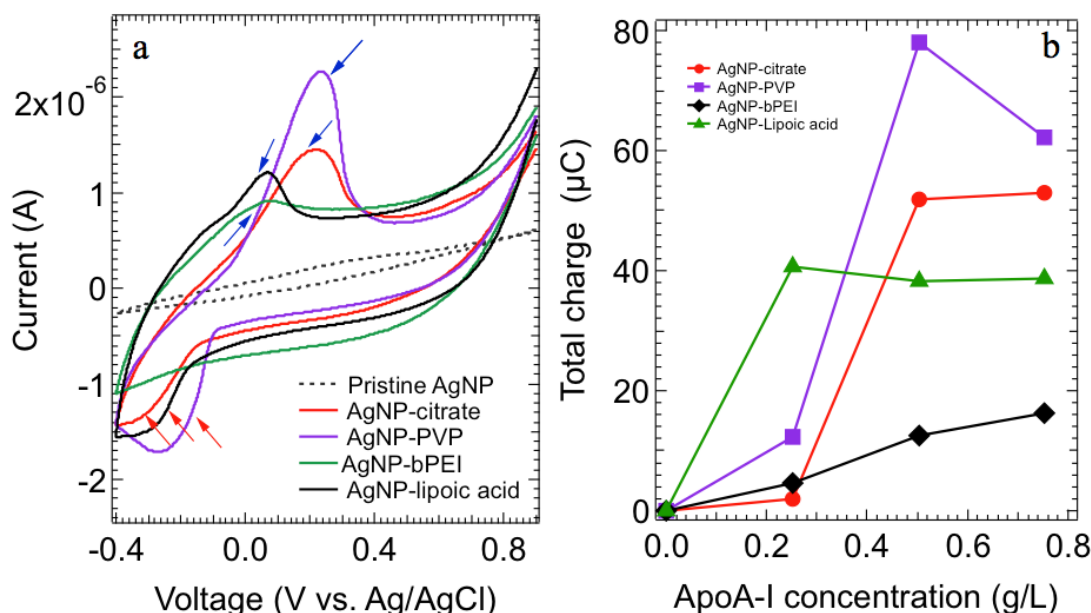
Figure 5.3.8: (a) Cyclic voltammetry scans showed the appearance of a peak (blue arrows) for AgNP electrodes in ApoA-I electrolyte suggesting the presence of charge-transfer stabilizing interactions. The peak for AgNP-bPEI occurred only in the forward scan (going from -0.4 to 0.8 V) indicating irreversible charge transfer. A valley (red arrows), the representative of reversible charge transfer, was observed for other surface coatings on the reverse scan (0.8 to -0.4 V). (b) The total charge enclosed by the CV curves in (a) displayed clear increasing trends with ApoA-I concentration confirming that the charge-transfer occurs due to interactions between ApoA-I and AgNPs.

As shown in **Fig. 5.3.8**, we performed cyclic voltammetry (CV) to develop a mechanistic understanding of surface charge dependent conformational changes observed in CD spectra (**Fig. 2.2.1**). Proteins interact with ENM surfaces through intramolecular bonds, ionic bonds, and charge transfer [156], [157]. A stabilizing charge may be

107

transferred between proteins and ENM surface depending upon their electronic energy levels, and the adsorbed proteins may undergo various conformational changes during the electron exchange process. Charge transfer processes and the relative differences between electronic energy levels of protein and ENM surface could be ascertained through peaks in current (i.e., charge flow) during a CV scan [58], [172].

In the CV scan of AgNPs without ApoA-I (dashed lines in **Fig. 5.3.8a**), we did not observe any peaks for all four surface coatings. The addition of ApoA-I to the electrolyte resulted in a change in voltammetric responses with the appearance of a new peak (blue arrows in **Fig. 5.3.8a**), which in turn increased the current considerably. This new peak cannot be attributed to desorption of adsorbed hydrogen (which is known to occur ~990 mV vs. Ag/AgCl electrode [172]) as the peak appeared at appreciably low potentials < 350 mV for all the coatings. We attribute this peak to stabilizing electron transfer between ApoA-I and AgNP surface. The electron transfer occurs only when the electronic energy levels of ApoA-I are in the vicinity of AgNPs energy levels. The so-called Fermi energy (E_F) or the chemical potential of AgNPs (that serve as the working electrode in our CV measurements) is decreased (/increased) when the voltage in a CV scan is increased (/decreased). An electron transfer occurs when the energy levels of ApoA-I match the altered E_F of AgNPs at a particular voltage in the CV scan. This peak voltage for electron transfer was found to be much lower for AgNP-bPEI and AgNP-lipoic acid (~60 mV) compared to AgNP-citrate and AgNP-PVP (~300 mV) suggesting that the surface coatings have considerable influence of electron transfer reactions between ApoA-I and AgNPs (**Fig. 5.3.8a**). The surface coatings have different electronic

108

nature relative to each other and may lead to charge transfer peak at different potentials. The electrochemical charge transfer (Q) can be quantified by calculating the area enclosed by CV curves (Fig. 4a). We found that all the AgNPs showed an increase in Q with increasing ApoA-I concentration concurring with our hypothesis that the observed peak arises from electron transfer between ApoA-I and AgNPs. The normalized areal charge density (Q/cm^2) at higher ApoA-I concentrations showed the following trend: AgNP-PVP>AgNP-citrate>AgNP-lipoic acid>AgNP-bPEI. This trend appeared to match the changes in CD spectra described earlier in **Fig. 2.2.1**.

An interesting feature in the CV scans was the presence of an irreversible charge transfer peak for AgNP-bPEI. For bPEI coating, a peak was observed only when the voltage was increasing in the CV scan indicative of irreversible charge transfer. On the other hand, CV scans for AgNP-citrate, AgNP-PVP, and AgNP-lipoic acid exhibited an observable valley (see red arrows in **Fig. 5.3.8a**) during the reverse voltage sweep suggesting that the observed Q for these coatings does not entirely result from irreversible charge transfer reaction. This reversible peak may possibly be attributed to the formation of hydrogen bonds between ApoA-I and surface coatings (PVP, citrate, and lipoic acid). Given that bPEI showed completely irreversible stabilizing charge transfer, we expect greater conformational changes in ApoA-I. In other words, the loss of ApoA-I secondary structure on bPEI coated AgNPs precludes reversibility of charge transfer. Such an observation suggests concurs with the CD spectra, which showed complete loss of α–helical content in bPEI coatings. It could be expected that the disruption of stabilizing hydrophobic interactions in the interior of the protein results in an irreversible

charge transfer and ensue in ApoA-I structural relaxation on AgNP-bPEI. On the other hand, AgNP-PVP and AgNP-citrate facilitate hydrogen bond formation with substantial retention of the helical content. Returning to **Fig. 2.3.1**, the loss in α-helical content of ApoA-I on AgNP-lipoic acid cannot be explained based on charge transfer. It is possible that the ApoA-I molecule unfolds on AgNP-lipoic acid surface to increase its interaction with AgNP surface in order to break strong Ag-S interactions in AgNP-lipoic acid.
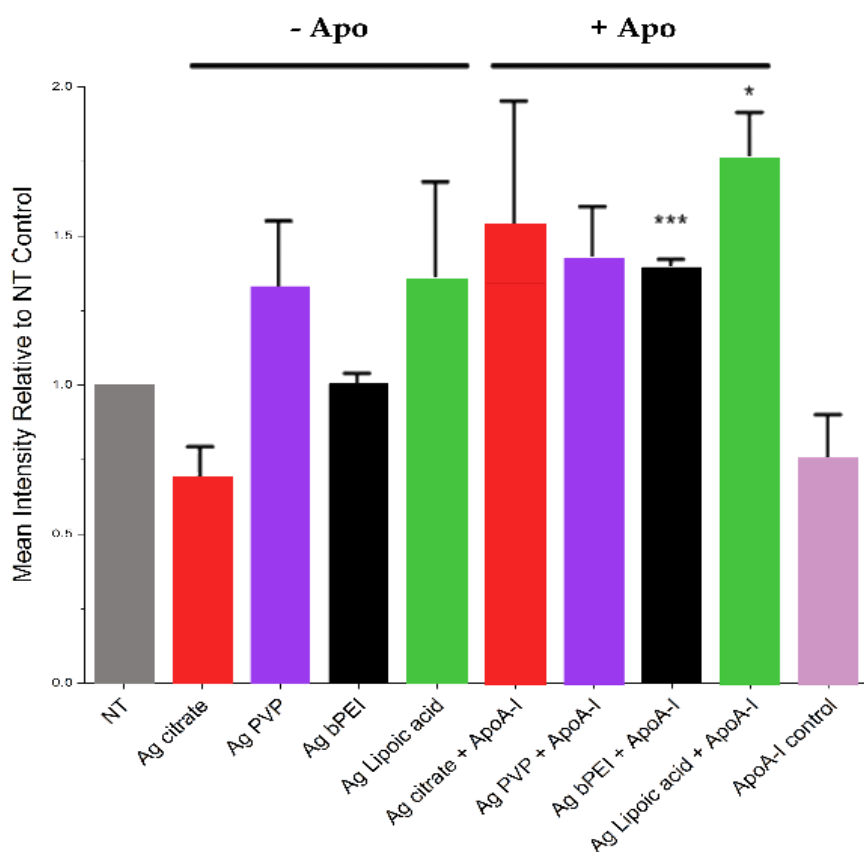
Figure 5.3.9: DCF assay was used to evaluate the ability of AgNPs with (+Apo) and without (-Apo) ApoA-I corona to generate reactive oxygen species (ROS). AgNP-bPEI-ApoA-I displayed a significant increase in ROS generation compared to AgNP-bPEI while the response to AgNP-lipoic acid-ApoA-I was significantly higher than the control.

110

These changes may be attributed the protein unfolding observed in AgNP-bPEI and AgNP-lipoic acid.

We assessed the ability of AgNPs with and without ApoA-I corona to generate intracellular ROS by RAW 264.7 macrophages after 1 h exposure using DCF fluorescence assay. As shown in **Fig. 5.3.9**, we did not observe any significant changes (relative to control) in ROS generation for pristine AgNPs without ApoA-I corona irrespective of their surface coatings. However, we found that the addition of ApoA-I corona changed the response of AgNP-bPEI-ApoA-I relative to AgNP-bPEI without corona and AgNP-lipoic acid-ApoA-I relative to the control. Based on our CD and CV results, we attribute these changes to the adsorption and unfolding of ApoA-I on AgNP-bPEI and AgNP-lipoic acid. Additionally, in case of AgNP-bPEI, ApoA-I corona resulted in an increased surface charge (accompanied by a change from positive to negative sign) and better stability (*cf.* **Fig. 5.3.7b**) that could have also been a contributing factor to the observed increase in ROS generation. Despite these changes in ROS generation, we did not observe any significant differences in the cytotoxicity of AgNPs before and after ApoA-I adsorption. Furthermore, our flow cytometry data did not show significant changes for AgNPs upon the addition of ApoA-I corona. Based on these results, changes in AgNP dissolution or uptake upon the addition of ApoA-I corona could be ruled out as a possible cause for the observed differences in ROS generation.

5.4 Conclusions

In summary, our dynamic and electrophoretic light scattering studies showed that ApoA-I displaces surface coatings such as citrate, PVP, and bPEI even at low concentrations (< 2 g/L). In case of AgNP-lipoic acid, strong Ag-S interactions inhibit ApoA-I adsorption for concentrations below 2 g/L. Circular dichroism studies showed a significant decrease in α-helical content for all surface coatings with the complete disappearance of α–helices for AgNP-bPEI and AgNP-lipoic acid. The changes in secondary structure concur with the observed charge transfer, measured using cyclic voltammetry, between ApoA-I and AgNPs. The unfolding of ApoA-I on AgNP-lipoic acid cannot be completely explained in terms of charge transfer. It is plausible that ApoA-I unfolds on the surface to lower its free energy and thereby break strong Ag-S interactions in AgNP-lipoic acid. Lastly, we found a significant increase in the ability of ApoA-I coated AgNP-bPEI and AgNP-lipoic acid to generate reactive oxygen species, which can be attributed to changes in surface charge and the unfolding of ApoA-I.

We have systematically carried out photoluminescence (PL), cyclic voltammetry (CV), and Raman measurements to elucidate the nature of interactions of aromatic amino acids with two-dimensional materials including graphene, BN, and graphene oxide (GO). PL and CV studies revealed that GO interacts strongly with tyrosine and tryptophan via H-bonding compared to graphene, which exhibited π−π interactions. We also found significant charge transfer between graphene and GO complexes with aromatic amino acids, as verified from CV measurements and Raman spectra. BN, on the other hand, did

not show considerable chemical interactions with aromatic amino acids due to localized π-electron clouds. The adsorption of amino acids was found to alter the potential of twodimensional materials to generate reactive oxygen species (ROS). We did not find significant changes in the ROS levels for graphene, whereas GO and BN showed significant differences, which could be explained on the basis of PL and CV measurements. In summary, the presence of functional groups and $\pi-\pi$ interactions play a significant role in the adsorption of amino acids on 2D materials.

CHAPTER SIX

ENVIRONMENTAL IMPACTS OF TWO-DIMENSIONAL MATERIALS

6.1 Introduction

The recent emergence of two-dimensional engineered nanomaterials (2D-ENM) enabled the advancement of electronics, sensors, coatings, water treatment membranes, and energy storage and conversion devices.[176]–[178] The unique properties of 2D-ENMs provide advantages for many environmental applications such as i) sorbents/photocatalytic materials for environmental remediation including radioactive waste removal [179], [180], ii) next-generation water treatment membranes[181], and iii) sensors for real-time contaminant monitoring.[182] As the production and technological applications of 2D-ENMs continue to grow in the coming years[183], it is imperative to study their environmental interactions for understanding 2D-ENM fate, transport, and toxicity in order to mitigate any potential risks.[184] It is likely that the high surface area of 2D-ENMs amplifies their environmental interactions relative to other nanomaterials.[185] 2D-ENMs discharged into the environment, either from the production facilities or at the end of the product lifecycle, will inevitably bind with natural organic matter (NOM) in water, sediments, and soils. Drawing from our previous studies on the effects of protein binding to ENMs or "protein corona" formation in mammalian cells, we hypothesize that the interactions of 2D-ENMs with NOM modify their surface through the formation of a biocorona and thereby influence their stability and interactions with algae.[164], [186]–[188]

The objective of this study is to investigate the interactions of aquatic NOM (Suwanee River and Nordic reservoir NOMs labeled as SRNOM and NRNOM) with two important 2D-ENMs viz., few-layer graphene and BN. Graphene and BN are structural homologues with differences in π-electron cloud distribution (delocalized in graphene and localized on N in BN), which present good experimental platforms for studying 2D-ENM-NOM interactions.[189] In this study, optical absorption and photoluminescence (PL) spectroscopy in addition to electrochemical measurements were used to elucidate the nature of interactions between NOM and 2D-ENMs. Graphene and BN were found to exhibit a higher affinity for SRNOM, which had more aromatic content than NRNOM. The delocalized π -electron cloud in graphene facilitated chemisorption of both SRNOM and NRNOM, as evidenced by the electrochemical charge transfer between graphene and NOMs. On the other hand, BN exhibited little or no charge transfer with both SRNOM and NRNOM. Importantly, the formation of NOM biocorona significantly impacted the interaction of 2D-ENMs with algal cells. Particularly, the increased surface charge of BN-SRNOM complexes was found to mitigate the adverse effects of BN on algal photosynthesis. These results suggest that it is critical to include the effects of biocorona for assessing the environmental impact of 2D-ENMs.

6.2 Materials and methods

Graphene and BN platelets were synthesized using chemical exfoliation technique described in Ref. [190]. Briefly, graphene/BN platelets were synthesized using the

chemical exfoliation technique. Bulk graphite (~1 g) or BN was suspended in 100 mL of N-methyl-2-pyrrolidinone (NMP) and sonicated using 1/8" tip sonicator (Branson 250) at 100 W for 2 h. After sonication, the suspension was centrifuged at 3000 rpm for 30 mins, and the supernatant was filtered through 0.45 μm nylon filter and resuspended in 100 mL of fresh NMP. This fresh solution was sonicated again for 6 h, and the centrifuged at 1500 rpm for 1 hr. The supernatant was then vacuum filtered using a 0.45 μm nylon filter. The filtered powder was washed several times using deionized water to remove residual NMP and air-dried to obtain exfoliated graphene/BN samples

Suwannee River and Nordic reservoir NOM (SRNOM and NRNOM) were purchased from International Humic Substance Society (IHSS #1R101N and 1R108N) while humic acid was procured from Sigma-Aldrich. Graphene and BN platelets were incubated in SRNOM and NRNOM for 12 hrs at different concentrations to obtain the adsorption isotherms. After incubation, samples were centrifuged at 13,000 rpm and the supernatant was removed. Subsequently, these samples were washed thrice with DI water to remove any loosely bound NOM. Zeta potential was measured using a Malvern Zetasizer. At least ten measurements were performed for each sample to obtain an average zeta potential. Transmission electron microscopy images were obtained using Hitachi H7600 and H9500. The absorbance at 254 nm was monitored using a Perkin Elmer Lambda 950 UV/Vis spectrometer to characterize the amount of adsorbed NOM. Fluorescence spectra were obtained using a Horiba-Jobin Yvon Nanolog coupled to a liquid N2 cooled CCD detector. At least 3 repeats were performed to obtain the average absorbance/fluorescence. A standard curve was created using NOM stock solutions to

obtain the relationship between absorbance at 254 nm and the NOM concentration. Charge transfer was studied using cyclic voltammetry in a three-electrode geometry (working electrode: 2D-ENMs, counter electrode-Pt mesh, Ag/AgCl reference, NOM as the electrolyte) with a Gamry reference 3000 electrochemical system.

Chlamydomonas freshwater algae were purchased from Carolina Biosupply (#152030) and cultured in soli-water medium (#153760) at room temperature under 300 foot-candles illumination for 7 days prior to the experiments. The algal photosynthesis was studied by monitoring CO_2 depletion using a bicarbonate indicator solution (0.2 g of thymol blue, 0.1 g of cresol red, in 0.01 M $NaHCO_3$).[191] For CO_2 depletion studies, the indicator solution was mixed with algae and 2D-ENMs (with and without NOMs; 15, 30, and 80 µg/ml) solution in an airtight tube. The algal photosynthesis depletes CO_2 in the indicator solution (coming from $NaHCO_3$) and thereby alters the pH, which can be monitored by optical absorbance at 574 nm. All the studies were repeated at least with three different sets of algae to obtain statistically meaningful results. The bright-field images of algae with 2D ENMs were obtained using the Axio Imager A1, Zeiss.

6.3 Results and discussion

As shown in **Fig. 6.3.1**, graphene (~10-15 layers) and BN (~20-25 layers) exhibited sheet-like structure, which is a characteristic of 2D-ENMs. Both pristine graphene and BN were found to have a negative surface charge in DI water, as indicated by their zeta potentials -45 and -26 mV, respectively (see Table 1). Upon NOM

117

adsorption, the zeta potential of graphene and BN significantly increased suggesting better stability due to electrostatic repulsion. The effect of NOMs in improving the suspension stability was more pronounced for BN with a markedly higher surface charge on BN-SRNOM and BN-NRNOM.
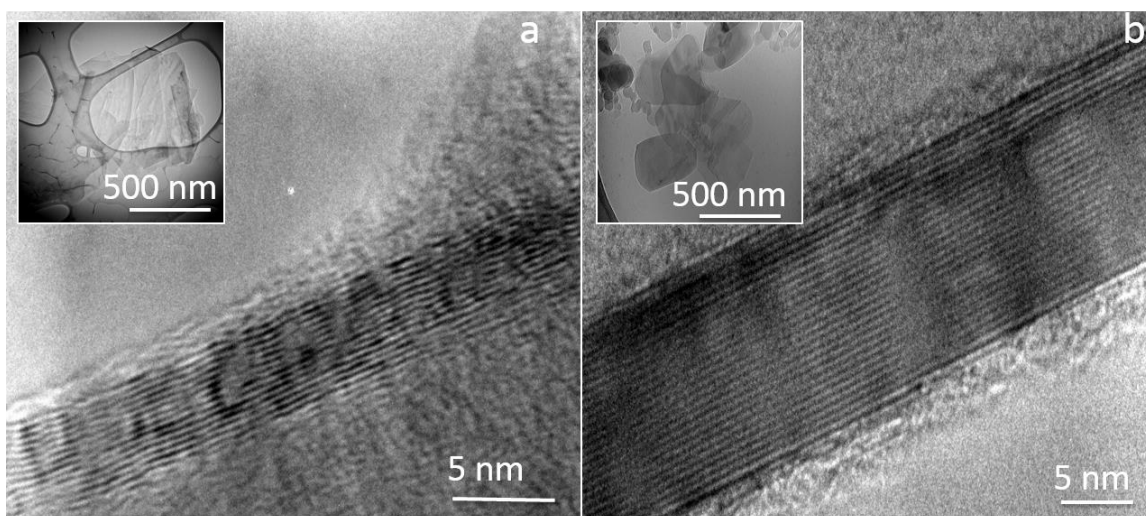
Figure 6.3.1: High-resolution transmission electron microscope images of pristine graphene and BN shows a layered structure with ~10-15 layers for graphene and 20-15 layers for BN. The insets show graphene and BN flakes at lower magnification with lateral sheet dimensions >1 μm.

	Zeta potential (mV)
SRNOM	-18.07
NRNOM	-11.14
Graphene	-44.96
Graphene + SRNOM	-71.42
Graphene + NRNOM	-54.57
BN	-26.38
BN + SRNOM	-69.77
BN + NRNOM	-50.86

Table 6.3.1: Zeta potential values to understand the stability of NOM with 2D materials in the aquatic environment. The result shows graphene and BN stabilize the NOM suspended water.

The adsorption of SRNOM and NRNOM was found to follow a Freundlich isotherm (**Fig. 6.3.2**) given by

$$q_e = K_f C_e^{1/n} \tag{6.1}$$

where q_e is the amount of NOM adsorbed on 2D-ENMs, C_e is the total concentration of NOM in which K_f (and $1/n$) for SRNOM was higher (/lower) than NRNOM (Table 2) suggesting that both graphene and BN showed a greater affinity for SRNOM. This improved affinity was also reflected in the higher zeta potentials for SRNOM-coated graphene and BN (*cf.* Table 1). Such a result may be partly understood in terms of better $\pi-\pi$ interactions[192]–[194] arising from higher aromatic content in SRNOM. NOM is a

heterogeneous mixture of a variety of organic compounds, consisting of aromatic, aliphatic, phenolic, and quinolinic functional groups with varying molecular sizes and properties.[195], [196] The aromatic content in NOM exhibits characteristic fluorescence spectra when excited by UV-light. This fluorescence intensity of NOM was previously used for qualitatively comparing the aromatic content between different types of NOM.[197], [198] Strong fluorescence emission ~450-500 nm was observed for both SRNOM and NRNOM when excited at 330 nm. However, the fluorescence emission from NRNOM was weaker compared to SRNOM, which could be attributed to its lower aromatic content. To further validate the hypothesis that SRNOM exhibits greater affinity due to higher aromatic content, the adsorption isotherms of 2D-ENMs with humic acid or HA, which has a lower aromatic content (and hence lower fluorescence intensity), were measured. As expected, both graphene and BN exhibited significantly lower adsorption of HA with much lower K_f values confirming our hypothesis (**Fig. 6.3.2**).
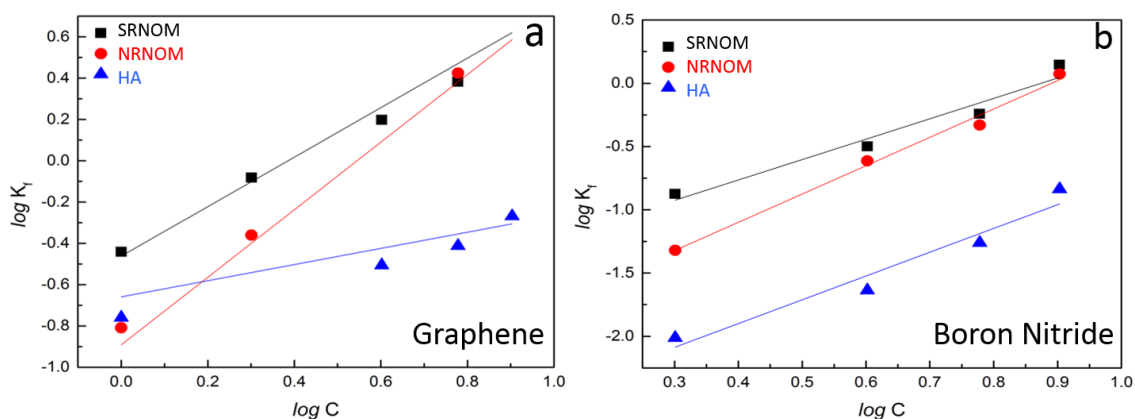
Figure 6.3.2: Adsorption isotherms of NOM on (a) graphene and (b) BN showed that Suwanee River NOM (SRNOM) exhibited higher affinity relative to Nordic reservoir

120

NOM (NRNOM) and humic acid (HA) that have lower aromatic content. The solid lines are fits obtained using Freundlich equation. Fitting parameters are listed in Table 6.3.2.

	K_f	$1/n$
Gr -SRNOM	0.72	0.95
Gr – NRNOM	0.41	1.63
Gr – Humic acid	0.51	0.39
BN – SRNOM	0.22	1.8
BN – NRNOM	0.13	2.24
BN – Humic acid	0.07	1.88

Table 6.3.2: Freundlich adsorption model parameters for graphene, BN with NOMs.

NOM adsorption on many porous materials is strongly influenced by the physical structure of the adsorbent.[199] Although a porous adsorbent (e.g., activated carbon) may have a high affinity for the NOM, its adsorption capacity could be limited by the accessible surface area because larger molecules in NOM are often blocked by micropores and some mesopores[200]–[202]. In such cases, the relationship between K_f and $1/n$ is not linear. In case of graphene and BN, however, it was observed that K_f and $1/n$ are inversely proportional (see **Table 6.3.2**) suggesting that NOM adsorption on 2D-ENMs is only weakly influenced by their physical structure.

While π–π interactions play an important role in the adsorption of NOMs on graphene and BN, an interfacial charge transfer between adsorbed NOM and 2D-ENMs can stabilize the 2D-ENM-NOM complexes by decreasing their total energy through charge redistribution. Thus, in addition to the adsorption isotherms, cyclic voltammetry

(CV) was performed to study the charge transfer interactions between 2D-ENMs and NOM. As described in the experimental section, 2D-ENMs were used as the working electrode while NOM dissolved in DI water was used as the electrolyte for CV measurements. A typical CV scan is performed by cycling the applied voltage on the working electrode (2D-ENMs in our case) between two voltage values while concomitantly measuring the current. The voltage values were chosen to be -0.2 and 0.8 V to avoid the electrolysis of water (see **Fig. 6.3.3**). The applied voltage on the working electrode upshifts (/downshifts) it's electronic energy levels for negative (/positive) voltages. A charge transfer or exchange occurs, between the working electrode and the electrolyte, when some electronic energy levels of the working electrode (for example, lowest energy level in the conduction band or the highest energy level in the valence band) matches either the highest occupied molecular orbital (HOMO) or lowest unoccupied molecular orbital (LUMO) energy states of the electrolyte. In a CV scan, a peak in the current occurs when there is a charge transfer between the working electrode and the analyte (NOM in this case) dissolved in the electrolyte. As shown in **Fig. 6.3.3a and b**, clear irreversible peaks were observed for graphene with both SRNOM and NRNOM indicating the presence of charge transfer reactions. On the other hand, no prominent peaks were found for BN. Such a result is expected the localization of π-electrons on N atoms in BN precludes charge transfer reactions unlike delocalized π-electron cloud in graphene. Similar behavior of graphene and BN was also observed in their interactions with aromatic amino acids. [203]
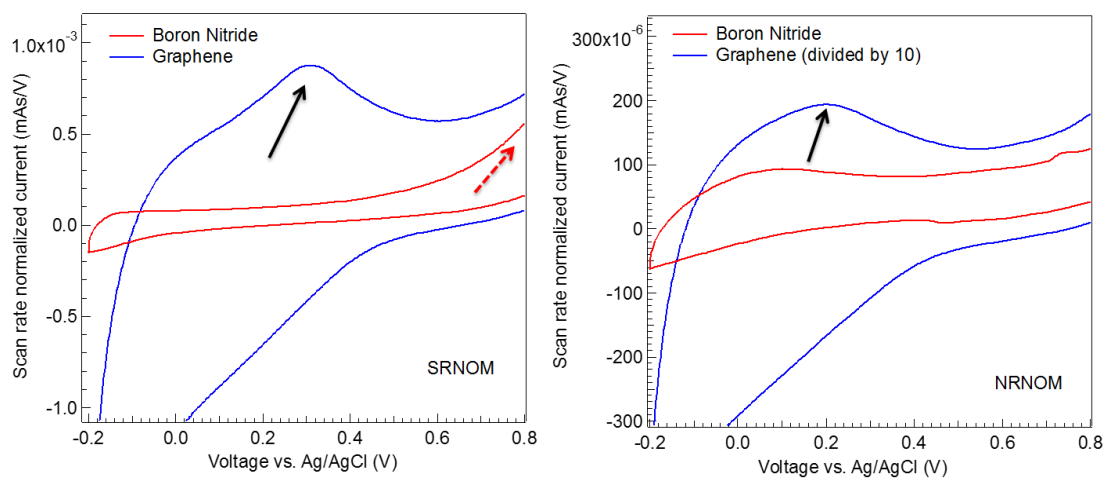
Figure 6.3.3: Cyclic voltammograms of graphene and BN in (a) Suwanee River NOM (SRNOM) and (b) Nordic reservoir NOM (NRNOM): A clear irreversible charge transfer peak (indicated by solid arrows) was observed for graphene while BN did not exhibit any peaks. The dashed arrows indicate the electrolysis of water in the electrolyte at higher voltages. A slow scan rate (~ 5 mV/s) was used in order to exclude any electrolyte diffusion effects.
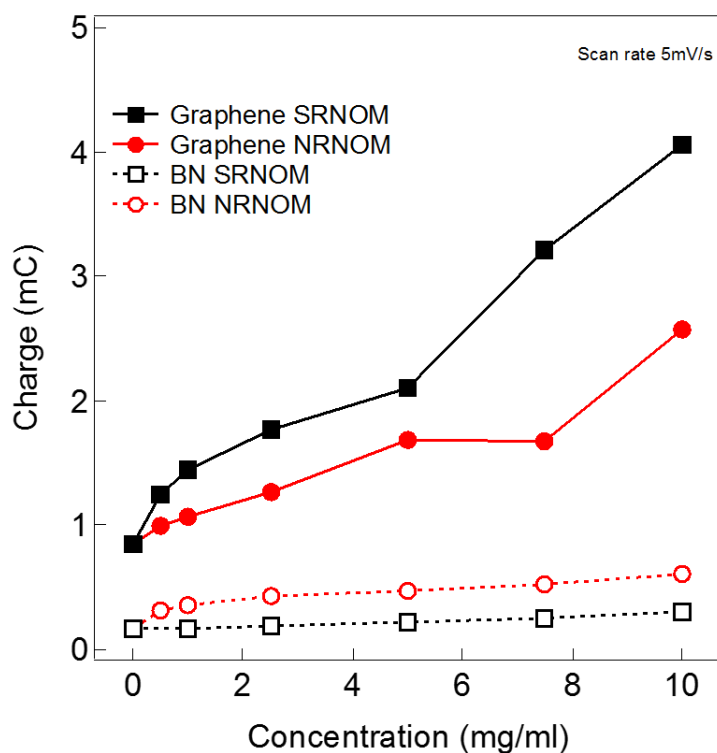
Figure 6.3.4: Charge transfer isotherms for Suwannee Rive & Nordic reservoir NOM (SRNOM and NRNOM) on 2D-ENMs show that NOM adsorption on graphene involves chemisorption, unlike BN. The observed differences between graphene and BN could be attributed to the delocalized π-electron cloud in graphene that facilitates charge transfer with aromatic content in NOM.

For a given NOM concentration, the electrochemical charge transfer can be quantified using the difference in the area enclosed by the CV curve for electrolytes with and without NOM. As shown in **Fig. 6.3.4**, CV curves were measured at different NOM concentrations to obtain charge-transfer isotherms. The charge-transfer isotherms for all

2D-ENMs and NOM combinations showed clear increasing trends as a function of concentration. In case of graphene, SRNOM showed higher charge transfer compared to NRNOM concurring with the results described in **Fig. 6.3.2**. It is plausible that higher aromatic content in SRNOM promotes charge transfer reactions with graphene, in addition to $\pi-\pi$ interactions, to facilitate chemisorption. The isotherms for BN showed no significant increase in charge transfer with increasing NOM concentration possibly due to insulating nature of BN and weaker $\pi-\pi$ interactions resulting from the localization of π-electron cloud on N-atoms.

Considering that living organisms in the environment may be exposed to 2D-ENMs through industrial and research waste, the effects of 2D-ENM-NOM biocorona on algal photosynthesis were evaluated[191], [204]. Algae are an important component of our environment and ecosystem and contribute ~40% of global biomass. In this regard, it is imperative to understand the effects of 2D-ENMs entrained in NOM biocorona on algal toxicity. Single-celled algae, Chlamydomonas sp., were used as the model system to examine the effects of NOM biocorona on CO_2 depletion (**Fig. 6.3.5** and **6.3.6**).
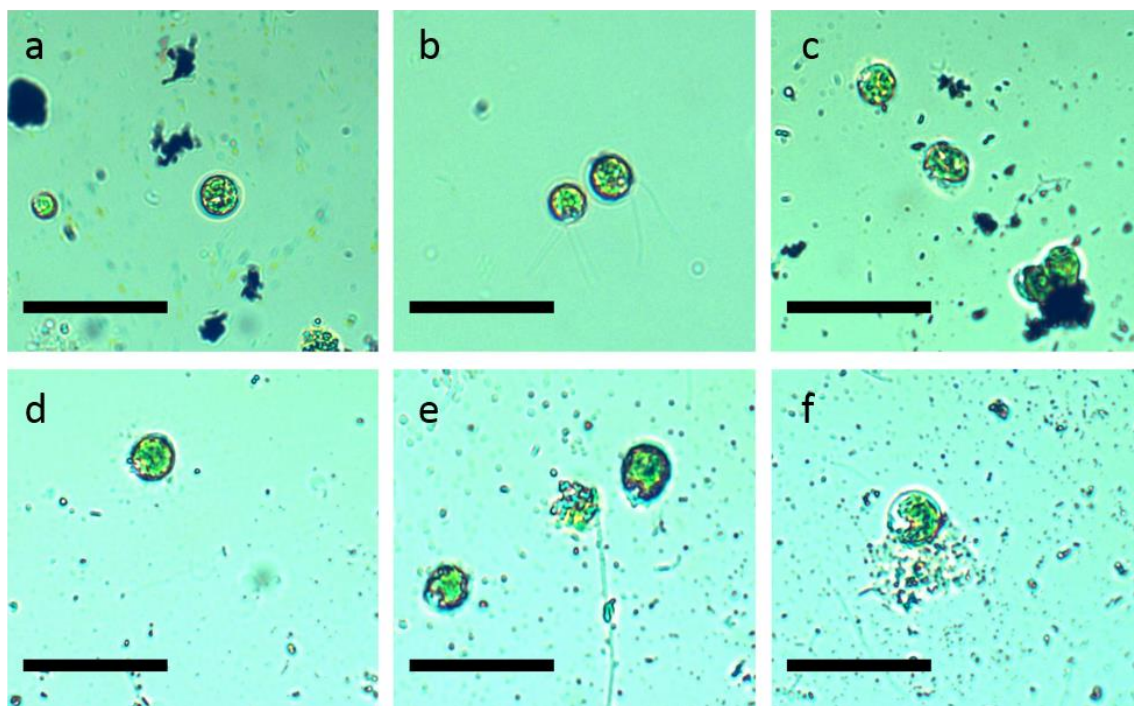
Figure 6.3.5: (a-c) Algae incubated in graphene, graphene with Suwannee and graphene with Nordic. (d-f) Algae incubated in BN, BN with Suwannee and BN with Nordic. The scale bar is 100 µm.
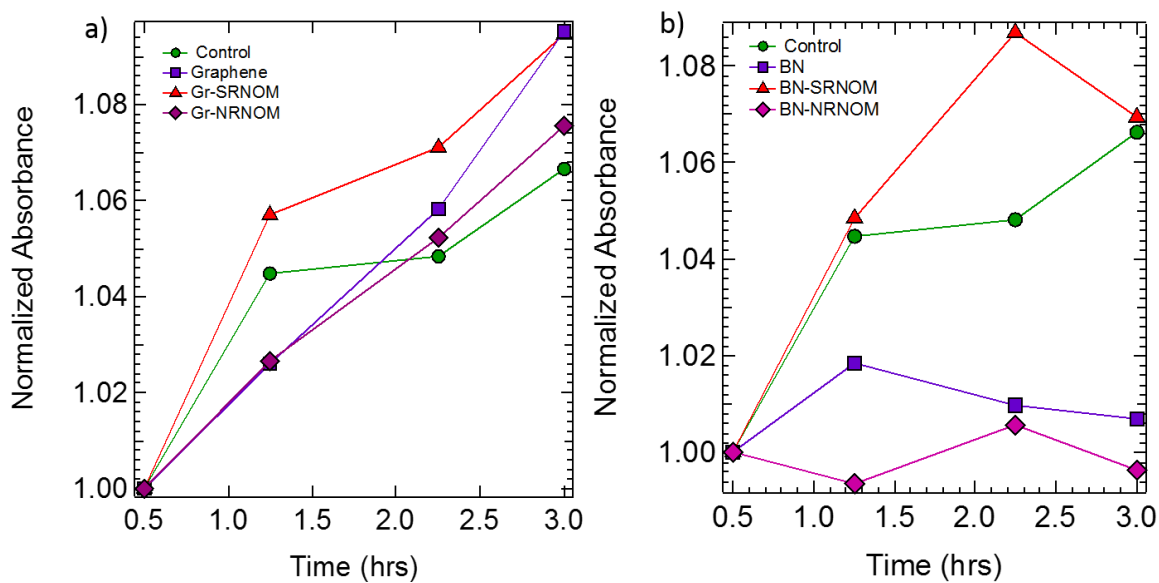
Figure 6.3.6: CO_2 depletion rate measured at 574 nm (as absorbance peak occurs for bicarbonate indicator) for (a) graphene and (b) BN samples at different intervals of time upon incubation with algae.

As shown in **Fig. 6.3.5**, pristine and NOM coated graphene were found to aggregate into ~10-100 μm clusters in the algal medium. Such large aggregates were not observed in case of BN. The algal cells retained their spherical shape when exposed to pristine and NOM coated graphene indicating minimal interactions between graphene and algae. On the other hand, algal cells appeared oblate with ruptured cell walls when exposed to pristine and NOM coated BN. The observed rupturing may be attributed to adsorption and uptake of BN through nitrate/nitrite transporters proteins involved in nitrate assimilation on the surface of Chlamydomonas[205]. Such algal cell rupture is expected to strongly impact their photosynthetic activity. At low concentrations (15 and 30 μg/ml), no significant differences were observed for the rate of CO_2 depletion for both graphene and BN (pristine and NOM coated). The rate of CO_2 depletion at a higher concentration 80 μg/ml is shown in **Fig. 6.3.6**. The rate of CO_2 depletion did not show any significant difference for both pristine and NOM coated graphene concurring with bright-field microscopy images. However, BN and BN-NRNOM were found to significantly decrease the CO_2 depletion rate. This could be rationalized in terms of the light blocking from the photosynthesis centers due to adsorption of the BN and BN-NRNOM on algae. Interestingly, BN-SRNOM showed a CO_2 depletion rate similar to the

control plausibly because of the inhibition of its interaction with nitrate/nitrite transporters proteins due to higher zeta potential relative to BN and BN-NRNOM.

6.4 Conclusions

In summary, the adsorption of NOM was found to increase the surface charge of graphene and BN, which led to better suspension stability. Suwanee River NOM showed higher affinity for graphene and BN due to a higher aromatic content compared to Nordic NOM and humic acid. A clear signature for charge transfer between NOMs and graphene was observed in cyclic voltammetry suggesting that chemisorption of NOMs. The cell walls of algae were found to be ruptured upon exposure to pristine and NOM coated BN, which could be possibly attributed to interactions between BN and algal surface transporter proteins involved in nitrate assimilation. While pristine and NOM coated graphene did not result in algal cell rupture or change CO_2 depletion rate, BN and BN-NRNOM were found to significantly decrease the CO_2 depletion.

CHAPTER SEVEN

SUMMARY AND FUTURE WORK

Vast commercial products integrated with nanomaterials have posed pressing concerns and need for thorough assessment of nanoparticle toxicity. Eventually, these produced goods enter aquatic environment posing threat to aquatic organisms. In this emerging field of nanotoxicity, we have presented a study of biocorona variation with defects, surface functional groups of nanomaterials and also in the altered physiological state. Future direction will further address the ability of carboxylated MWCNTs to deliver the antigen or allergen in animal studies, and further investigate the toxicity using various methods, as well as the possibility of different surface functionalization to alter the immune response *in vivo*. In addition, future studies should examine efficient methods to modify the frequency of defect sites on MWCNTs to improve their capability to bind antigen and optimize MWCNT-based drug/antigen delivery systems.

There still lies action mechanisms that govern nanomaterial toxicity yet to be fully uncovered. Some overlooked factors like protein gradient, temperature and its effects on the composition of biocorona need to be thoroughly assessed. It will be of great interest to understand the implications of nanoparticle-induced cellular toxicity, genotoxicity, bioaccumulation etc. Although studies of environmental impacts of ENMs has grown exponentially, we still lack a complete understanding of its fate, transport, and toxicity in the aquatic environment. Further research studies will enable us to build a predictive model for nanomaterial toxicological effects which guides in the selection and potential safe applications in near future.

APPENDIX

Glossary of acronyms used in the dissertation

1. ENMs: Engineered Nanomaterials

2. BC: Biocorona

3. MD: Molecular Dynamics

4. CD: Circular Dichroism

5. TEM: Transmission Electron Microscopy

6. SEM: Scanning Electron Microscopy

7. 2D: Two-dimensional

8. SWCNTs: Single-Walled Carbon Nanotubes

9. MWCNTs: Multi-Walled Carbon Nanotubes

10. AFM: Atomic Force Microscopy

11. RAEC: Rat Aortic Endothelial Cells

12. ICP-MS: Inductively Coupled Plasma-Mass Spectrometry

13. NOM: Natural Organic Matter

14. Gr: Graphene

15. NPs: Nanoparticles

16. DOS: Density of States

17. FTIR: Fourier Transform Infrared Spectroscopy

18. BSA: Bovine Serum Albumin

19. PVP: Polyvinylpyrrolidone

20. bPEI: branched Polyethylenimine

REFERENCES

[1]   V. H. Nguyen and B. J. Lee, "Protein corona: A new approach for nanomedicine design," *International Journal of Nanomedicine*, vol. 12. pp. 3137–3151, 2017.

[2]   J. Wolfram, Y. Yang, J. Shen, A. Moten, C. Chen, H. Shen, M. Ferrari, and Y. Zhao, "The nano-plasma interface: Implications of the protein corona," *Colloids Surfaces B Biointerfaces*, vol. 124, pp. 17–24, 2014.

[3]   M. E. Vance, T. Kuiken, E. P. Vejerano, S. P. McGinnis, M. F. Hochella, and D. R. Hull, "Nanotechnology in the real world: Redeveloping the nanomaterial consumer products inventory," *Beilstein J. Nanotechnol.*, vol. 6, no. 1, pp. 1769–1780, 2015.

[4]   R. Podila, J. M. Brown, A. Kahru, and A. M. Rao, "Illuminating nano-bio interactions: A spectroscopic perspective," *MRS Bull.*, vol. 39, no. 11, pp. 990–995, 2014.

[5]   A. E. Nel, L. Mädler, D. Velegol, T. Xia, E. M. V Hoek, P. Somasundaran, F. Klaessig, V. Castranova, and M. Thompson, "Understanding biophysicochemical interactions at the nano-bio interface," *Nat. Mater.*, vol. 8, no. 7, pp. 543–557, 2009.

[6]   I. Lynch, A. Salvati, and K. A. Dawson, "Protein-nanoparticle interactions: What does the cell see?," *Nature nanotechnology*, vol. 4, no. 9. pp. 546–547, 2009.

[7]   A. Salvati, C. Åberg, K. A. Dawson, M. P. Monopoli, C. Åberg, A. Salvati, K. A. Dawson, C. Aberg, A. Salvati, and K. A. Dawson, "Biomolecular coronas provide

the biological identity of nanosized materials," *Nat. Nanotechnol.*, vol. 7, no. 12, pp. 779–786, 2012.

[8]   L. Vroman, A. L. Adams, G. C. Fischer, and P. C. Munoz, "Interaction of high molecular weight kininogen, factor XII, and fibrinogen in plasma at interfaces.," *Blood*, vol. 55, no. 1, pp. 156–9, 1980.

[9]   M. P. Monopoli, D. Walczyk, A. Campbell, G. Elia, I. Lynch, F. Baldelli Bombelli, and K. A. Dawson, "Physical-Chemical aspects of protein corona: Relevance to in vitro and in vivo biological impacts of nanoparticles," *J. Am. Chem. Soc.*, vol. 133, no. 8, pp. 2525–2534, 2011.

[10]   M. Lundqvist, J. Stigler, G. Elia, I. Lynch, T. Cedervall, and K. A. Dawson, "Nanoparticle size and surface properties determine the protein corona with possible implications for biological impacts.," *Proc. Natl. Acad. Sci. U. S. A.*, vol. 105, no. 38, pp. 14265–70, 2008.

[11]   I. Nasir, M. Lundqvist, and C. Cabaleiro-Lago, "Size and surface chemistry of nanoparticles lead to a variant behavior in the unfolding dynamics of human carbonic anhydrase," *Nanoscale*, vol. 7, no. 41, pp. 17504–17515, 2015.

[12]   M. Mahmoudi, I. Lynch, M. R. Ejtehadi, M. P. Monopoli, F. B. Bombelli, and S. Laurent, "Protein-nanoparticle interactions: Opportunities and challenges," *Chemical Reviews*, vol. 111, no. 9. pp. 5610–5637, 2011.

[13]   M. A. Dobrovolskaia, A. K. Patri, J. Zheng, J. D. Clogston, N. Ayub, P. Aggarwal, B. W. Neun, J. B. Hall, and S. E. McNeil, "Interaction of colloidal gold nanoparticles with human blood: effects on particle size and analysis of plasma

protein binding profiles," *Nanomedicine Nanotechnology, Biol. Med.*, vol. 5, no. 2, pp. 106–117, 2009.

[14]   S. Lindman, I. Lynch, E. Thulin, H. Nilsson, K. A. Dawson, and S. Linse, "Systematic investigation of the thermodynamics of HSA adsorption to N-iso-propylacrylamide/N-tert-butylacrylamide copolymer nanoparticles. Effects of particle size and hydrophobicity," *Nano Lett.*, vol. 7, no. 4, pp. 914–920, 2007.

[15]   E. Casals, T. Pfaller, A. Duschl, G. J. Oostingh, and V. Puntes, "Time evolution of the nanoparticle protein corona," *ACS Nano*, vol. 4, no. 7, pp. 3623–3632, 2010.

[16]   P. Aggarwal, J. B. Hall, C. B. McLeland, M. A. Dobrovolskaia, and S. E. McNeil, "Nanoparticle interaction with plasma proteins as it relates to particle biodistribution, biocompatibility and therapeutic efficacy," *Advanced Drug Delivery Reviews*, vol. 61, no. 6. pp. 428–437, 2009.

[17]   G. Maiorano, S. Sabella, B. Sorce, V. Brunetti, M. A. Malvindi, R. Cingolani, and P. P. Pompa, "Effects of Cell Culture Media on the Protein-Nanoparticle Complexes and Influence on the Cellular Response," *ACS Nano*, vol. 4, no. 12, pp. 7481–7491, 2010.

[18]   M. R. Wiesner, G. V. Lowry, P. Alvarez, D. Dionysiou, and P. Biswas, "Assessing the risks of manufactured nanomaterials," *Environmental Science and Technology*, vol. 40, no. 14. pp. 4336–4345, 2006.

[19]   I. Dror, B. Yaron, and B. Berkowitz, "Abiotic soil changes induced by engineered nanomaterials: A critical review," *Journal of contaminant hydrology*, vol. 181. pp. 3–16, 2015.

[20] M. Farré, K. Gajda-Schrantz, L. Kantiani, and D. Barceló, "Ecotoxicity and analysis of nanomaterials in the aquatic environment," *Anal. Bioanal. Chem.*, vol. 393, no. 1, pp. 81–95, 2009.

[21] P. Borm and V. Castranova, "Toxicology of Nanomaterials: Permanent interactive learning.," *Part. Fibre Toxicol.*, vol. 6, p. 28, 2009.

[22] A. M. Fan and G. Alexeeff, "Nanotechnology and nanomaterials: toxicology, risk assessment, and regulations.," *J. Nanosci. Nanotechnol.*, vol. 10, no. 12, pp. 8646–8657, 2010.

[23] M. R. Wiesner, G. V. Lowry, P. Alvarez, D. Dionysiou, and P. Biswas, "Assessing the risks of manufactured nanomaterials," *Environmental Science and Technology*, vol. 40, no. 14. pp. 4336–4345, 2006.

[24] R. Duncan and R. Gaspar, "Nanomedicine(s) under the microscope," *Molecular Pharmaceutics*, vol. 8, no. 6. pp. 2101–2141, 2011.

[25] C. Corbo, R. Molinaro, A. Parodi, N. E. Toledano Furman, F. Salvatore, and E. Tasciotti, "The impact of nanoparticle protein corona on cytotoxicity, immunotoxicity and target drug delivery," *Nanomedicine*, vol. 11, no. 1, pp. 81–100, 2016.

[26] A. Salvati, C. Åberg, K. A. Dawson, M. P. Monopoli, C. Åberg, A. Salvati, K. A. Dawson, C. Aberg, A. Salvati, and K. A. Dawson, "Biomolecular coronas provide the biological identity of nanosized materials," *Nat. Nanotechnol.*, vol. 7, no. 12, pp. 779–786, 2012.

[27] S. Tenzer, D. Docter, J. Kuharev, A. Musyanovych, V. Fetz, R. Hecht, F. Schlenk,

D. Fischer, K. Kiouptsi, C. Reinhardt, K. Landfester, H. Schild, M. Maskos, S. K. Knauer, and R. H. Stauber, "Rapid formation of plasma protein corona critically affects nanoparticle pathophysiology.," *Nat. Nanotechnol.*, vol. 8, no. 10, pp. 772–81, 2013.

[28]   J. H. Shannahan, K. S. Fritz, A. J. Raghavendra, R. Podila, I. Persaud, and J. M. Brown, "From the Cover: Disease-Induced Disparities in Formation of the Nanoparticle-Biocorona and the Toxicological Consequences," *Toxicol. Sci.*, vol. 152, no. 2, pp. 406–416, 2016.

[29]   J. Huang, L. Bu, J. Xie, K. Chen, Z. Cheng, X. Li, and X. Chen, "Effects of nanoparticle size on cellular uptake and liver MRI with polyvinylpyrrolidone-coated iron oxide nanoparticles," *ACS Nano*, vol. 4, no. 12, pp. 7151–7160, 2010.

[30]   B. Yameen, W. Il Choi, C. Vilos, A. Swami, J. Shi, and O. C. Farokhzad, "Insight into nanoparticle cellular uptake and intracellular targeting," *J. Control. Release*, vol. 190, pp. 485–499, 2014.

[31]   W. Jiang, B. Y. S. Kim, J. T. Rutka, and W. C. W. Chan, "Nanoparticle-mediated cellular response is size-dependent.," *Nat. Nanotechnol.*, vol. 3, no. 3, pp. 145–50, 2008.

[32]   V. Mirshafiee, M. Mahmoudi, K. Lou, J. Cheng, and M. L. Kraft, "Protein corona significantly reduces active targeting yield.," *Chem. Commun. (Camb).*, vol. 49, no. 25, pp. 2557–2559, 2013.

[33]   R. R. Arvizo, K. Giri, D. Moyano, O. R. Miranda, B. Madden, D. J. McCormick, R. Bhattacharya, V. M. Rotello, J. P. Kocher, and P. Mukherjee, "Identifying new

therapeutic targets via modulation of protein corona formation by engineered nanoparticles," *PLoS One*, vol. 7, no. 3, 2012.

[34] R. Podila and J. M. Brown, "Toxicity of Engineered Nanomaterials: A Physicochemical Perspective," *J. Biochem. Mol. Toxicol.*, vol. 27, no. 1, pp. 50–55, 2013.

[35] L. Shang, K. Nienhaus, and G. U. Nienhaus, "Engineered nanoparticles interacting with cells: size matters.," *J. Nanobiotechnology*, vol. 12, no. 1, p. 5, 2014.

[36] R. Podila, R. Chen, P. C. Ke, J. M. Brown, and a. M. Rao, "Effects of surface functional groups on the formation of nanoparticle-protein corona," *Appl. Phys. Lett.*, vol. 101, no. 26, 2012.

[37] J. H. Shannahan, R. Podila, and J. M. Brown, "A hyperspectral and toxicological analysis of protein corona impact on silver nanoparticle properties, intracellular modifications, and macrophage activation," *Int. J. Nanomedicine*, vol. 10, pp. 6509–6520, Oct. 2015.

[38] M. A. Calin, S. V. Parasca, D. Savastru, and D. Manea, "Hyperspectral Imaging in the Medical Field: Present and Future," *Appl. Spectrosc. Rev.*, vol. 49, no. 6, pp. 435–447, 2014.

[39] M. Mortimer, A. Gogos, N. Bartolomé, A. Kahru, T. D. Bucheli, and V. I. Slaveykova, "Potential of hyperspectral imaging microscopy for semi-quantitative analysis of nanoparticle uptake by Protozoa," *Environ. Sci. Technol.*, vol. 48, no. 15, pp. 8760–8767, 2014.

[40] N. Fairbairn, R. Fernandes, R. Carter, T. J. Elliot, A. G. Kanaras, and O. L.

Muskens, "Single-nanoparticle detection and spectroscopy in cells using a hyperspectral darkfield imaging technique," *Spie ...*, vol. 1, no. 1, p. 859501, 2013.

[41]   J. H. Shannahan, R. Podila, and J. M. Brown, "A hyperspectral and toxicological analysis of protein corona impact on silver nanoparticle properties, intracellular modifications, and macrophage activation," *Int. J. Nanomedicine*, vol. 10, pp. 6509–6520, Oct. 2015.

[42]   Y. Chen, J. A. Preece, and R. E. Palmer, "Processing and characterization of gold nanoparticles for use in plasmon probe spectroscopy and microscopy of biosystems," in *Annals of the New York Academy of Sciences*, 2008, vol. 1130, pp. 201–206.

[43]   M. A. Vetten, N. Tlotleng, D. Tanner Rascher, A. Skepu, F. K. Keter, K. Boodhia, L.-A. Koekemoer, C. Andraos, R. Tshikhudo, and M. Gulumian, "Label-free in vitro toxicity and uptake assessment of citrate stabilised gold nanoparticles in three cell lines.," *Part. Fibre Toxicol.*, vol. 10, no. 1, p. 50, 2013.

[44]   S. Patskovsky, E. Bergeron, and M. Meunier, "Hyperspectral darkfield microscopy of PEGylated gold nanoparticles targeting CD44-expressing cancer cells," *J. Biophotonics*, vol. 8, no. 1–2, pp. 162–167, 2015.

[45]   C. Grabinski, J. Schlager, and S. Hussain, "Hyperspectral microscopy for characterization of gold nanoparticles in biological media and cells for toxicity assessment.," *Methods Mol. Biol.*, vol. 1025, pp. 167–178, 2013.

[46]   D. Zhang, O. Neumann, H. Wang, V. M. Yuwono, A. Barhoumi, M. Perham, J. D. Hartgerink, P. Wittung-Stafshede, and N. J. Halas, "Gold nanoparticles can induce

the formation of protein-based aggregates at physiological pH," *Nano Lett.*, vol. 9, no. 2, pp. 666–671, 2009.

[47] Z. J. Deng, M. Liang, M. Monteiro, I. Toth, and R. F. Minchin, "Nanoparticle-induced unfolding of fibrinogen promotes Mac-1 receptor activation and inflammation," *Nat. Nanotechnol.*, vol. 6, no. 1, pp. 39–44, 2011.

[48] N. J. Greenfield, "Using circular dichroism spectra to estimate protein secondary structure," *Nat. Protoc.*, vol. 1, no. 6, pp. 2876–2890, 2006.

[49] L. Whitmore and B. A. Wallace, "Protein secondary structure analyses from circular dichroism spectroscopy: Methods and reference databases," *Biopolymers*, vol. 89, no. 5, pp. 392–400, 2008.

[50] S. M. Kelly, T. J. Jess, and N. C. Price, "How to study proteins by circular dichroism," *Biochimica et Biophysica Acta - Proteins and Proteomics*, vol. 1751, no. 2. pp. 119–139, 2005.

[51] P. Through and C. Dichroism, "Proteins Through Circular Dichroism," *Ann. Rev. Biophys. Biophys. Cher*, vol. 17, no. Cd, pp. 145–66, 1988.

[52] Y. L. Marcel and R. S. Kiss, "Structure-function relationships of apolipoprotein A-I: a flexible protein with dynamic lipid associations.," *Curr. Opin. Lipidol.*, vol. 14, no. 2, pp. 151–7, 2003.

[53] R. Huang, R. A. G. D. Silva, W. G. Jerome, A. Kontush, M. J. Chapman, L. K. Curtiss, T. J. Hodges, and W. S. Davidson, "Apolipoprotein A-I structural organization in high-density lipoproteins isolated from human plasma.," *Nat. Struct. Mol. Biol.*, vol. 18, no. 4, pp. 416–22, 2011.

[54] D. W. Borhani, D. P. Rogers, J. a Engler, and C. G. Brouillette, "Crystal structure of truncated human apolipoprotein A-I suggests a lipid-bound conformation.," *Proc. Natl. Acad. Sci. U. S. A.*, vol. 94, no. 23, pp. 12291–12296, 1997.

[55] K. Saha, D. F. Moyano, and V. M. Rotello, "Protein coronas suppress the hemolytic activity of hydrophilic and hydrophobic nanoparticles.," *Mater. horizons*, vol. 2014, no. 1, pp. 102–105, 2014.

[56] I. Lynch and K. A. Dawson, "Protein-nanoparticle interactions," *Nano Today*, vol. 3, no. 1–2. pp. 40–47, 2008.

[57] A. J. Raghavendra, N. Alsaleh, J. M. Brown, and R. Podila, "Charge-transfer interactions induce surface dependent conformational changes in apolipoprotein biocorona," *Biointerphases*, vol. 12, no. 2, p. 02D402, 2017.

[58] B. Sengupta, W. E. Gregory, J. Zhu, S. Dasetty, M. Karakaya, J. M. Brown, A. M. Rao, J. K. Barrows, S. Sarupria, and R. Podila, "Influence of carbon nanomaterial defects on the formation of protein corona," *Rsc Adv.*, vol. 5, no. 100, pp. 82395–82402, 2015.

[59] S. C. Roy, M. Paulose, and C. A. Grimes, "The effect of TiO2 nanotubes in the enhancement of blood clotting for the control of hemorrhage," *Biomaterials*, vol. 28, no. 31, pp. 4667–4672, 2007.

[60] J. H. Morrissey, E. Tajkhorshid, and C. M. Rienstra, "Nanoscale studies of protein-membrane interactions in blood clotting," *Journal of Thrombosis and Haemostasis*, vol. 9, no. 1 S. pp. 162–167, 2011.

[61] L. Wang, A. K. Pal, J. A. Isaacs, D. Bello, and R. L. Carrier, "Nanomaterial

induction of oxidative stress in lung epithelial cells and macrophages," *J. Nanoparticle Res.*, vol. 16, no. 9, 2014.

[62]   B. Wang, P. Wu, R. A. Yokel, and E. A. Grulke, "Influence of surface charge on lysozyme adsorption to ceria nanoparticles," *Appl. Surf. Sci.*, vol. 258, no. 14, pp. 5332–5341, 2012.

[63]   K. Bradley, J.-C. P. Gabriel, M. Briman, A. Star, and G. Grüner, "Charge transfer from ammonia physisorbed on nanotubes.," *Phys. Rev. Lett.*, vol. 91, no. 21, p. 218301, 2003.

[64]   C. P. Firme and P. R. Bandaru, "Toxicity issues in the application of carbon nanotubes to biological systems," *Nanomedicine: Nanotechnology, Biology, and Medicine*, vol. 6, no. 2. pp. 245–256, Apr-2010.

[65]   R. Podila, P. Vedantam, P. C. Ke, J. M. Brown, and a M. Rao, "Evidence for charge-transfer-induced conformational changes in CNT-Protien corona.pdf," 2012.

[66]   E. B. Barros, A. G. S. Filho, V. Lemos, J. M. Filho, S. B. Fagan, M. H. Herbst, J. M. Rosolen, C. A. Luengo, and J. G. Huber, "Charge transfer effects in acid treated single-wall carbon nanotubes," *Carbon N. Y.*, vol. 43, no. 12, pp. 2495–2500, 2005.

[67]   L. H. Butterfield, "Cancer vaccines.," *BMJ*, vol. 350, no. 5, p. h988, 2015.

[68]   E. J. Ryan, L. M. Daly, and K. H. G. Mills, "Immunomodulators and delivery systems for vaccination by mucosal routes," *Trends in Biotechnology*, vol. 19, no. 8. pp. 293–304, 2001.

[69] E. B. Lindblad, "Aluminium compounds for use in vaccines," *Immunology and Cell Biology*, vol. 82, no. 5. pp. 497–505, 2004.

[70] D. M. Smith, J. K. Simon, and J. R. Baker, "Applications of nanotechnology for immunology," *Nature Reviews Immunology*, vol. 13, no. 8. pp. 592–605, 2013.

[71] C. H. Villa, T. Dao, I. Ahearn, N. Fehrenbacher, E. Casey, D. A. Rey, T. Korontsvit, V. Zakhaleva, C. A. Batt, M. R. Philips, and D. A. Scheinberg, "Single-walled carbon nanotubes deliver peptide antigen into dendritic cells and enhance IgG responses to tumor-associated antigens," *ACS Nano*, vol. 5, no. 7, pp. 5300–5311, 2011.

[72] P. C. B. De Faria, L. I. Dos Santos, J. P. Coelho, H. B. Ribeiro, M. A. Pimenta, L. O. Ladeira, D. A. Gomes, C. A. Furtado, and R. T. Gazzinelli, "Oxidized multiwalled carbon nanotubes as antigen delivery system to promote superior CD8+ T Cell response and protection against Cancer," *Nano Lett.*, vol. 14, no. 9, pp. 5458–5470, 2014.

[73] B. S. Wong, S. L. Yoong, A. Jagusiak, T. Panczyk, H. K. Ho, W. H. Ang, and G. Pastorin, "Carbon nanotubes for delivery of small molecule drugs," *Advanced Drug Delivery Reviews*, vol. 65, no. 15. pp. 1964–2015, 2013.

[74] T. L. Moore, J. E. Pitzer, R. Podila, X. Wang, R. L. Lewis, S. W. Grimes, J. R. Wilson, E. Skjervold, J. M. Brown, A. Rao, and F. Alexis, "Multifunctional polymer-coated carbon nanotubes for safe drug delivery," *Part. Part. Syst. Charact.*, vol. 30, no. 4, pp. 365–373, 2013.

[75] L. Yan, F. Zhao, S. Li, Z. Hu, and Y. Zhao, "Low-toxic and safe nanomaterials by

surface-chemical design, carbon nanotubes, fullerenes, metallofullerenes, and graphenes," *Nanoscale*, vol. 3, no. 2, pp. 362–382, 2011.

[76]   J. H. Shannahan, J. M. Brown, R. Chen, P. C. Ke, X. Lai, S. Mitra, and F. A. Witzmann, "Comparison of nanotube-protein corona composition in cell culture media.," *Small*, vol. 9, no. 12, pp. 2171–81, 2013.

[77]   D. A. Gomez-Gualdrón, J. C. Burgos, J. Yu, and P. B. Balbuena, "Carbon nanotubes: Engineering biomedical applications," *Progress in Molecular Biology and Translational Science*, vol. 104. pp. 175–245, 2011.

[78]   F. Liang and B. Chen, "A Review on Biomedical Applications of Single-Walled Carbon Nanotubes," *Curr. Med. Chem.*, vol. 17, no. 1, pp. 10–24, 2010.

[79]   B. Anand, R. Podila, P. Ayala, L. Oliveira, R. Philip, S. S. S. Sai, A. a Zakhidov, and A. M. Rao, "Nonlinear optical properties of boron doped single-walled carbon nanotubes.," *Nanoscale*, vol. 5, no. 16, pp. 7271–6, 2013.

[80]   Y. Stubrov, A. Nikolenko, V. Gubanov, and V. Strelchuk, "Manifestation of Structure of Electron Bands in Double-Resonant Raman Spectra of Single-Walled Carbon Nanotubes," *Nanoscale Res. Lett.*, vol. 11, no. 1, pp. 1–5, 2016.

[81]   L.-C. Ong, F. F.-L. Chung, Y.-F. Tan, and C.-O. Leong, "Toxicity of single-walled carbon nanotubes," *Arch. Toxicol.*, vol. 90, no. 1, pp. 103–118, 2016.

[82]   M. Lundqvist, J. Stigler, T. Cedervall, T. Berggård, M. B. Flanagan, I. Lynch, G. Elia, and K. Dawson, "The Evolution of the Protein Corona around Nanoparticles: A Test Study," *ACS Nano*, vol. 5, no. 9, pp. 7503–7509, 2011.

[83]   M. P. Monopoli, A. S. Pitek, I. Lynch, and K. A. Dawson, "Formation and

characterization of the nanoparticle-protein corona," *Methods Mol. Biol.*, vol. 1025, pp. 137–155, 2013.

[84] D. J. O'Connell, F. B. Bombelli, A. S. Pitek, M. P. Monopoli, D. J. Cahill, and K. A. Dawson, "Characterization of the bionano interface and mapping extrinsic interactions of the corona of nanomaterials," *Nanoscale*, vol. 7, no. 37, pp. 15268–15276, 2015.

[85] Z. Wang, C. Wang, S. Liu, W. He, L. Wang, J. Gan, Z. Huang, Z. Wang, H. Wei, J. Zhang, and L. Dong, "Specifically Formed Corona on Silica Nanoparticles Enhances Transforming Growth Factor β1 Activity in Triggering Lung Fibrosis," *ACS Nano*, vol. 11, no. 2, pp. 1659–1672, 2017.

[86] X. Cheng, X. Tian, A. Wu, J. Li, J. Tian, Y. Chong, Z. Chai, Y. Zhao, C. Chen, and C. Ge, "Protein Corona Influences Cellular Uptake of Gold Nanoparticles by Phagocytic and Nonphagocytic Cells in a Size-Dependent Manner," *ACS Appl. Mater. Interfaces*, vol. 7, no. 37, pp. 20568–20575, 2015.

[87] P. L. Chariou, K. L. Lee, A. M. Wen, N. M. Gulati, P. L. Stewart, and N. F. Steinmetz, "Detection and imaging of aggressive cancer cells using an epidermal growth factor receptor (EGFR)-Targeted filamentous plant virus-based nanoparticle," *Bioconjug. Chem.*, vol. 26, no. 2, pp. 262–269, 2015.

[88] W. S. Cho, F. Thielbeer, R. Duffin, E. M. V. Johansson, I. L. Megson, W. Macnee, M. Bradley, and K. Donaldson, "Surface functionalization affects the zeta potential, coronal stability and membranolytic activity of polymeric nanoparticles," *Nanotoxicology*, vol. 8, no. 2, pp. 202–211, 2014.

[89] R. Liu, W. Jiang, C. D. Walkey, W. C. W. Chan, and Y. Cohen, "Prediction of nanoparticles-cell association based on corona proteins and physicochemical properties," *Nanoscale*, vol. 7, no. 21, pp. 9664–9675, 2015.

[90] Y. Fan, B. R. Goldsmith, and P. G. Collins, "Identifying and counting point defects in carbon nanotubes," *Nat. Mater.*, vol. 4, no. 12, pp. 906–911, 2005.

[91] B. Sengupta, W. E. Gregory, J. Zhu, S. Dasetty, M. Karakaya, J. M. Brown, A. M. Rao, J. K. Barrows, S. Sarupria, and R. Podila, "Influence of carbon nanomaterials defects on the formation of protein corona," *J. Phys. Chem. Chem. Phys. Phys. Chem. Chem. Phys*, vol. 0, pp. 1–3, 2015.

[92] Y. Chen and S. Mitra, "Fast microwave-assisted purification, functionalization and dispersion of multi-walled carbon nanotubes.," *J. Nanosci. Nanotechnol.*, vol. 8, no. 11, pp. 5770–5775, 2008.

[93] S. Gordon and F. O. Martinez, "Alternative activation of macrophages: Mechanism and functions," *Immunity*, vol. 32, no. 5. pp. 593–604, 2010.

[94] W. Bai, A. Raghavendra, R. Podila, and J. M. Brown, "Defect density in multiwalled carbon nanotubes influences ovalbumin adsorption and promotes macrophage activation and CD4+T-cell proliferation," *Int. J. Nanomedicine*, vol. 11, pp. 4357–4371, 2016.

[95] Y. Murakami, "Growth of vertically aligned single-walled carbon nanotube films on quartz substrates and their optical anisotropy," *Chem. Phys. Lett.*, vol. 385, no. 3–4, pp. 298–303, 2004.

[96] N. Pierard, A. Fonseca, J. F. Colomer, C. Bossuot, J. M. Benoit, G. Van Tendeloo,

J. P. Pirard, and J. B. Nagy, "Ball milling effect on the structure of single-wall carbon nanotubes," *Carbon N. Y.*, vol. 42, no. 8–9, pp. 1691–1697, 2004.

[97] S. M. Wojtowicz-Praga, R. B. Dickson, and M. J. Hawkins, "Matrix metalloproteinase inhibitors," *Investigational New Drugs*, vol. 15, no. 1. pp. 61–75, 1997.

[98] D. Bhowmick and G. Mugesh, "Insights into the catalytic mechanism of synthetic glutathione peroxidase mimetics," *Org. Biomol. Chem.*, vol. 13, no. 41, pp. 10262–10272, 2015.

[99] J. Shannahan, R. Podila, and J. M. Brown, "A hyperspectral and toxicological analysis of protein corona impact on silver nanoparticle properties , intracellular modifications , and macrophage activation," *Int. J. Nanomedicine*, vol. 2015:10, pp. 6509–6521, 2015.

[100] D. Ricklin and J. D. Lambris, "Complement in immune and inflammatory disorders: pathophysiological mechanisms.," *J. Immunol.*, vol. 190, no. 8, pp. 3831–8, 2013.

[101] J. Köhrle, "Environment and endocrinology: The case of thyroidology," *Ann. Endocrinol. (Paris).*, vol. 69, no. 2, pp. 116–122, 2008.

[102] S. G. Han, B. Newsome, and B. Hennig, "Titanium dioxide nanoparticles increase inflammatory responses in vascular endothelial cells," *Toxicology*, vol. 306, pp. 1–8, 2013.

[103] N. L. Mills, M. R. Miller, A. J. Lucking, J. Beveridge, L. Flint, A. J. F. Boere, P. H. Fokkens, N. A. Boon, T. Sandstrom, A. Blomberg, R. Duffin, K. Donaldson, P.

W. F. Hadoke, F. R. Cassee, and D. E. Newby, "Combustion-derived nanoparticulate induces the adverse vascular effects of diesel exhaust inhalation," *Eur. Heart J.*, vol. 32, no. 21, pp. 2660–2671, 2011.

[104] H. Rosas-Hernández, S. Jiménez-Badillo, P. P. Martínez-Cuevas, E. Gracia-Espino, H. Terrones, M. Terrones, S. M. Hussain, S. F. Ali, and C. González, "Effects of 45-nm silver nanoparticles on coronary endothelial cells and isolated rat aortic rings," *Toxicol. Lett.*, vol. 191, no. 2–3, pp. 305–313, 2009.

[105] L. K. Vesterdal, L. Mikkelsen, J. K. Folkmann, M. Sheykhzade, Y. Cao, M. Roursgaard, S. Loft, and P. Møller, "Carbon black nanoparticles and vascular dysfunction in cultured endothelial cells and artery segments," *Toxicol. Lett.*, vol. 214, no. 1, pp. 19–26, 2012.

[106] C. J. Wingard, D. M. Walters, B. L. Cathey, S. C. Hilderbrand, P. Katwa, S. Lin, P. C. Ke, R. Podila, A. Rao, R. M. Lust, and J. M. Brown, "Mast cells contribute to altered vascular reactivity and ischemia-reperfusion injury following cerium oxide nanoparticle instillation," *Nanotoxicology*, vol. 5, no. 4, pp. 531–545, 2011.

[107] A. C. P. Elder, R. Gelein, M. Azadniv, M. Frampton, J. Finkelstein, and G. Oberdörster, "Systemic effects of inhaled ultrafine particles in two compromised, aged rat strains.," *Inhal. Toxicol.*, vol. 16, no. 6–7, pp. 461–71, 2004.

[108] J. Schwartz and D. W. Dockery, "Increased mortality in Philadelphia associated with daily air pollution concentrations.," *Am. Rev. Respir. Dis.*, vol. 145, pp. 600–604, 1992.

[109] J. Schwartz and R. Morris, "Air pollution and hospital admissions for

cardiovascular disease in Detroit, Michigan.," *Am. J. Epidemiol.*, vol. 142, no. 1, pp. 23–35, 1995.

[110] M. Catalano, A. Aronica, G. Carzaniga, R. Seregni, and A. Libretti, "Serum lipids and apolipoproteins in patients with essential hypertension," *Atherosclerosis*, vol. 87, no. 1, pp. 17–22, 1991.

[111] W. A. LaFramboise, R. Dhir, L. A. Kelly, P. Petrosko, J. M. Krill-Burger, C. M. Sciulli, M. A. Lyons-Weiler, U. R. Chandran, A. Lomakin, R. V. Masterson, O. C. Marroquin, S. R. Mulukutla, and D. M. McNamara, "Serum protein profiles predict coronary artery disease in symptomatic patients referred for coronary angiography," *BMC Med.*, vol. 10, 2012.

[112] M. P. Monopoli, C. Åberg, A. Salvati, and K. A. Dawson, "Biomolecular coronas provide the biological identity of nanosized materials," *Nat. Nanotechnol.*, vol. 7, no. 12, pp. 779–786, 2012.

[113] A. Beduneau, Z. Ma, C. B. Grotepas, A. Kabanov, B. E. Rabinow, N. Gong, R. L. Mosley, H. Dou, M. D. Boska, and H. E. Gendelman, "Facilitated monocyte-macrophage uptake and tissue distribution of superparmagnetic iron-oxide nanoparticles," *PLoS One*, vol. 4, no. 2, 2009.

[114] M. J. D. Clift, S. Bhattacharjee, D. M. Brown, and V. Stone, "The effects of serum on the toxicity of manufactured nanoparticles," *Toxicol. Lett.*, vol. 198, no. 3, pp. 358–365, 2010.

[115] L. Lartigue, C. Wilhelm, J. Servais, C. Factor, A. Dencausse, J. C. Bacri, N. Luciani, and F. Gazeau, "Nanomagnetic sensing of blood plasma protein

interactions with iron oxide nanoparticles: Impact on macrophage uptake," *ACS Nano*, vol. 6, no. 3, pp. 2665–2678, 2012.

[116] F. Joris, B. B. Manshian, K. Peynshaert, S. C. De Smedt, K. Braeckmans, and S. J. Soenen, "Assessing nanoparticle toxicity in cell-based assays: influence of cell culture parameters and optimized models for bridging the in vitro–in vivo gap," *Chem. Soc. Rev.*, vol. 42, no. 21, p. 8339, 2013.

[117] A. Jedlovszky-Hajdú, F. B. Bombelli, M. P. Monopoli, E. Tombácz, and K. A. Dawson, "Surface coatings shape the protein corona of SPIONs with relevance to their application in vivo," *Langmuir*, vol. 28, no. 42, pp. 14983–14991, 2012.

[118] J. H. Shannahan, X. Lai, P. C. Ke, R. Podila, J. M. Brown, and F. A. Witzmann, "Silver nanoparticle protein corona composition in cell culture media.," *PLoS One*, vol. 8, no. 9, p. e74001, 2013.

[119] C. D. Walkey, J. B. Olsen, H. Guo, A. Emili, and W. C. W. Chan, "Nanoparticle size and surface chemistry determine serum protein adsorption and macrophage uptake," *J. Am. Chem. Soc.*, vol. 134, no. 4, pp. 2139–2147, 2012.

[120] C. D. Walkey, J. B. Olsen, F. Song, R. Liu, H. Guo, D. W. H. Olsen, Y. Cohen, A. Emili, and W. C. W. Chan, "Protein corona fingerprinting predicts the cellular interaction of gold and silver nanoparticles," *ACS Nano*, vol. 8, no. 3, pp. 2439–2455, Mar. 2014.

[121] L. Babes, B. Denizot, G. Tanguy, J. J. Le Jeune, and P. Jallet, "Synthesis of Iron Oxide Nanoparticles Used as MRI Contrast Agents: A Parametric Study," *J. Colloid Interface Sci.*, vol. 212, no. 2, pp. 474–482, 1999.

[122] A. K. Gupta and M. Gupta, "Synthesis and surface engineering of iron oxide nanoparticles for biomedical applications," *Biomaterials*, vol. 26, no. 18. pp. 3995–4021, 2005.

[123] H. Amiri, L. Bordonali, A. Lascialfari, S. Wan, M. P. Monopoli, I. Lynch, S. Laurent, and M. Mahmoudi, "Protein corona affects the relaxivity and MRI contrast efficiency of magnetic nanoparticles," *Nanoscale*, vol. 5, no. 18, p. 8656, 2013.

[124] J. H. Shannahan, X. Lai, P. C. Ke, R. Podila, J. M. Brown, and F. A. Witzmann, "Silver Nanoparticle Protein Corona Composition in Cell Culture Media," *PLoS One*, vol. 8, no. 9, 2013.

[125] J. H. Shannahan, H. Sowrirajan, I. Persaud, R. Podila, and J. M. Brown, "Impact of Silver and Iron Nanoparticle Exposure on Cholesterol Uptake by Macrophages," *J. Nanomater.*, vol. 2015, p. 127235, 2015.

[126] Y. Fukuda, K. Ando, R. Ishikura, N. Kotoura, N. Tsuda, N. Kato, S. Yoshiya, and N. Nakao, "Superparamagnetic iron oxide (SPIO) MRI contrast agent for bone marrow imaging: differentiating bone metastasis and osteomyelitis.," *Magn. Reson. Med. Sci.*, vol. 5, no. 4, pp. 191–6, 2006.

[127] Y.-X. J. Wang, "Superparamagnetic iron oxide based MRI contrast agents: Current status of clinical application," *Quant Imaging Med Surg*, vol. 1, no. Dcc, pp. 35–44, 2011.

[128] D. Mazzei, M. A. Guzzardi, S. Giusti, and A. Ahluwalia, "A low shear stress modular bioreactor for connected cell culture under high flow rates," *Biotechnol.*

Bioeng., vol. 106, no. 1, pp. 127–137, 2010.

[129] C. Grabinski, M. Sharma, E. Maurer, C. Sulentic, R. Mohan Sankaran, and S. Hussain, "The effect of shear flow on nanoparticle agglomeration and deposition in in vitro dynamic flow models," *Nanotoxicology*, vol. 10, no. 1, pp. 74–83, 2016.

[130] A. G. Koutsiaris, S. V Tachmitzi, N. Batis, M. G. Kotoula, C. H. Karabatsas, E. Tsironi, and D. Z. Chatzoulis, "Volume flow and wall shear stress quantification in the human conjunctival capillaries and post-capillary venules in vivo.," *Biorheology*, vol. 44, no. 5–6, pp. 375–86, 2007.

[131] J. Seebach, P. Dieterich, F. Luo, H. Schillers, D. Vestweber, H. Oberleithner, H. J. Galla, and H. J. Schnittler, "Endothelial barrier function under laminar fluid shear stress.," *Lab. Invest.*, vol. 80, no. 12, pp. 1819–31, 2000.

[132] S. Tenzer, D. Docter, S. Rosfa, A. Wlodarski, J. Kuharev, A. Rekik, S. K. Knauer, C. Bantz, T. Nawroth, C. Bier, J. Sirirattanapan, W. Mann, L. Treuel, R. Zellner, M. Maskos, H. Schild, and R. H. Stauber, "Nanoparticle size is a critical physicochemical determinant of the human blood plasma corona: A comprehensive quantitative proteomic analysis," *ACS Nano*, vol. 5, no. 9, pp. 7155–7167, 2011.

[133] J. Shannahan, "The biocorona: A challenge for the biomedical application of nanoparticles," *Nanotechnol. Rev.*, vol. 6, no. 4, pp. 345–353, 2017.

[134] H. Shen, L. Zhang, M. Liu, and Z. Zhang, "Biomedical applications of graphene," *Theranostics*, vol. 2, no. 3. pp. 283–294, 2012.

[135] Y. Wang, Z. Li, J. Wang, J. Li, and Y. Lin, "Graphene and graphene oxide:

Biofunctionalization and applications in biotechnology," *Trends in Biotechnology*, vol. 29, no. 5. pp. 205–212, 2011.

[136] S. Goenka, V. Sant, and S. Sant, "Graphene-based nanomaterials for drug delivery and tissue engineering," *Journal of Controlled Release*, vol. 173, no. 1. pp. 75–88, 2014.

[137] J. Liu, L. Cui, and D. Losic, "Graphene and graphene oxide as new nanocarriers for drug delivery applications," *Acta Biomaterialia*, vol. 9, no. 12. pp. 9243–9257, 2013.

[138] T. L. Moore, R. Podilakrishna, A. Rao, and F. Alexis, "Systemic Administration of Polymer-Coated Nano-Graphene to Deliver Drugs to Glioblastoma," *Part. Part. Syst. Charact.*, vol. 31, no. 8, pp. 886–894, 2014.

[139] R. Podila, T. Moore, F. Alexis, and A. M. Rao, "Graphene coatings for enhanced hemo-compatibility of nitinol stents," *RSC Adv.*, vol. 3, no. 6, p. 1660, 2013.

[140] P. Miró, M. Audiffred, and T. Heine, "An atlas of two-dimensional materials.," *Chem. Soc. Rev.*, 2014.

[141] T. Hashimoto, T. Perlot, A. Rehman, J. Trichereau, H. Ishiguro, M. Paolino, V. Sigl, T. Hanada, R. Hanada, S. Lipinski, B. Wild, S. M. R. Camargo, D. Singer, A. Richter, K. Kuba, A. Fukamizu, S. Schreiber, H. Clevers, F. Verrey, P. Rosenstiel, and J. M. Penninger, "ACE2 links amino acid malnutrition to microbial ecology and intestinal inflammation," *Nature*, vol. 487, no. 7408. pp. 477–481, 2012.

[142] X.-R. Xia, N. a Monteiro-Riviere, and J. E. Riviere, "Supplementary Information: An index for characterization of nanomaterials in biological systems.," *Nat.*

Nanotechnol., vol. 5, no. 9, pp. 671–675, 2010.

[143] H. Vovusha, S. Sanyal, and B. Sanyal, "Interaction of nucleobases and aromatic amino acids with graphene oxide and graphene flakes," *J. Phys. Chem. Lett.*, vol. 4, no. 21, pp. 3710–3718, 2013.

[144] R. Podila, P. Vedantam, P. C. Ke, J. M. Brown, and A. M. Rao, "Evidences For Charge Transfer-Induced Conformational Changes In Carbon Nanostructure-Protein Corona.," *J. Phys. Chem. C. Nanomater. Interfaces*, vol. 116, no. 41, pp. 22098–22103, 2012.

[145] H. Y. Zhang, Z. X. Ji, T. Xia, H. Meng, C. Low-Kam, R. Liu, S. Pokhrel, S. J. Lin, X. Wang, Y. P. Liao, M. Y. Wang, L. J. Li, R. Rallo, R. Damoiseaux, D. Telesca, L. Madler, Y. Cohen, J. I. Zink, and A. E. Nel, "Use of Metal Oxide Nanoparticle Band Gap To Develop a Predictive Paradigm for Oxidative Stress and Acute Pulmonary Inflammation," *ACS Nano*, vol. 6, no. 5, pp. 4349–4368, 2012.

[146] C. J. Murphy, A. M. Vartanian, F. M. Geiger, R. J. Hamers, J. Pedersen, Q. Cui, C. L. Haynes, E. E. Carlson, R. Hernandez, R. D. Klaper, G. Orr, and Z. Rosenzweig, "Biological Responses to Engineered Nanomaterials: Needs for the Next Decade," *ACS Cent. Sci.*, vol. 1, no. 3, pp. 117–123, 2015.

[147] T. Cedervall, I. Lynch, S. Lindman, T. Berggard, E. Thulin, H. Nilsson, K. a Dawson, and S. Linse, "Understanding the nanoparticle-protein corona using methods to quantify exchange rates and affinities of proteins for nanoparticles," *Proc. Natl. Acad. Sci.*, vol. 104, no. 7, pp. 2050–2055, 2007.

[148] A. Marucco, I. Fenoglio, F. Turci, and B. Fubini, "Interaction of fibrinogen and

albumin with titanium dioxide nanoparticles of different crystalline phases," *J. Phys. Conf. Ser.*, vol. 429, p. 12014, 2013.

[149] D. Dutta, S. K. Sundaram, J. G. Teeguarden, B. J. Riley, L. S. Fifield, J. M. Jacobs, S. R. Addleman, G. A. Kaysen, B. M. Moudgil, and T. J. Weber, "Adsorbed proteins influence the biological activity and molecular targeting of nanomaterials," *Toxicol. Sci.*, vol. 100, no. 1, pp. 303–315, 2007.

[150] J. H. Shannahan, J. M. Brown, R. Chen, P. C. Ke, X. Lai, S. Mitra, and F. A. Witzmann, "Comparison of nanotube-protein corona composition in cell culture media," *Small*, vol. 9, no. 12, pp. 2171–2181, 2013.

[151] R. Podila, R. Chen, P. C. Ke, J. M. Brown, and A. M. Rao, "Effects of surface functional groups on the formation of nanoparticle-protein corona," *Appl. Phys. Lett.*, vol. 101, no. 26, 2012.

[152] T. Cedervall, I. Lynch, S. Lindman, T. Berggård, E. Thulin, H. Nilsson, K. A. Dawson, and S. Linse, "Understanding the nanoparticle-protein corona using methods to quantify exchange rates and affinities of proteins for nanoparticles.," *Proc. Natl. Acad. Sci. U. S. A.*, vol. 104, no. 7, pp. 2050–2055, 2007.

[153] A. Verma and F. Stellacci, "Effect of surface properties on nanoparticle-cell interactions," *Small*, vol. 6, no. 1. pp. 12–21, 2010.

[154] R. a Sperling and W. J. Parak, "Surface modification, functionalization and bioconjugation of colloidal inorganic nanoparticles.," *Philos. Trans. A. Math. Phys. Eng. Sci.*, vol. 368, no. 1915, pp. 1333–1383, 2010.

[155] P. Satzer, F. Svec, G. Sekot, and A. Jungbauer, "Protein adsorption onto

nanoparticles induces conformational changes: Particle size dependency, kinetics, and mechanisms," *Eng. Life Sci.*, vol. 16, no. 3, pp. 238–246, 2016.

[156] W. Norde, "My voyage of discovery to proteins in flatland ...and beyond," *Colloids Surfaces B Biointerfaces*, vol. 61, no. 1, pp. 1–9, 2008.

[157] C. C. Gibson, D. a. Puleo, and R. Bizios, *Biological interactions on materials surfaces: understanding and controlling protein, cell, and tissue responses.* Springer New York, 2009.

[158] Y. Fang, O. Gursky, and D. Atkinson, "Structural studies of N- and C-terminally truncated human apolipoprotein A-I," *Biochemistry*, vol. 42, no. 22, pp. 6881–6890, 2003.

[159] D. W. Borhani, J. A. Engler, and C. G. Brouillette, "Crystallization of truncated human apolipoprotein A-I in a novel conformation," *Acta Crystallogr. Sect. D Biol. Crystallogr.*, vol. 55, no. 9, pp. 1578–1583, 1999.

[160] A. A. Ajees, G. M. Anantharamaiah, V. K. Mishra, M. M. Hussain, and H. M. K. Murthy, "Crystal structure of human apolipoprotein A-I: Insights into its protective effect against cardiovascular diseases," *Proc. Natl. Acad. Sci. U. S. A.*, vol. 103, no. 7, pp. 2126–2131, 2006.

[161] X. Mei and D. Atkinson, "Crystal structure of C-terminal truncated apolipoprotein A-I reveals the assembly of High Density Lipoprotein (HDL) by dimerization," *J. Biol. Chem.*, vol. 286, no. 44, pp. 38570–38582, 2011.

[162] W. S. Davidson and T. B. Thompson, "The structure of apolipoprotein A-I in high density lipoproteins.," *J. Biol. Chem.*, vol. 282, no. 31, pp. 22249–22253, 2007.

[163] R. Cukalevski, M. Lundqvist, C. Oslakovic, B. Dahlbäck, S. Linse, and T. Cedervall, "Structural changes in apolipoproteins bound to nanoparticles," *Langmuir*, vol. 27, no. 23, pp. 14360–14369, 2011.

[164] S. Radic, N. K. Geitner, R. Podila, A. Käkinen, P. Chen, P. C. Ke, and F. Ding, "Competitive binding of natural amphiphiles with graphene derivatives.," *Sci. Rep.*, vol. 3, p. 2273, 2013.

[165] C. Rajesh, C. Majumder, H. Mizuseki, and Y. Kawazoe, "A theoretical study on the interaction of aromatic amino acids with graphene and single walled carbon nanotube.," *J. Chem. Phys.*, vol. 130, no. 12, p. 124911, 2009.

[166] C. Cazorla, "Ab initio study of the binding of collagen amino acids to graphene and A-doped (A=H, Ca) graphene," *Thin Solid Films*, vol. 518, no. 23. pp. 6951–6961, 2010.

[167] R. a. Latour, "The langmuir isotherm: A commonly applied but misleading approach for the analysis of protein adsorption behavior," *J. Biomed. Mater. Res. Part A*, vol. 103, no. 3, pp. 949–958, 2015.

[168] R. Podila, R. Rao, R. Tsuchikawa, M. Ishigami, and A. M. Rao, "Raman spectroscopy of folded and scrolled graphene," *ACS Nano*, vol. 6, no. 7, pp. 5784–5790, 2012.

[169] K. Krishnamoorthy, M. Veerapandian, K. Yun, and S.-J. Kim, "The chemical and structural analysis of graphene oxide with different degrees of oxidation," *Carbon N. Y.*, vol. 53, pp. 38–49, 2013.

[170] R. Li, R. Chen, P. Chen, Y. Wen, P. C. Ke, and S. S. Cho, "Computational and

experimental characterizations of silver nanoparticle-apolipoprotein biocorona," *J. Phys. Chem. B*, vol. 117, no. 43, pp. 13451–13456, 2013.

[171] A. Longo, M. Palomba, S. De Nicola, and G. Carotenuto, "Dependence of Optical and Microstructure Properties of Thiol-Capped Silver Nanoparticles Embedded in Polymeric Matrix," *Polymers*, vol. 3. pp. 1794–1804, 2011.

[172] D. R. Jackson, S. Omanovic, and S. G. Roscoe, "Electrochemical studies of the adsorption behavior of serum proteins on titanium," *Langmuir*, vol. 16, no. 12, pp. 5449–5457, Jun. 2000.

[173] N. A. Ramella, O. J. Rimoldi, E. D. Prieto, G. R. Schinella, S. A. Sanchez, M. S. Jaureguiberry, M. E. Vela, S. T. Ferreira, and M. A. Tricerri, "Human apolipoprotein A-I-derived amyloid: Its association with atherosclerosis," *PLoS One*, vol. 6, no. 7, 2011.

[174] H. J. Schönfeld, D. Roessner, and J. Seelig, "Self-Association of Apo A-1 Studied with Dynamic and Static Light Scattering," *J. Phys. Chem. B*, vol. 120, no. 7, pp. 1228–1235, Feb. 2016.

[175] A. A-i, W. H. O. International, R. Materials, and A. A-i, "Serum Concentrations a Population Sample of Apolipoprotein B , and Lipoprotein (a) in," vol. 636, 1995.

[176] S. Borini, R. White, D. Wei, M. Astley, S. Haque, E. Spigone, N. Harris, J. Kivioja, and T. Ryhänen, "Ultrafast graphene oxide humidity sensors," *ACS Nano*, vol. 7, no. 12, pp. 11166–11173, 2013.

[177] F. Bonaccorso, L. Colombo, G. Yu, M. Stoller, V. Tozzini, A. C. Ferrari, R. S. Ruoff, and V. Pellegrini, "Graphene, related two-dimensional crystals, and hybrid

systems for energy conversion and storage," *Science (80-.).*, vol. 347, no. 6217, pp. 1246501–1246501, 2015.

[178] A. S. Aricò, P. Bruce, B. Scrosati, J.-M. Tarascon, and W. van Schalkwijk, "Nanostructured materials for advanced energy conversion and storage devices," *Nat. Mater.*, vol. 4, no. 5, pp. 366–377, 2005.

[179] M. M. Khin, a. S. Nair, V. J. Babu, R. Murugan, and S. Ramakrishna, "A review on nanomaterials for environmental remediation," *Energy Environ. Sci.*, vol. 5, no. 8, p. 8075, 2012.

[180] K. S. Subrahmanyam, D. Sarma, C. D. Malliakas, K. Polychronopoulou, B. J. Riley, D. A. Pierce, J. Chun, and M. G. Kanatzidis, "Chalcogenide aerogels as sorbents for radioactive iodine," *Chem. Mater.*, vol. 27, no. 7, pp. 2619–2626, 2015.

[181] J. Kou, J. Yao, Li. Wu, X. Zhou, H. Lu, F. Wu, and J. Fan, "Nanoporous Two-Dimensional MoS2 Membrane for Fast Saline Solution Purification," *Phys. Chem. Chem. Phys.*, vol. 18, pp. 22210–22216, 2016.

[182] Y. Ying, Y. Yang, W. Ying, and X. Peng, "Two-dimensional materials for novel liquid separation membranes," *Nanotechnology*, vol. 27, no. 33, p. 332001, 2016.

[183] M. S. Mauter and M. Elimelech, "Environmental applications of carbon-based nanomaterials," *Environmental Science and Technology*, vol. 42, no. 16. pp. 5843–5859, 2008.

[184] D. Lin, X. Tian, F. Wu, and B. Xing, "Fate and transport of engineered nanomaterials in the environment.," *J. Environ. Qual.*, vol. 39, no. 6, pp. 1896–

1908, 2010.

[185] S. Radic, N. K. Geitner, R. Podila, A. Käkinen, P. Chen, P. C. Ke, and F. Ding, "Competitive Binding of Natural Amphiphiles with Graphene Derivatives," *Sci. Rep.*, vol. 3, p. 2273, 2013.

[186] J. Zhao, J. P. Lu, J. Han, and C. K. Yang, "Noncovalent functionalization of carbon nanotubes by aromatic organic molecules," *Appl. Phys. Lett.*, vol. 82, no. 21, pp. 3746–3748, 2003.

[187] H. Hyung and J. H. Kim, "Natural organic matter (NOM) adsorption to multi-walled carbon nanotubes: Effect of NOM characteristics and water quality parameters," *Environ. Sci. Technol.*, vol. 42, no. 12, pp. 4416–4421, 2008.

[188] F. Tournus, S. Latil, M. Heggie, and J.-C. Charlier, "π-stacking interaction between carbon nanotubes and organic molecules," *Physical Review B*, vol. 72, no. 7. 2005.

[189] A. Nag, K. Raidongia, K. P. S. S. Hembram, R. Datta, U. V. Waghmare, and C. N. R. Rao, "Graphene analogues of BN: Novel synthesis and properties," *ACS Nano*, vol. 4, no. 3, pp. 1539–1544, 2010.

[190] S. S. K. Mallineni, J. Shannahan, A. J. Raghavendra, A. M. Rao, J. M. Brown, and R. Podila, "Biomolecular Interactions and Biological Responses of Emerging Two-Dimensional Materials and Aromatic Amino Acid Complexes," *ACS Appl. Mater. Interfaces*, vol. 8, no. 26, pp. 16604–16611, 2016.

[191] S. Lin, P. Bhattacharya, N. C. Rajapakse, D. E. Brune, and P. C. Ke, "Effects of quantum dots adsorption on algal photosynthesis," *J. Phys. Chem. C*, vol. 113, no.

25, pp. 10962–10966, 2009.

[192] C. A. Hunter and J. K. M. Sanders, "The Nature of pi-pi Interactions," *J. Am. Chem. Soc.*, vol. 112, pp. 5525–5534, 1990.

[193] C. R. Martinez and B. L. Iverson, "Rethinking the term 'pi-stacking,'" *Chemical Science*, vol. 3, no. 7. p. 2191, 2012.

[194] M. Swart, T. van der Wijst, C. Fonseca Guerra, and F. M. Bickelhaupt, "Pi-pi stacking tackled with density functional theory.," *J. Mol. Model.*, vol. 13, no. 12, pp. 1245–1257, 2007.

[195] M. Sillanpää, A. Matilainen, and T. Lahtinen, "Characterization of NOM," in *Natural Organic Matter in Water: Characterization and Treatment Methods*, 2014, pp. 17–53.

[196] D. M. Owen, G. L. Amy, Z. K. Chowdhury, R. Paode, G. McCoy, and K. Viscosil, "NOM characterization and treatability," *J. / Am. Water Work. Assoc.*, vol. 87, no. 1, pp. 46–63, 1995.

[197] L. Martin-Neto, D. M. B. P. Milori, W. T. L. Da Silva, and M. L. Simões, "EPR, FTIR, Raman, UV-Visible Absorption, and Fluorescence Spectroscopies in Studies of NOM," in *Biophysico-Chemical Processes Involving Natural Nonliving Organic Matter in Environmental Systems*, 2009, pp. 651–727.

[198] J. Chen, E. J. LeBoeuf, S. Dai, and B. Gu, "Fluorescence spectroscopic studies of natural organic matter fractions," *Chemosphere*, vol. 50, no. 5, pp. 639–647, 2003.

[199] H. Van De Weerd, W. H. Van Riemsdijk, and A. Leijnse, "Modeling the dynamic adsorption/desorption of a NOM mixture: Effects of physical and chemical

heterogeneity," *Environ. Sci. Technol.*, vol. 33, no. 10, pp. 1675–1681, 1999.

[200] G. Newcombe and M. Drikas, "Adsorption of NOM onto activated carbon: Electrostatic and non-electrostatic effects," *Carbon N. Y.*, vol. 35, no. 9, pp. 1239–1250, 1997.

[201] C. Pelekani and V. L. Snoeyink, "Competitive adsorption in natural water: Role of activated carbon pore size," *Water Res.*, vol. 33, no. 5, pp. 1209–1219, 1999.

[202] M. Bjelopavlic, G. Newcombe, and R. Hayes, "Adsorption of NOM onto Activated Carbon: Effect of Surface Charge, Ionic Strength, and Pore Volume Distribution.," *J. Colloid Interface Sci.*, vol. 210, no. 2, pp. 271–280, 1999.

[203] S. S. K. Mallineni, J. Shannahan, A. J. Raghavendra, A. M. Rao, J. M. Brown, and R. Podila, "Biomolecular Interactions and Biological Responses of Emerging Two-Dimensional Materials and Aromatic Amino Acid Complexes," *ACS Appl. Mater. Interfaces*, vol. 8, no. 26, pp. 16604–16611, 2016.

[204] C. W. Cho, T. P. T. Pham, Y. C. Jeon, J. Min, H. Y. Jung, D. S. Lee, and Y. S. Yun, "Microalgal photosynthetic activity measurement system for rapid toxicity assessment," *Ecotoxicology*, vol. 17, no. 6, pp. 455–463, 2008.

[205] E. Sanz-Luque, A. Chamizo-Ampudia, A. Llamas, A. Galvan, and E. Fernandez, "Understanding nitrate assimilation and its regulation in microalgae," *Front. Plant Sci.*, vol. 6, 2015.